Summer 1996

Numerical Prediction of Turbulent Diffusion Flames Formed by Cylindrical Tube Injector

Ali S. Kheireddine
Old Dominion University

Recommended Citation

Kheireddine, Ali S.. "Numerical Prediction of Turbulent Diffusion Flames Formed by Cylindrical Tube Injector" (1996). Doctor of Philosophy (PhD), Dissertation, Mechanical & Aerospace Engineering, Old Dominion University, DOI: 10.25777/yt26-9798
https://digitalcommons.odu.edu/mae_etds/128

NUMERICAL PREDICTION OF TURBULENT DIFFUSION FLAMES FORMED BY CYLINDRICAL TUBE INJECTOR

by

Ali S. Kheireddine
B. S., May 1990, Mechanical Engineering Technology
M. S., December 1992, Department of Mechanical Engineering and Mechanics
Old Dominion University, Norfolk Virginia

A Dissertation submitted to the Faculty
of Old Dominion University in Partial Fulfillment of the
Requirements for the Degree of

DOCTOR OF PHILOSOPHY
MECHANICAL ENGINEERING
OLD DOMINION UNIVERSITY
August, 1996

Approved by:

Dr. S. K. Chaturvedi (Director)

Dr. T. O. Mohieldin

Dr. A. S. Roberts, Jr.

Dr. S. N. Tiwari

ABSTRACT

NUMERICAL PREDICTION OF TURBULENT DIFFUSION FLAMES FORMED BY CYLINDRICAL TUBE INJECTOR

Ali Kheireddine
Old Dominion University, 1996
Director: Dr. S. K. Chaturvedi

This work summarizes numerical results for a diffusion flame formed from a cylindrical tube fuel injector, issuing gaseous fuel jet vertically in a quiescent atmosphere. Both pure fuels as well as fuel mixtures are examined. The primary objective is to predict the flame base height as a function of the jet velocity. A finite volume scheme is used to discretize the time-averaged Navier-Stokes equations for the reacting flow, resulting from the turbulent fuel jet motion. The turbulent stresses, and heat and mass fluxes are computed from the Reynolds stress turbulence model. A chemical kinetics model involving a two-step chemical reaction mechanism is employed for the oxidation of methane. The reaction rate is determined from a procedure which computes at each point the minimum (process limiting) rate from an Arrhenius (kinetically controlled) expression and the eddy dissipation (turbulent mixing controlled) model. The Reynolds stress model (RSM), in conjunction with the two-step kinetics and the eddy dissipation model, produces flame base height and other flame characteristics that are in good agreement with experimental results. Numerical results are also in agreement with the hypothesis of

Vanquickenborne and van Tiggelen concerning the stabilization mechanism of lifted diffusion flames. Furthermore, computed results also indicate that the flame base location can be approximately located by consideration of the turbulent mixing of the fuel jet in the non-reacting case.

For propane, numerical results , obtained using one-step kinetics, show good agreement with the experimental data. Results pertaining to a methane-hydrogen mixture are obtained by using the RSM with three-step kinetics and the eddy dissipation model. The results for pure fuels and fuel mixtures indicate that the lift-off height for all the fuels considered in this study increases linearly with respect to the jet exit velocity.

The study also analyzes the effect of swirling motion on the flame stabilization characteristics of the methane jet. The characteristics of methane flame are also determined by another combustion model which employs the probability density function (PDF) in conjunction with the flame sheet model. Results from this model differ in the near field from those predicted from the RSM-eddy dissipation model. However, in the far field the two combustion models yielded results that are in good agreement.

ACKNOWLEDGMENTS

I would like to express my sincere appreciation to my advisor, Professor S. K. Chaturvedi for his encouragement and valuable guidance during the course of this study. I would also like to thank my research guidance committee members, Drs. T. O. Mohieldin, A. S. Roberts, Jr., and S. N. Tiwari, for their helpful comments that improved my research. My deepest gratitude to my parents, Saleh and Zeinab, my brother and sisters for their patience and continuous support.

TABLE OF CONTENTS

NOMENCLATURE

Latin symbols

A	empirical constant, 4; also pre-exponential factor
a	strain rate, s^{-1}
B	empirical constant, 0.5
b	burnout rate
C	molar concentration
c_p	specific heat, J/kg.K
d	fuel jet diameter, m
E	activation energy
f	mixture fraction
g	scalar variance, $g=f''^2$
g_i	gravitation acceleration, m/s^2
h	lift-off height, m
h_i	specific enthalpy of species i
I	turbulence intensity
k	turbulent kinetic energy, m^2/s^2; also thermal conductivity
L	characteristic length
l	turbulent length scale
M	molecular weight

m	mass fraction
p	pressure, Pa
R	reaction rate
R	universal gas constant
R_l	turbulence Reynolds number
r	radial direction, m
Sc	Schmidt number
S_l	laminar flame speed, m/s
S_t	turbulent flame speed, m/s
T	temperature, K
u	axial velocity component, m/s
u'	root mean square fluctuation velocity, m/s
V	volume, m^3
v	radial velocity component, m/s
x	axial direction, m
Z	Shvab-Zeldovich function

Greek symbols

δ_{ij}	Kronecker delta
ϵ	turbulent kinetic energy dissipation
μ	molecular viscosity, kg/m.s
ν	stoichiometric coefficient; also kinematic viscosity, m^2/s
ρ	fluid density, kg/m^3

σ_h, σ_m	turbulent Schmidt/Prandtl numbers
ϕ	generalized scalar quantity
χ	scalar dissipation rate

Subscripts

eff	effective
fu	fuel
l	laminar
o	inlet condition
ox	oxidizer
P	product
R	reactant
st	stoichiometry condition
t	turbulent

LIST OF TABLES

LIST OF FIGURES

Chapter 1

INTRODUCTION

The gaseous flames have always been a challenging and important phenomenon to analyze. They are classified as either premixed or non-premixed (diffusion) flames, depending on the state of mixedness of the reactants when they reach the flame zone. Each class of flames, premixed or non-premixed, has its own characteristics and applications. In premixed flames, the air and fuel are thoroughly mixed in a required ratio before combustion takes place. Due to the fact that the chemical reaction time is larger than the mixing time, these flames are important in exploring the global reaction rate, the flame speed, flame ignition and extinction. In addition, premixed flames also have applications in internal combustion engines, and in the analysis of scramjet engines.

Diffusion flames, on the other hand are encountered in more practical combustion devices than premixed flames. These flames have been studied extensively due to their wide range of applications in industrial and residential gas furnaces, and jet engine combustors. In diffusion flames, the fuel and air are introduced in separate streams into the combustion chamber and the rate of burning is mainly controlled by the rate of diffusion of fuel into air, due to either the molecular mixing in laminar diffusion flames or the turbulent mixing in turbulent diffusion flames.

The vast majority of the diffusion flames in practical applications are turbulent. Turbulence enhances the rates of chemical reaction by increasing transport properties for heat, mass, and momentum transfer. However, the computational modelling of these flames is one of the most challenging tasks due to the closure problem. Also, the interaction between turbulence and chemical kinetics needs to be properly modeled. The advances in computer architecture and more efficient algorithms, make it possible to numerically investigate a wide spectrum of combustion problems. The emerging field of Computational Fluid Dynamics (CFD), due to recent progress in computational techniques and turbulence modeling, has now the capability of analyzing combustion problems using a variety of turbulence models ranging from a simple zero equation model (Prandtl mixing length) to more complex Reynolds Stress models. The CFD schemes such as un-split MacCormack, power law and second order upwind schemes have been successfully developed and employed in a variety of numerical algorithms. One of the most widely known algorithm, SIMPLE [1][1], has been used extensively in many fluid flow and combustion problems. The main advantage of this algorithm is that it accounts in a simple way for the coupling between pressure, velocity and chemical species equations.

The interaction between turbulence and chemical reactions needs to be taken into account by the use of a variety of chemistry models. Chemistry models such as fast (equilibrium) chemistry, reduced or detailed kinetic mechanisms, assumed shape PDF (Probability Density Function)/flamelet, and eddy break-up models are commonly used to analyze combustion systems. Applications of some of these models are limited and depend on the nature of the problem. For example, detailed finite rate kinetics schemes are ideal for simple geometries governed by one or two dimensional laminar flows. But

---

[1] Number in brackets indicate references.

in practical combustion devices, such as furnaces and gas turbine combustors, the problem is further complicated due to multi-dimensionality as well as the interaction between turbulence and kinetics. Thus less sophisticated representations of kinetics models, such as fast chemistry or reduced kinetic mechanisms, have to be used because of computer storage capacity limitations. Other combustion models such as PDF /flamelet model or the eddy dissipation model, take into account effects of turbulent fluctuation for calculation of chemical reaction rates. These reaction rates are coupled with the kinetics and turbulence parameters and play an important role in predicting near field phenomena such as the flame lift-off height, the flame stability and the flame structure. One of the contributions of this work is to establish the validity of these reduced kinetics models and several turbulence models to assess their applicability to the flame lift-off phenomena in diffusion flames.

Although a great deal of research has been devoted to the study of flame lift-off in turbulent diffusion flames, the physical mechanisms responsible for flame stabilization are still controversial. A review by Pitts [2] summarizes published experimental and theoretical results. His study concluded that neither theoretical nor experimental characterization of flame stabilization is sufficient to determine the actual physical processes that determine lift-off and blowout. Consequently, numerical prediction of flame lift-off height and flame structure are pursued in this study.

1.1 Background Literature

In recent years, considerable research efforts has been directed towards developing theories to analyze the lift-off phenomenon in diffusion flames. Prediction of flame lift-off height is important in the design of combustors, and in the determination of thermal loads on the flame holders and other combustor surfaces. Two distinct approaches have been pursued in the literature to explain the observed flame lift-off phenomenon. The classical approach, due to Vanquickenborne and van Tiggelen [3], assumes that a premixed fuel-air mixture occurs at the flame base. According to their model, flame propagation, with turbulent flame speed into the oncoming flow results in a stably lifted flame at a location where the flame speed equals the local flow velocity. Other studies subscribing to the premixed flame base concept include the work of Gunther et al. [4], Annushkin and Sverdlov [5], Hall et al. [6] and Kalaghatgi [7]. Kalaghatgi successfully correlated his experimental results of flame lift-off height by applying the flame stability model of Vanquickenborne and van Tiggelen [3], and the dimensional analysis. More recently, Comer, Mohieldin and Tiwari [8] have investigated the turbulent lifted flames for methane issuing from a cylindrical tube into still air. Their experiment provided data for the variation of flame base height as function of fuel jet velocity for comparison with numerical results.

The concept of premixed flame base has been challenged by others who contend that it is unlikely that, based on characteristics diffusion length and time scales, sufficient mixing of fuel and air would occur at molecular level near the flame base. A recent development in combustion modelling has been the emergence of the laminar flamelet concept to predict the flame lift-off height in turbulent diffusion flames. Although several related ideas have been proposed, the central thesis of these newly proposed models is that the absence of a flame near the fuel injection point is due to extinction of laminar flamelets. Prominent studies following this approach are due to Peters [9], Janika and Peters [10], and Peters and Williams [11]. These studies use the flamelet model to relate the local composition to the local mixture fraction and its dissipation rate. More recently Sanders and Lamers [12] have used the theory of Peters and Williams [11] while considering the strain rate of smallest eddies as the parameter describing the flame stretch. On the other hand, Bradley et al. [13] proposed an alternative approach for predicting lift-off height of turbulent diffusion flames, where combustion is considered to take place in a premixed mode in the diffusion flames. At a given mixture fraction within flammability limits, a premixed flame is established. This model is called mixedness-reactedness, flamelet model. The drawback of the models described above involves calibration of the empirical constants in the models so that the lift-off height is satisfactory predicted. For example, Sanders and Lamers [12] reported that the sensitivity of the predicted lift-off height depends on the choice of the dissipation rate coefficient. Other discrepancy reported in the above study indicates that the computed temperature field near the center axis of the flame differed significantly from that predicted by Bradley et al. [13]. The flamelet profile used in these studies is usually taken from experimental measurements or is based on detailed theoretical calculations of thin laminar diffusion flames.

The thin laminar diffusion flame provides a one-to-one correspondence between any local scalar property (temperature, density, viscosity and species compositions) and the local value of the mixture fraction. This relationship would prevail within the turbulent reacting flows. Tsuji and Yamaoka [14] were the pioneers to experimentally investigate the thin laminar flame. They studied the porous cylinder counter diffusion flame where the fuel is emitted from a porous cylinder into an oncoming stream of air. A free stagnation line parallel to the cylinder axis forms in front of the cylinder's porous surface, and the combustion takes place within a thin flame zone when fuel and oxidizer are in proper proportion. This produces a unique relationship between the scalar variables and the mixture fraction. Other researchers [15-18] have also investigated the laminar flamelet concept experimentally, and their results represent important contributions to turbulent reactive flows. Theoretical and numerical investigation of laminar counterflow flame have been reported by Dixon-Lewis et al. [19] who have outlined a similarity solution that allows the problem to be treated as one-dimensional in space. Their results for the methane-air flames showed good agreement with the experimental observations of Tsuji and Yamaoka [14]. Keyes and Smooke [20] and Smooke and coworkers [21-24] have also studied the laminar flamelet and their application to turbulent reacting flows. In Ref. 20 a simplified flame sheet model with one step chemical reaction rather than detailed kinetics models has been developed to reduce the modeling complexity and the computation time needed for calculations. Kee et al. [25] and Miller et al. [26-30] have contributed in the development of a detailed subroutine library known as CHEMKIN that uses a complex chemistry and detailed formulation of the transport fluxes. CHEMKIN has been used extensively in Refs. 19-24 to provide the thermodynamic properties and the chemical production rates for hydrocarbon fuels.

Recently Rokke et al. [31] and Sonju and Hustad [32] have experimentally investigated the partially premixed flames which showed good general agreement with the flamelet theory presented by Peters [9]. The fluctuations in the local mixture fraction may become separated from each other with pockets of a chemically frozen mixture occurring for large scalar dissipation rates. They found that for smaller fluctuations in the mixture fraction the concentration variations are small enough for a premixed flame to propagate through the mixture. Above certain critical dissipation rate the flamelets will become separated leading to a shift in mechanisms for the lift-off heights.

The eddy dissipation model of Magnussen and Hjertager [33] is an attractive approach that has also been used in theoretical modelling of turbulent combustion problems and to determine flame lift-off and flame structure phenomena [34, 35]. The basic assumption in the model is that the premixed combustion condition exists at the base of the flame. This model relates the rate of combustion to the rate of dissipation of fuel and oxidizer containing eddies, and expresses the rate of reaction by the mean concentration of a reacting species, the turbulent kinetic energy and the rate of dissipation of this energy.

An alternative approach concerning flame base stabilization is due to Broadwell et al. [36]. In their model, the hot gases transported to the edge of the jet by large scale turbulent structures, are re-entrained and ignite the non-reacting eddies of the jet. However, predictions for lift-off distance from this model are not in accord with experimental results.

Numerical calculation involving the above models requires procedures that must incorporate simultaneous treatment of turbulence, chemical reaction, heat transfer, mass and momentum transfer. The turbulence modeling problem has been extensively studied particularly for non-reacting flows. Studies including those by Rodi [37], Bradshaw et al. [38], Jones and Launder [39], Spalding [40] and Mellor et al. [41] represent excellent contributions to development of the mathematical models for turbulent flows, including the k-ϵ model and the Reynolds stress model. A summary of comparison of results from various turbulence models for non-reacting cylindrical jet is presented by Schetz [42]. It is important to note that in all turbulent combustion problems the same constants as those in the non-reacting cases are used. The k-ε model has been used successfully in many studies [43-51]. Although the k-ε model is the very popular and widely used turbulence model in reacting flows applications, it has limitation in predicting accurate results in some practical combustion devices that involve swirling motion. For flows with swirling motion and large streamline curvature, the Reynolds stress model is the model of choice. Studies by Janicka [52] and Weber et al. [53] have employed the Reynolds stress model for the prediction of diffusion flames. These studies showed that the use of the Reynolds stress model was able to improve the accuracy of results as compared to other models such as the k-ε model and the mixing length model.

The interaction between turbulence and chemistry has been taken into account by many researchers who have concluded that kinetic mechanism models have an essential role in reacting flow problems. These models involve detailed kinetic mechanisms and reduced kinetic mechanisms. Most combustion devices use hydrocarbons as fuels, and consequently these fuels have been extensively studied and reported in the literature. Some detailed models [54-57] involve a large number of species that require many transport equations to be solved. However, these models generally do not consider multidimensional flows. As a result, reduced global reaction models are more popular for multi-dimensional turbulent reactive flows. These models range from one-step to four-step reaction mechanisms for methane and propane fuels. Westbrook and Dryer [58] have developed several reduced global mechanisms for a wide variety of hydrocarbon fuels, the most important of these being the one-step and two-step models. These models incorporate procedures for determining global kinetics parameters from experimental flammability limits and stoichiometric flame speed at atmospheric conditions. A single step global reaction model using these parameters has been shown to predict reasonably well the flame speeds over a wide range of equivalence ratios from very lean to very rich. Other approach, pursued by Coffee et al. [59], first solves the equations governing the detailed chemistry model. The overall reaction rate parameters are then found from a least squares fit of the heat released profile. Peters [60], Peters and Kee [61], Dryer and Glassman [62] and Hautmann et al. [63], have also developed global reaction mechanisms for a wide range of combustion problems. In Ref. 58 the two-step reaction model has been developed for a variety of hydrocarbon fuels. In particular, for methane the model has been tested by many researchers [64-67] and has produced reliable results.

1.2 Present Study

This study addresses numerical prediction of the turbulent diffusion flame structure and calculation of flame base lift-off height for cylindrical tube injectors operating in a quiescent environment. The calculations are carried out by using two different techniques that treat the interaction of turbulence and chemistry. The objective is to test the validity of these models and to assess the feasibility of applying turbulence and chemistry models to general combustor flow problems. The first approach revisits a turbulent combustion model, known as the eddy dissipation model, by Magnussen and Hjertager [33], based on the eddy breakup model proposed by Spalding [68]. Although this model is heuristic in nature, and lacks the theoretical foundation of the flamelet concept, it does offer a simple way of treating chemical reaction rates in turbulent combustion. The reaction rate at any point in the flow field is calculated from the eddy dissipation model and the Arrehenius expression, depending on whether the reaction is diffusion or kinetically controlled. The lower of these rates determines the process limiting rate. Selection of turbulence model would have an impact in predicting k and ϵ values that are used in the eddy dissipation model. In regions away from the injection point, as reported by Magnussen and Hjertager [33], Mohieldin and Chaturvedi [35] and Mohieldin [66], the eddy dissipation model in conjunction with the k-ϵ turbulence model produces results that are in good agreement with reported experimental results. However, success of this model in predicting near field phenomenon such as flame base height has not been documented in the literature. In the present study, we have used the eddy dissipation model in conjunction with the k-ϵ model and the Reynolds Stress Model, to predict the base flame lift-off height, flame structure, and the near field and far field product concentrations. When the reaction is kinetically controlled, the rates are determined from the Arrehenius kinetic rate expression. Two global kinetics models, namely one step and two step models, are used in this study to compute the reaction rates. In the single-step model, the hydrocarbon fuel is oxidized into carbon dioxide and water. In the two step model, the first step oxidizes the fuel into carbon monoxide while the second step oxidizes it to carbon dioxide.

The second approach for prediction of diffusion flames employs the probability density function (PDF) and the flame sheet model. Unlike the previous approach, which requires the solution of each individual species transport equation, a single conserved scalar (the mixture fraction) transport equation is solved and individual component concentrations are derived from the predicted mixture fraction. The interaction of turbulence and chemistry are accounted by the probability density function. This approach assumes the flow to be incompressible and turbulent, and is suited for non-premixed flames that are generated by separated fuel and oxidizer streams. Even though the model is advanced and possesses the theoretical foundation of laminar flamelet concept, it is still not at a stage where it is useful for engineering calculations involving practical combustion systems. In this study we have used this model to compare its results with those predicted from the eddy dissipation model.

Chapter 2 describes the physical configuration, the mathematical formulation and the turbulent combustion models. The numerical discretization and solution procedure for the equations governing the turbulent reacting flows are discussed in Chap. 3. Chapter 4 presents results for a methane fuel jet issuing in a quiescent atmosphere. This chapter also features the grid independency, and the computer code validation for non-reacting as well as reacting flows. The effect of jet exit diameter and fuel type are investigated in Chap.

5. This chapter also discusses the results obtained by considering the PDF/Flame sheet approach in modeling the turbulent reacting flows problems. Chapter 6 presents the conclusions of the study.

Chapter 2

PHYSICAL CONFIGURATION AND TURBULENT COMBUSTION MODELS

This chapter introduces the present problem and describes the physical configuration considered in this study. Later in the chapter, the mathematical formulation for the turbulent reacting flows is discussed. The problem addressed in this study is a challenging one due to a number of reasons. First, the flow is turbulent which makes the analysis of the phenomenon difficult even in the non-reacting flows regime. Also, in reacting flows several aspects such as the closure and interaction between chemistry and turbulence need to be treated. Furthermore, the governing equations in realistic configurations are very complicated and are usually solved numerically. Two approaches are generally used in solution of turbulent flows. In the direct numerical simulation (DNS), a complete solution of the Navier-Stokes equations is implemented. However, this approach is prohibitively expensive and presently restricted only to cases with small Reynolds and Damkohler numbers. Filtered statistical approaches, such as the large eddy simulation (LES) or vortex methods, model the small scales at which the molecular transport and chemical reaction takes place. Unfortunately, these methods are still very expensive and limited to simple geometries. The other approach used in turbulent flow problems is based on averaging of the transport equation for momentum, energy and species. For constant density flows or flows with small density changes, a time weighted averaging procedure known as the Reynolds averaging is employed. In flows with significant density variation, a density weighted averaging procedure known as the Favre averaging is more suitable. However, both averaging procedures are characterized by appearance of higher order correlations of fluctuations of flows properties. This, in turn, requires modeling of these correlations, also known as the Reynolds stresses. This is also known as the closure problem in the literature. Several levels of turbulence models have been introduced to address the closure problem. Although the k-ε turbulence model has emerged as a reasonably good model for many engineering calculations of both non-reacting and reacting flow problems, it has its limitations specially in applications involving swirling flows and strong curvature of stream lines. For these and other applications, the RSM appears to be a more appropriate turbulence model. The k-ε model relates the individual Reynolds stresses to the mean flow gradients with the aid of the eddy viscosity. The RSM on the other hand predicts the individual stress terms directly by solving transport equations for Reynold stresses which leads to more accurate results than those obtained from the k-ε model.

The next challenging task in modeling of reacting flows is the stiffness problem encountered as a result of various scales of turbulence and their influence on chemical reactions in gaseous diffusion flames. Even in simple fuels such as methane, the kinetic mechanisms involves several dozen intermediate chemical reactions. In realistic reacting flow problems in three-dimensions, it would be impossible to analyze the coupled flow, turbulence and chemistry consideration with several intermediate species. Consequently, the emphasis of recent combustion research has been to develop global kinetic reaction models with one, two ar four reactions. Most recent studies have employed either global one-step or two-step reaction mechanism to solve problems of turbulent combustion. In the present study, we have employed both a single-step and a two-step chemical reaction to model combustion. The turbulence effects are modeled by employing both the k-ε model and the RSM. Features of these models together with the description of the physical configurations are discussed in the next section.

2.1 Physical Models

This study specifically deals with turbulent non-premixed flames. The diffusion flame is formed by a cylindrical injector similar to the one used in the experimental studies performed by Vanquickenbourn and van Tiggelen [3], Kalaghatagi [7] and Comer et al. [64]. The numerical domain used in the present study is depicted in Fig. 2.1. A circular tube of 0.46 cm inside diameter, and 0.1 meter in length is used as a fuel injector. The tube has a wall thickness of 0.089 cm. The fuel is injected vertically in a quiescent atmosphere. The gas jet entrains the surrounding air, and the combustion ensues at a short distance from the tube opening. The flame base height (h), measured as the axial distance between tube opening and the base of the flame (Fig. 2.1), depends on several parameters, namely the type of fuel, fuel jet velocity and the tube diameter. In order to assess the effect of these parameters numerically, a computational domain of 0.29 meter in diameter and 0.58 meter in length was chosen. Effects of various parameters governing the flame base height and other flame characteristics are analyzed by solving governing equations that are described in the next section.

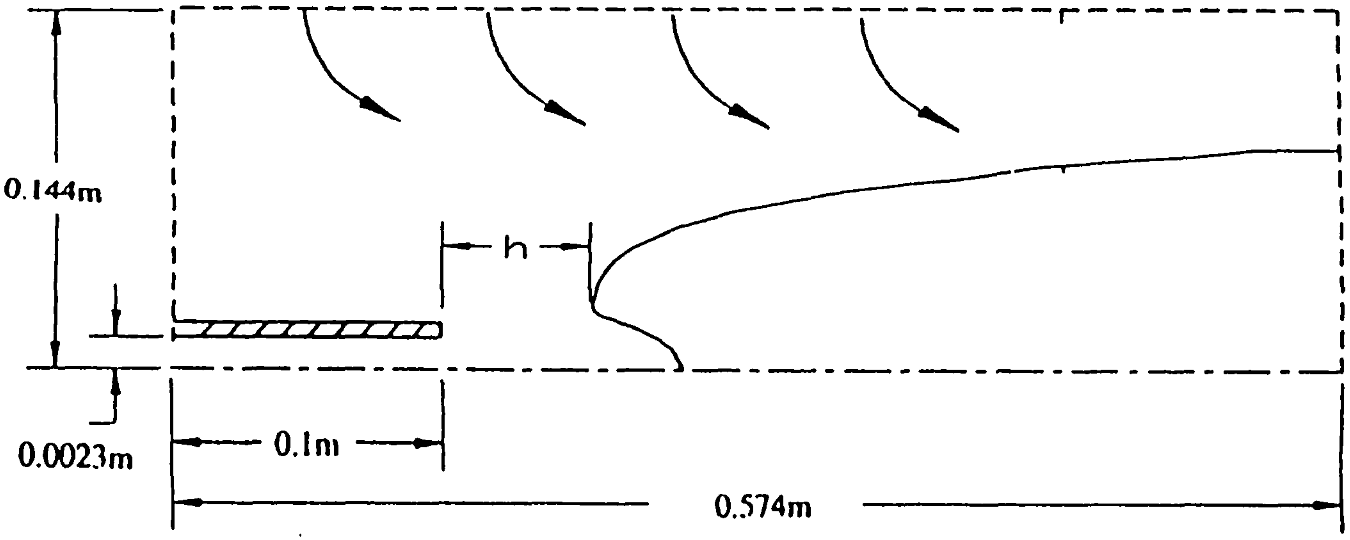

Fig. 2.1 Schematics of the lifted turbulent diffusion flame.

2.2 Basic Governing Equations

The physical model illustrated in the previous section can be analyzed theoretically or experimentally. In the present study the theoretical approach is adopted and the results are compared with the existing experimental data. The fluid motion, heat transfer and species concentrations are governed by the Navier-Stokes equations and species transport equations. The fuel jet Reynolds number ranges from 6000 to 15,000 for the methane jet, and 10,000 to 30,000 for the propane jet, and the flow is essentially turbulent [68]. In the analysis turbulent flows the physical quantities are decomposed into mean and fluctuating components. Two distinctive decomposition techniques can be used: namely density un-weighted Reynolds averaging and the density-weighted Favre averaging. Both techniques have been investigated and compared for reacting flows problems by many researchers. Studies by Jones [69] and more recently by Soong et al. [70] demonstrated both techniques for confined and unconfined jet diffusion flames. Soong et al. [70] concluded that the results predicted from the Reynolds averaging compared better with the experimental results than the ones predicted by the density-weighted (Favre averaging). In this study we have employed the time-averaged (Reynolds) to predict the flow characteristics. As a result, a fluctuating variable is expressed as the sum of the density-un-weighted time averaged part and a fluctuating part.

$$\phi_i(x_i,t) = \overline{\phi_i(x_i)} + \phi'(x_i,t) \tag{2.1}$$

where ϕ denotes the physical quantities (u, p, ρ, h & m), the term ϕ is the mean quantity and ϕ' the fluctuating quantity measured from the mean.

Since the physical configuration considered in the study has cylindrical symmetry, the governing equations for turbulent reacting flow in the cylindrical coordinate (omitting the bars) can be expressed as follows:

Continuity

$$\frac{\partial}{\partial x}(\rho u) + \frac{1}{r}\frac{\partial}{\partial r}(r\rho v) = 0 \tag{2.2}$$

x-Momentum

$$\begin{aligned}\frac{\partial}{\partial x}(\rho u u) + \frac{1}{r}\frac{\partial}{\partial r}(r\rho u v) &= \frac{\partial p}{\partial x} + \frac{\partial}{\partial x}\left(\mu\frac{\partial u}{\partial x} - \rho\overline{u'u'}\right) \\ &+ \frac{1}{r}\frac{\partial}{\partial r}\left(r\mu\frac{\partial u}{\partial r} - \rho\overline{u'v'}\right) + S_u\end{aligned} \tag{2.3}$$

r-Momentum

$$\begin{aligned}\frac{\partial}{\partial x}(\rho u v) + \frac{1}{r}\frac{\partial}{\partial r}(r\rho v v) &= \frac{\partial p}{\partial x} + \frac{\partial}{\partial x}\left(\mu\frac{\partial v}{\partial x} - \rho\overline{u'v'}\right) \\ &+ \frac{1}{r}\frac{\partial}{\partial r}\left(r\mu\frac{\partial v}{\partial r} - \rho\overline{v'v'}\right) + S_v\end{aligned} \tag{2.4}$$

Energy

$$\begin{aligned}\frac{\partial}{\partial x}(\rho u h) + \frac{1}{r}\frac{\partial}{\partial r}(r\rho v h) &= \frac{\partial}{\partial x}\left(\frac{k}{c_p}\frac{\partial h}{\partial x} - \rho\overline{u'h'}\right) \\ &+ \frac{1}{r}\frac{\partial}{\partial r}\left(r\frac{k}{c_p}\frac{\partial h}{\partial r} - \rho\overline{v'h'}\right) + \sum h_j R_j\end{aligned} \tag{2.5}$$

Mass Transport

$$\begin{aligned}\frac{\partial}{\partial x}(\rho u m_j) + \frac{1}{r}\frac{\partial}{\partial r}(r\rho v m_j) &= \frac{\partial}{\partial x}\left(\frac{\mu}{S_c}\frac{\partial m_j}{\partial x} - \rho\overline{u'm_j'}\right) \\ &+ \frac{1}{r}\frac{\partial}{\partial r}\left(r\frac{\mu}{S_c}\frac{\partial m_j}{\partial r} - \rho\overline{v'm_j'}\right) + R_j\end{aligned} \tag{2.6}$$

Equations (2.2) - (2.6) govern the turbulent motion while neglecting density fluctuation terms. The axial and radial mean velocity components are denoted by u and v

respectively, h is the mixture enthalpy and h_j is the enthalpy of species j. Symbols c_p, μ and k are the specific heat, molecular viscosity, and conductivity of the fluid mixture respectively. The mass fraction and the production rate of species j are represented by m_j and R_j respectively. Calculation of R_j is discussed in some detail in a later section. The terms S_u and S_v are given in Table 2.1. Thermodynamics properties such as the mixture enthalpy, the mixture specific heat and the mixture density are calculated as follows:

$$h = \sum_j m_j (h_j^o + h_j) = \sum_j m_j (h_j^o + \int_{T_{ref}}^{T} c_{pj}(T) dT)$$

$$c_p = \sum_j m_j c_{pj}(T)$$

$$\rho = \frac{P}{\bar{R} T \sum_j \frac{m_j}{M_j}}$$

where c_{pj} and h_j^o are the specific heat and the enthalpy of formation of species j, respectively.

2.3 Turbulence Models

Equations (2.2)- (2.6) can be expressed in a compact form as (omitting the bars)

$$\frac{\partial}{\partial x}(\rho u \phi) + \frac{1}{r}\frac{\partial}{\partial r}(r \rho v \phi) = \frac{\partial}{\partial x}\left(\Gamma_\phi \frac{\partial \phi}{\partial x} - \rho \overline{u' \phi'}\right) + \frac{1}{r}\frac{\partial}{\partial r}\left(r \Gamma_\phi \frac{\partial \phi}{\partial r} - \rho \overline{v' \phi'}\right) + S_\phi \quad (2.7)$$

The expressions for ϕ, Γ_ϕ and S_ϕ for various variables are described in Table 2.1. The stresses $-\rho\overline{u'\phi'}$ and $-\rho\overline{v'\phi'}$ are additional unknowns. It is evident that Eq. (2.7) represents a set of transport equations that include more variables than equations. This means that the system is not yet closed. To achieve closure, one must find enough equations to solve for the unknowns. This closure problem is resolved through modeling of the Reynolds stresses. Two well known turbulence models are used in the present study, namely the k-ϵ Model and the Reynolds stress model (RSM).

The k-ϵ Model

This model has been the leading choice for solving various turbulent flow problems. The model computes both the turbulent kinetic energy and the turbulence scale by solving transport equations for these quantities. The starting point of the k-ϵ model is the Boussinesq approximation in which turbulent stresses are expressed in terms of a turbulent viscosity and the strain rate.

$$-\rho\overline{u_i'u_j'} = \mu_t\left(\frac{\partial u_i}{\partial x_j} + \frac{\partial u_j}{\partial x_i}\right) + \frac{2}{3}k\delta_{ij} - \frac{2}{3}\rho k\delta_{ij} \tag{2.8}$$

$$k = \frac{1}{2}\sum\overline{u_i'u_i'} \tag{2.9}$$

Table 2.1 Conservation terms corresponding to Eq. (2.6)

Cons. of	ϕ	Γ_ϕ	S_ϕ
Mass	1	0	0
x-Momentum	u	μ	$-\frac{\partial p}{\partial x} + S_u$
r-Momentum	v	μ	$-\frac{\partial p}{\partial r} + S_v$
Energy	h	$\frac{k}{c_p}$	$\Sigma h_j R_j$
Mass Fraction	m_j	$\frac{\mu}{Sc}$	R_j

$$S_u = \rho g + \frac{\partial}{\partial x}\left(\mu\frac{\partial u}{\partial x}\right) + \frac{1}{r}\frac{\partial}{\partial r}\left(r\mu\frac{\partial v}{\partial x}\right) \qquad S_v = \frac{\partial}{\partial x}\left(\mu\frac{\partial u}{\partial r}\right) + \frac{1}{r}\frac{\partial}{\partial r}\left(r\mu\frac{\partial v}{\partial r}\right) - 2\mu\frac{v^2}{r}$$

Symbols μ_t and k represent the eddy viscosity and the turbulent kinetic energy, respectively. The eddy viscosity μ_t, in contrast to the molecular viscosity μ, is not a fluid property but depends strongly on the local state of turbulence. The turbulence viscosity μ_t, and the turbulence length scale, l, are expressed in terms of the turbulent kinetic energy (k) and the dissipation rate (ϵ) as

$$\mu_t = \rho C_\mu \frac{k^2}{\epsilon}, \qquad l = C_\mu \frac{k^{3/2}}{\epsilon} \tag{2.10}$$

The k transport equation is derived by taking the trace of the transport equations for Reynolds stresses, while the ε equation is a modeled one. Equations used in the present study are identical to those reported by Launder and Spalding [44], i. e.,

$$\begin{aligned} \frac{\partial}{\partial x}(\rho u k) + \frac{1}{r}\frac{\partial}{\partial r}(r \rho v k) &= \frac{\partial}{\partial x}\left(\frac{\mu_t}{\sigma_k}\frac{\partial k}{\partial x}\right) + \frac{1}{r}\frac{\partial}{\partial r}\left(r\frac{\mu_t}{\sigma_k}\frac{\partial k}{\partial r}\right) \\ &+ G_k + G_b - \rho\epsilon \end{aligned} \tag{2.11}$$

$$\begin{aligned} \frac{\partial}{\partial x}(\rho u \epsilon) + \frac{1}{r}\frac{\partial}{\partial r}(r \rho v \epsilon) &= \frac{\partial}{\partial x}\left(\frac{\mu_t}{\sigma_t}\frac{\partial \epsilon}{\partial x}\right) + \frac{1}{r}\frac{\partial}{\partial r}\left(r\frac{\mu_t}{\sigma_t}\frac{\partial \epsilon}{\partial r}\right) \\ &+ C_{1\epsilon}\frac{\epsilon}{k}\left(G_k + (1 - C_{3\epsilon})G_b\right) - C_{2\epsilon}\rho\frac{\epsilon^2}{k} \end{aligned} \tag{2.12}$$

where C_μ, $C_{1\epsilon}$, $C_{2\epsilon}$, $C_{3\epsilon}$, σ_k and σ_ϵ are empirical constants that are given in Table 2.2. Symbols G_k and G_b are the rate of production of turbulent kinetic energy and the generation of turbulence due to buoyancy. These terms are expressed as

$$G_k = \mu_t\left(\frac{\partial u_i}{\partial x_j} + \frac{\partial u_j}{\partial x_i}\right)\frac{\partial u_i}{\partial x_j}$$

$$G_b = -g_i \frac{\mu_t}{\sigma_h} \frac{\partial \rho}{\partial x_i}$$

The terms $-\rho \overline{u'\phi'}$ and $-\rho \overline{v'\phi'}$, where ϕ' is h in the energy equation or m in the species conservation equation, are expressed interms of gradient of the respective mean quantities h and m_j as

$$-\rho \overline{u_i' h'} = \frac{\mu_t}{\sigma_h} \frac{\partial \bar{h}}{\partial x_i} \tag{2.13}$$

$$-\rho \overline{u_i' m_j'} = \frac{\mu_t}{\sigma_m} \frac{\partial \overline{m_j}}{\partial x_i} \tag{2.14}$$

where σ_m and σ_h are the turbulent Schmidt and Prandtl numbers, respectively. Their values are determined empirically, and a value of 0.7 is used for both σ_m and σ_h.

Reynolds Stress Model (RSM)

In many reacting flow problems, such as the one considered in the present study, the velocity and time scales vary significantly. Consequently, the k-ε model becomes inadequate for making reliable predictions. Also, in flows with swirl component and streamline curvature, the Reynolds stress model, which computes the individual stresses $-\rho \overline{u_i' u_j'}$ provides a better and a more accurate description of turbulence and flow fields.

Table 2.2 Turbulence model constants

Constants	*Value*
C_μ	*0.09*
C_1	*1.44*
C_2	*1.92*
σ_ϵ	*1.30*
σ_k	*1.0*

For example, Jones [69] has used the Reynolds stress model [71] and has reported greatly improved accuracy in isothermal and reacting flows. Each of the stresses ($-\rho\overline{u_i'u_j'}$) appearing in Eq. (2.7) are governed by transport equations that contain triple order velocity correlations and pressure velocity correlations that must be modeled to obtain closure. One such Reynolds stress model has been employed in Refs. 52 and 69. We have used this model to carry out numerical calculations in the present study. The transport equations for Reynolds stress can be expressed as [72]

$$u_k \frac{\partial \overline{u_i'u_j'}}{\partial x_k} = \frac{\partial}{\partial x_k}\left(\frac{\mu_t}{\rho\,\sigma_k}\frac{\partial \overline{u_i'u_j'}}{\partial x_k}\right) + P_{ij} + \Phi_{ij} - \epsilon_{ij} \tag{2.15}$$

where the stress production rate, pressure-strain correlation, and viscous dissipation terms are given by symbols P_{ij}, Φ_{ij}, andϵ_{ij} respectively

$$P_{ij} = -\left(\overline{u_i'u_k'}\frac{\partial u_j}{\partial x_k} + \overline{u_j'u_k'}\frac{\partial u_i}{\partial x_k}\right)$$

$$\Phi_{ij} = C_3\frac{\epsilon}{k}\left(\overline{u_i'u_j'} - \frac{2}{3}\delta_{ij}k\right) - C_4\left(P_{ij} - \frac{2}{3}\delta_{ij}P\right)$$

$$\epsilon_{ij} = \frac{2}{3}\delta_{ij}\epsilon$$

where C_3 and C_4 are empirical constants taken as 1.8 and 0.6 respectively, and ϵ is governed by Eq. (2.12). The turbulent kinetic energy k is obtained from Eq. (2.9), and the eddy viscosity is calculated from Eq. (2.10). Representations for $-\rho\overline{u_i'h'}$ and $-\rho\overline{u_i'm_j'}$ are identical to those expressed in Eq. (2.13) and Eq. (2.14), respectively.

2.4 Turbulent Combustion Models

Computation of turbulent combustion requires treatment of the different processes such as turbulence, chemical reaction and their interaction. In the previous section we presented the turbulence models used in this study. In this section we discuss the combustion models that have been employed for non-premixed diffusion flame calculations. It has often been argued that for most hydrocarbons, oxidation processes take place in a thin flamelet whose thickness is of the order of the Kolomogrov microscale. Numerical modeling to capture these small turbulent scales requires large number of grid points which in turn leads to a very expensive computational effort. Consequently, several models have been proposed to simplify the turbulence/chemistry interaction. One such model is based on flamelet or flame sheet models where the influence of the turbulence is described by a probability density function (PDF). The other approach is based on the observations that time scales for dissipation of smaller eddies containing fuel and oxygen must determine the reaction rates for mixing control combustion problems. This model is known as the eddy dissipation model [33] and it is closely related in a conceptual sense to another model known as the eddy breakup model [67]. In the present study, we have employed the eddy dissipation model since it yields reasonable results by relating the mixing controlled limiting reaction rate to mean concentration of species and a characteristic time (ε/k) .

Eddy Dissipation Model

The eddy dissipation model has been tested and used successfully in regions away from the injection point [34, 35, 66]. One of the features of this model is that unlike the eddy breakup model it does not call for solution of equations for the concentration fluctuations. Eddy dissipation model is a mixing-controlled combustion technique that allows one to determine the mean reaction rate as a function of the mean concentration field and the characteristic turbulent time. In this model the rate of reaction is given as the smallest of the two expressions below [33]:

$$
\begin{aligned}
R_{j,k} &= \nu_{j,k} M_j A\, \bar{\rho} \frac{\epsilon}{k} \frac{m_R}{\nu_{R,k} M_R} \\
R_{j,k} &= \nu_{j,k} M_j A B\, \bar{\rho} \frac{\epsilon}{k} \frac{\sum_P m_P}{\sum_P \nu_{P,k} M_P}
\end{aligned}
\qquad (2.16)
$$

where $\nu_{j,k}$ is the molar stoichiometric coefficient for species j in reaction k, and A and B are empirical constants equal to 4 and 0.5, respectively. The time scale of the turbulent eddies is represented by ϵ/k. Subscripts R and P denote reactants and products respectively and M is the molecular weight of each species. In a kinetic controlled combustion process, the reaction rate is represented by an Arrhenius type formulation, i. e.,

$$
R_{j,k} = -\mu_{j,k} M_j T^{\beta_k} A_k C_{fu}^{\alpha} C_{ox}^{\beta} e^{-\frac{E}{RT}} \qquad (2.17)
$$

where β_k is a temperature exponent, A_k is the pre-exponential factor, E_k represents the activation energy, and C_{fu} and C_{ox} are the molar concentration of fuel and oxidizer. Symbols α and β are concentration exponents. For reduced global reactions the values of α and β are determined empirically while for detailed reactions their values would be same as stoichiometric coefficients. The reaction rate in Eq. (2.17) is calculated from reduced global kinetics models. These model will be discussed in the following section.

In turbulent reacting flows, both reaction rates from the Arrehenius expression, Eq. (2.17), and the eddy dissipation model, Eq. (2.16), are calculated and the minimum of the two is used as the process limiting combustion rate. The source term that appears in the enthaply and mass species equations is determined by the following expression

$$R_j = \sum_k R_{j,k}$$

Kinetics Models

A global mechanism that describes the oxidation of fuel in a single-step or multi-step reaction is important and practical concept in turbulent reacting flow problems. As stated earlier, the interaction between turbulence and chemistry creates severe modeling difficulties. A number of investigators, including Dryer and Glassman [62], Westbrook and Dryer [58], Hautman et al. [63] and Coffee et al. [57] have proposed global or quasi-global reaction schemes optimized for a particular flame feature such as burning velocity [62], thermal profile [57], or particular experimental configurations [58, 63]. In this study, we have used a single and two-step reaction model for methane, a single- step for propane and a three-step model for a mixture of methane and hydrogen.

One Step Model

In a global single step mechanism the hydrocarbon fuel such as methane and propane is oxidized to carbon dioxide and water without taking into account the intermediate species such as (CO, H_2, OH, *etc.*). The reaction for methane is expressed as [62]

$$CH_4 + 2O_2 \rightarrow CO_2 + 2H_2O \tag{2.18}$$

The reaction rate in Eq. (2.17) for methane is rewritten in the following form

$$R_{CH_4} = M_{CH_4} A C_{CH_4}^{\alpha} C_{O_2}^{\beta} e^{-\frac{E}{\bar{R}T}} \tag{2.19}$$

where M_{CH4} is the molecular weight of methane and C_{CH4} and C_{O2} are the concentrations of methane and oxygen, respectively. Symbols A, α and β are empirical constants that are taken from kinetics model discussed by Dryer and Glassman [62]. These constants are listed in Table 2.3. The activation energy, E, is also determined empirically and its value is given in Table 2.3. The reaction rates for O_2, CO_2 and H_2O are determined from the law of mass action.

For the propane fuel mechanism, the rates are described in a manner similar to the one for methane. The model used in this study is from by Westbrook and Dryer [58] and the overall reaction and reaction rates can be expressed as

$$\begin{gathered} C_3H_8 + 5O_2 \rightarrow 3CO_2 + 4H_2O \\ R_{C_3H_8} = M_{C_3H_8} A_1 C_{C_3H_8}^{\alpha_1} C_{O_2}^{\beta_1} e^{-\frac{E_1}{\bar{R}T}} \end{gathered} \tag{2.20}$$

Constants in the model are given in Table 2.4. The expression of reaction rates for O_2, CO_2 and H_2O are determined from the law of mass action..

Two-Step Reaction

This mechanism is more detailed compared to the model presented earlier, and can predict the concentration of carbon monoxide. In the two step reaction model, the first step oxidizes the fuel (methane) into CO while the second step oxidizes it to CO_2. The formation of CO is the rate limiting process that also slows the heat release from the fuel. This in turn is reflected in a slower temperature rise and a consequent increase in the flame base height. These reactions are expressed as [58]

$$CH_4 + \frac{3}{2}O_2 \rightarrow CO + 2H_2O$$
$$CO + \frac{1}{2}O_2 \rightarrow CO_2$$

The reaction rate, Eq. (2.17), is rewritten as

$$\begin{aligned} R_{CH_4} &= M_{CH_4} A_1 C_{CH_4}^{\alpha_1} C_{O_2}^{\beta_1} e^{-\frac{E_1}{\bar{R}T}} \\ R_{CO} &= M_{CO} A_2 C_{CO}^{\alpha_2} C_{O_2}^{\beta_2} e^{-\frac{E_2}{\bar{R}T}} \end{aligned} \qquad (2.22)$$

The empirical constants α_1, β_1, E_1, α_2, β_2, and E_2 are given in Table 2.5.

Three Step Model

In the present study we have investigated the combustion of fuel mixtures. The chemical reaction mechanism for the mixture of methane and hydrogen is modeled by

Table 2.3 One-step model for methane/air reaction

Constant	R_{CH_4}
A_I (kg/m^3-s)	1.60×10^{17}
E_I (J/kg-mole)	2.02312×10^{8}
α_I	0.7
β_I	0.8

Table 2.4 One-step model for propane/air reaction

Constant	$R_{C_3H_8}$
A_I (kg/m^3-s)	3.76×10^{16}
E_I (J/kg-mole)	1.25604×10^{8}
α_I	0.1
β_I	1.65

Table 2.5 Two-step model for methane/air reaction

Constant	R_{CH_4}	R_{CO}
k	1	2
A_k	$5.28x10^{15}$	$1.60x10^{10}$
E_k	$2.2403x10^{8}$	$1.03716x10^{8}$
α_k	0.5	1.0
β_k	1.0	1.0

Table 2.6 One-step model for hydrogen/air reaction

Constant	R_{H_2}
A_1 (kg/m^3-s)	$6.32x10^{15}$
E_1 (J/kg-mole)	$1.2263x10^{7}$
α_1	1.6
β_1	1.6

three global reactions including two reactions for methane and one for hydrogen. The reaction mechanism of methane is the same as described in the two-step CH_4 model. The global mechanism of hydrogen and the reaction rate are adapted from the Ref. 73.

$$H_2 + \frac{1}{2} O_2 \rightarrow H_2O$$

$$R_{H_2} = M_{H_2} A_3 C_{H_2}^{\alpha_3} C_{O_2}^{\beta_3} e^{-\frac{E_3}{RT}} \qquad (2.23)$$

The constants α_2, β_3, and E_3 are given in Table 2.6 .

The Mixture Fraction / PDF Model

The mixture fraction / PDF modeling approach involves the solution of the transport equation for a single conserved scalar (the mixture fraction). In this approach, unlike the one presented in the previous section, transport equations for individual species are not solved. The chemical rates are assumed to be very large so that the reaction is completed as soon as the reactants are mixed. The fast chemistry assumption implies that the instantaneous molecular species concentration and temperature are functions only of the mixture fraction (*f*). For a single step hydrocarbon reaction

$$\nu'_F F + \nu'_{O2} O_2 \rightarrow \nu''_{CO_2} CO_2 + \nu''_{H_2O} H_2O$$

The mixture fraction (*f*) is conserved during chemical reactions and is defined by [10]

$$f = \frac{Z - Z_{ox}}{Z_{fu} - Z_{ox}} \qquad (2.24)$$

The subscripts *fu* and *ox* refer to fuel and oxidizer stream conditions at the inlet, and Z is a Shvab-Zoldivich function and is expressed as [11]

$$Z = \frac{\nu Y_F - Y_{O_2} + Y_{ox}}{\nu Y_{fu} + Y_{ox}}$$

where $\nu = \nu'_{O2} M_{O2} / \nu'_F M_F$ and M denotes molecular weight. The individual species concentrations that are usually predicted from Eq. (2.7) can instead be expressed in terms of a conserved scalar f. In this case the chemical source term vanishes, i. e.,

$$\frac{\partial}{\partial x}(\rho u f) + \frac{1}{r}\frac{\partial}{\partial r}(\rho v f) = \frac{\partial}{\partial x}\left(\frac{\mu_{eff}}{\sigma_f}\frac{\partial f}{\partial x}\right) + \frac{1}{r}\frac{\partial}{\partial r}\left(\frac{\mu_{eff}}{\sigma_f}\frac{\partial f}{\partial r}\right) \tag{2.25}$$

The scalar variant $g = f'^2$ is governed by the following equation

$$\frac{\partial}{\partial x}(\rho u g) + \frac{1}{r}\frac{\partial}{\partial r}(\rho v g) = \frac{\partial}{\partial x}\left(\frac{\mu_{eff}}{\sigma_g}\frac{\partial g}{\partial x}\right) + \frac{1}{r}\frac{\partial}{\partial r}\left(\frac{\mu_{eff}}{\sigma_g}\frac{\partial g}{\partial r}\right) + C_{g1}\Phi_g - \rho C_{g2} g \frac{\epsilon}{k} \tag{2.26}$$

where

$$\Phi_g = \mu_t\left[\left(\frac{\partial f}{\partial x}\right)^2 + \left(\frac{\partial f}{\partial r}\right)^2\right]$$

Here the Schmidt's numbers σ_f and σ_g each are taken as 0.7; C_{g1} and C_{g2} are empirical and their values usually taken as 2.86 and 2.0 respectively. The last term in Eq. (2.26) is known as the scalar dissipation rate and is denoted by a symbol χ.

Probability Density Function (PDF)

The probability density function (PDF) is usually described in terms of two parameters f and g. Thus, the time average of any quantity ϕ depends solely on f

$$\bar{\phi}(x) = \int_0^1 \phi(f) P(f,x) df \tag{2.27}$$

In many past studies the PDF, $P(f,x)$, has been described in terms of the beta function. This allows the PDF to be computed at all points in the flow field interms of f only as [65]

$$P(f) = \frac{f^{a-1}(1-f)^{b-1}}{\int_0^1 f^{a-1}(1-f)^{b-1}\,df}$$

where

$$a = \bar{f}\left[\frac{\bar{f}(1-\bar{f})}{g} - 1\right] , \qquad b = \frac{1-\bar{f}}{\bar{f}}\,a$$

The known PDF function $P(f)$ is used as the weighting function to determine the time averaged mean values of species concentrations, density and temperature by substituting $P(f)$ into Eq. (2.27), i. e.,

$$\bar{\phi} = \frac{1}{\beta(a,b)} \int_0^1 \phi(f) f^{a-1} (1-f)^{b-1}\,df \tag{2.28}$$

The flame sheet / flamelet model provides $\phi(f)$ for each species concentration, viscosity, temperature, and density.

Chapter 3

NUMERICAL ASPECTS AND SOLUTION PROCEDURE

In the previous chapter, the governing equations for turbulent reacting and non-reacting flows were discussed. These equations are non-linear and coupled partial differential equations (pdes), for which no analytical solutions exist. Consequently, a numerical approach is adopted for solving the present problem. There are a variety of numerical methods which are suitable for solving the Navier-stokes equations. These methods have been described by Hirsch [73], and Anderson et al. [74]. In this chapter, we will focus on discretization of the pdes using the control volume approach. This approach involves integration of the pdes in the conservative form over finite volume cells and the automatic generation of conservative approximations to the pdes in algebraic form that can be solved numerically. The computational accuracy is related to several aspects such as the choice of the grid size as well as the numerical scheme. In practice, the grid size is decreased until a solution independent of the grid is achieved. Also, the choice of the numerical scheme plays an important role in dealing with false diffusion errors encountered in the solution. In general, three types of schemes have been used in the literature for solving elliptic equations, namely the power law scheme, the second order upwind scheme, and the quadratic upwind (QUICK) scheme [76, 77]. In this study, we have adopted the QUICK scheme to carry out the computations. Later in the chapter, the method of solution, boundary conditions and other related equations associated with flame stabilization are described.

3.1 Numerical Discretization

The discrete approximation of the governing equations is derived using the non-staggered mesh arrangement reported by Majumdar [78]. Figure 3.1 shows an enlarged view of the control volume employed in this study. In the non-staggered arrangement, the variables (pressure, velocity components, and all scalars) are stored at the control volume cell center. The compact form of the governing equations in the cylindrical coordinate system is given by Eq. (2.7) which is repeated here as

$$\frac{\partial}{\partial x}(\rho u \phi) + \frac{1}{r}\frac{\partial}{\partial r}(r \rho v \phi) = \frac{\partial}{\partial x}(\Gamma_{\phi}\frac{\partial \phi}{\partial x} - \rho\overline{u'\phi'}) + \frac{1}{r}\frac{\partial}{\partial r}(\Gamma_{\phi}\frac{\partial \phi}{\partial r} - \rho\overline{v'\phi'}) + S_{\phi} \qquad (3.1)$$

The source terms (S_{ϕ}) and ϕ in this equation, discussed in the previous chapter, are given in Table 2.1.

The numerical procedure employed has been discussed in some details by Patankar [1], Rhie and Chow [79], and Majumdar [78]. In this study we discuss only the important features of the numerical procedure. Equation (3.1) is integrated over the control volume, shown in Fig. 3.1, by employing the Divergence Theorem

$$\int_{V} \nabla.(\rho u \phi) dV = \int_{A} (\rho u \phi).dA \qquad (3.2)$$

The resulting algebraic equation is given in the following form

$$\begin{aligned}
&\Big[(\rho u\phi)_e A_e - (\rho u\phi)_w A_w \Big] + \frac{1}{r_P}\Big[r_n(\rho v\phi)_n A_n - r_s(\rho v\phi)_s A_s \Big] = \\
&\quad \left[\Gamma_\phi\left(\frac{\phi_E - \phi_P}{\Delta x}\right) - \rho\overline{u'\phi'} \right]_e A_e - \left[\Gamma_\phi\left(\frac{\phi_P - \phi_W}{\Delta x}\right) - \rho\overline{u'\phi'}\right]_w A_w + \\
&\quad \frac{1}{r_P}\left[\Gamma_\phi\left(\frac{\phi_N - \phi_P}{\Delta x}\right) - \rho\overline{v'\phi'}\right]_n r_n A_n - \frac{1}{r_P}\left[\Gamma_\phi\left(\frac{\phi_P - \phi_S}{\Delta x}\right) - \rho\overline{v'\phi'}\right]_s r_s A_s + S_\phi \Delta V
\end{aligned} \tag{3.3}$$

In a non-staggered arrangement for the momentum equation, not only velocities at faces (e,w,s, and n) are needed but also the pressure values at these faces. The source term S_ϕ includes the pressure gradients in x-momentum and r-momentum and is treated as follows

$$\begin{aligned}
&\int_V \frac{\partial p}{\partial x} dV = (p_e - p_w)A \\
&\int_V \frac{\partial p}{\partial r} dV = (p_n - p_s)A
\end{aligned} \tag{3.4}$$

The algebraic equation described in Eq. (3.3) is solved by interpolating the unknowns (p, u, and ϕ) in a manner that relates their values at the control volume faces to the stored values at the node point of the control volume. As stated earlier, three types of schemes can be used to perform the interpolation namely the power law, the second order upwind, and the quadratic upwind (QUICK) schemes. The details of these interpolation procedures are furnished in Refs. 76 and 77. In this study, the QUICK scheme is employed to perform the interpolation. This scheme is superior since it is second order accurate, and it minimizes the diffusion errors associated with the other models. This scheme computes the unknowns (ϕ) at the faces (w, e, n and s) in terms of

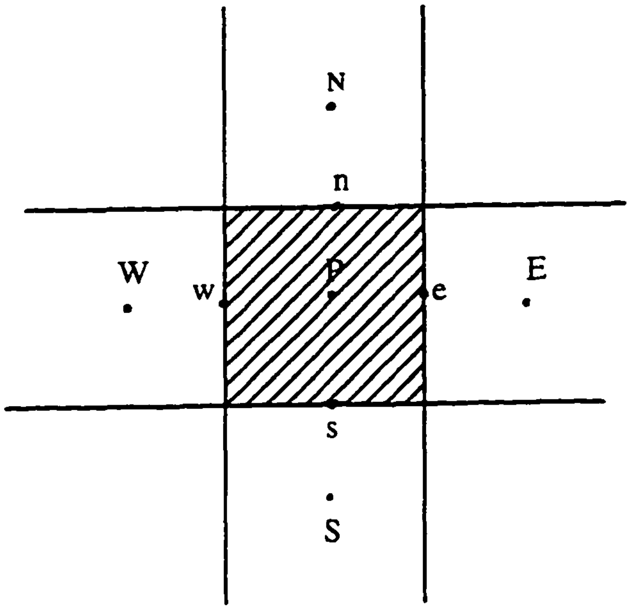

Fig. 3.1 Non-staggered control volume storage scheme.

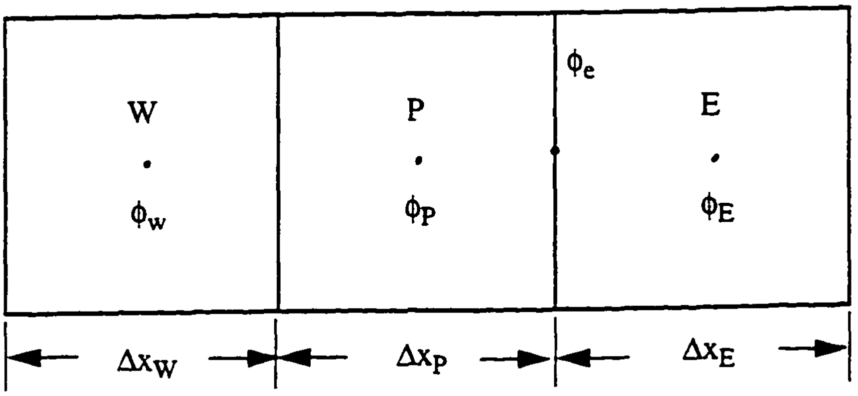

Fig. 3.2 Central, downwind, and upwind cell nomenculture emploed in the QUICK interpolation scheme.

the cell center values at (*P*, *W*, *E*, *N* and *S*). Here the QUICK scheme is illustrated for one face as depicted in Fig. 3.2; extension of the concept to all faces of a control volume is straight forward and will not be given here. The face value can be written in terms of these neighbor values as

$$\begin{aligned} \phi_e = \theta & \left[\frac{\Delta x_E}{\Delta x_P + \Delta x_E} \phi_P + \frac{\Delta x_P}{\Delta x_P + \Delta x_E} \phi_E \right] + \\ (1 - \theta) & \left[\frac{\Delta x_W + 2 \Delta x_P}{\Delta x_W + \Delta x_P} \phi_P - \frac{\Delta x_P}{\Delta x_W + \Delta x_P} \phi_W \right] \end{aligned} \tag{3.5}$$

The choice of θ determines the scheme type. For example a value of $\theta = 0$ would produce a second-order upwind scheme while $\theta = 3/4$ would result in a QUICK scheme. One of the drawbacks of the scheme given in Eq. (3.5) is that of numerical instability (over shooting and under shooting). It can occur unless the interpolation is appropriately bounded. In this case θ is computed as follows:

$$\begin{aligned} \theta &= \frac{2 - 3\bar{\phi}_P}{1 - 2\bar{\phi}_P} && \textit{for} \quad \frac{5}{6} < \bar{\phi}_P < 1 \\ &= \frac{-3\bar{\phi}_P}{1 - 2\bar{\phi}_P} && \textit{for} \quad -\frac{1}{2} < \bar{\phi}_P < 0 \\ &= \frac{3}{4} && \textit{otherwise} \end{aligned} \tag{3.6}$$

where

$$\bar{\phi}_P = \frac{\theta_P - \theta_W}{\theta_E - \theta_W}$$

From Eq. (3.5) one can eliminate the face values in Eq. (3.3), and the resulting algebraic equation would contain only cell centered values of different variables. Any variable ϕ at a point P may be written as

$$A_P \phi_P = A_E \phi_E + A_W \phi_W + A_N \phi_N + A_S \phi_S + S_\phi \tag{3.7}$$

where A_P, A_E, A_W, A_N and A_S are coefficients that involve the flow properties of convection, diffusion and area. Solution of the Eq. (3.7) requires specific treatment for the pressure and velocity components in the mass and momentum equations. This can be achieved by implementing the SIMPLE algorithm [1].

Velocity and Pressure Calculation

One of the problems associated in solving Eq. (3.7) relates to finding the pressure field such that when it is substituted in the momentum equations, the resulting velocity components obtained from solution of these equations would also satisfy the mass conservation equation. In general the pressure field is initially guessed and subsequently corrected. In SIMPLE algorithm, the pressure correction can be achieved by combining the momentum equations with the continuity equation. Using Eq. (3.7), one obtains the axial and radial momentum equations in the following form

$$\begin{aligned} A_P u_P &= \sum_{NB} A_{NB} u_{NB} + (p_w - p_e) A + S_u \\ A_P v_P &= \sum_{NB} A_{NB} v_{NB} + (p_n - p_s) A + S_v \end{aligned} \tag{3.8}$$

where subscript NB denotes (W, E, N and S) . The SIMPLE algorithm starts with a guessed values of u^*, v^* and p^* such that

$$\begin{aligned} p &= p* + p' \\ u &= u* + u' \\ v &= v* + v' \end{aligned} \tag{3.9}$$

where p', u' and v' are the pressure and velocities correction. The guessed velocities values satisfy Eq. (3.8) as

$$\begin{aligned} A_P u*_P &= \sum_{NB} A_{NB} u*_{NB} + (p*_w - p*_e)A + S_u \\ A_P v*_P &= \sum_{NB} A_{NB} v*_{NB} + (p*_n - p*_s)A + S_v \end{aligned} \tag{3.10}$$

Subtracting Eq. (3.10) from Eq. (3.8) results in momentum balance equations in terms of the velocity and pressure corrections as

$$\begin{aligned} A_P u'_P &= \sum_{NB} A_{NB} u'_{NB} + (p'_w - p'_e)A \\ A_P v'_P &= \sum_{NB} A_{NB} v'_{NB} + (p'_n - p'_s)A \end{aligned} \tag{3.11}$$

The summation terms $A_{NB}\ u'_{NB}$ and $A_{NB}\ v'_{NB}$ are dropped from Eq. (3.11) (since corrections at neighboring points will be zero at convergence), and the velocity correction can be expressed in terms of pressure correction as follows:

$$\begin{aligned} u'_P &= \frac{1}{A_P}(p'_w - p'_e)A \\ v'_P &= \frac{1}{A_P}(p'_n - p'_s)A \end{aligned} \tag{3.12}$$

The continuity equation can be expressed as

$$(\rho uA)_e - (\rho uA)_w + (\rho vA)_n - (\rho vA)_s = 0 \tag{3.13}$$

Combining Eqs. (3.9), (3.12) and (3.13), the pressure correction equation can be written as

$$\begin{aligned}\left(\rho u^* A\right)_e^w + \left(\rho v^* A\right)_n^s + (\rho A)_e \frac{1}{(A_P)_e}(p_P' - p_E') - (\rho A)_w \frac{1}{(A_P)_w}(p_W' - p_P') +\\ (\rho A)_n \frac{1}{(A_P)_n}(p_P' - p_N') - (\rho A)_s \frac{1}{(A_P)_s}(p_S' - p_P') = 0\end{aligned} \tag{3.14}$$

Equation (3.14) is solved for the pressure correction field which in turn is used to compute the velocity corrections from Eq. (3.12). The velocity components and the pressure are then updated using Eq. (3.9).

3.2 General Solution Procedure

In the present study a general purpose CFD code, known as "FLUENT" was used to obtain the reacting flow calculations. The FLUENT code [80] uses an iterative solution procedure with iterations continuing until all equations are satisfied at all points in the flow field. Each iteration of the solution procedure consists of the solution of the momentum equations based on the guessed values of pressure namely p*. The following step uses Eq. (3.14) to calculate the pressure field correction. The velocity components are then updated by solving Eq. (3.9). The turbulence equations such as the Reynolds stress transport equations, and ϵ-equation are solved using the updated velocity field. In the same manner the enthalpy and species conservation equations are solved using the previously updated values of other variables. Finally the fluid properties are updated.

These steps are repeated until convergence is achieved when residuals for all properties are of the order of 10^{-5} or less.

Calculations for both reacting and non-reacting flows were performed utilizing the k-ϵ model and the RSM model. Figure 3.3 shows the calculation procedure for the RSM. It should be noted that the RSM model could not be executed directly without first implementing the k-ϵ model due to divergence of the calculation procedure. Typically, for a given fuel jet velocity, first non-reacting case is simulated by employing the k-ϵ model. Two approaches can be used successfully to obtain the reacting flow solution with the RSM. In the first approach, with the combustion model activated, the reacting flow results are obtained with the RSM by using the non-reacting case obtained from the k-ϵ model as the starting solution. Alternatively, a direct reacting flow solution can be used from the k-ϵ model as the starting point to compute the reacting flow solution with the RSM.

3.3 Boundary Conditions

Only the upper half of the flow domain is computed due to symmetry about the centerline of the cylindrical tube (Fig. 2.1). Along the center line, the diffusion fluxes have zero value. Thus, the normal gradients of all variables including velocities are assigned zero value. The constant pressure condition is applied along the outer boundaries in order to ensure a free boundary condition. A no-slip condition is used on the solid tube surfaces. For the fuel jet, a velocity profile, obtained from a separate calculation of the flow field inside the pipe is applied at the tube exit section. The turbulence inlet values of k and ϵ are calculated from a specified inlet turbulence intensity as follows

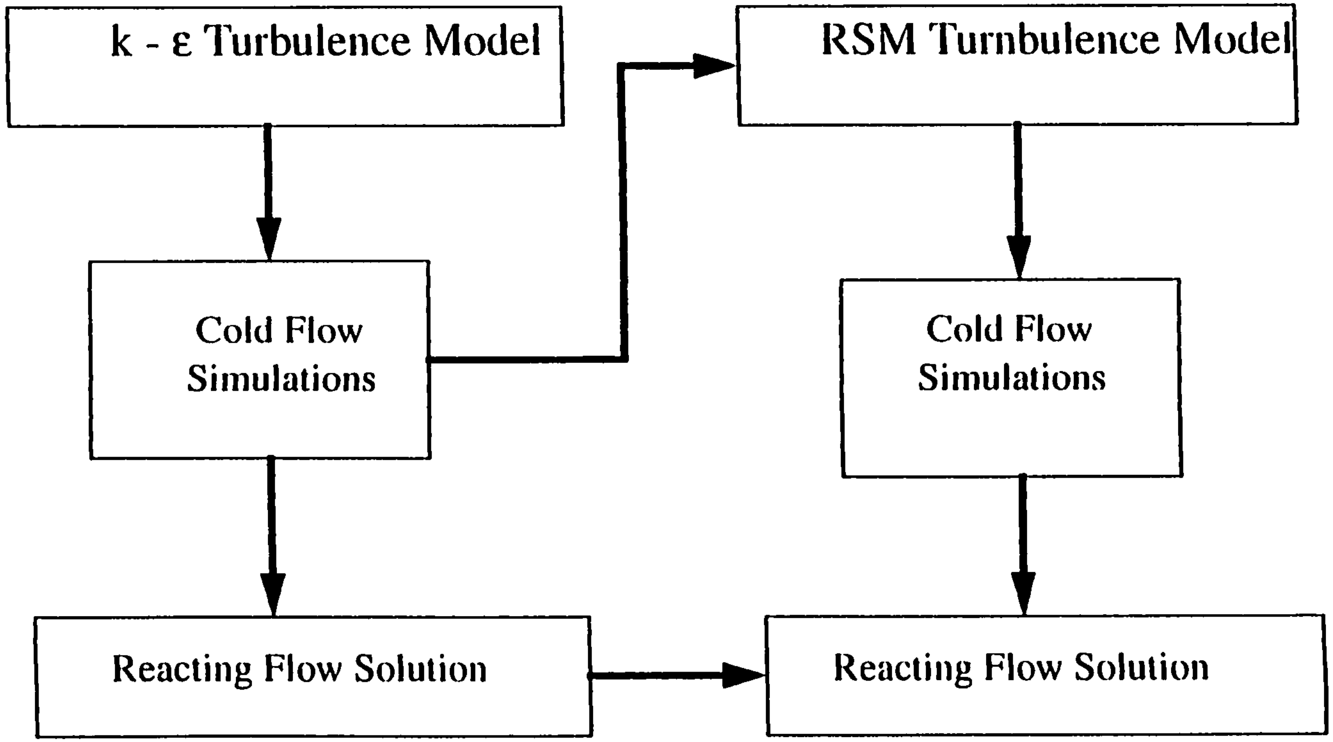

Fig. 3.3 Flow chart of the overall calculation procedure.

$$k = \frac{3}{2}(u_{inlet} I)^2$$
$$\epsilon = C_{\mu}^{\frac{3}{2}} \frac{k^{\frac{3}{2}}}{l} \qquad (3.15)$$

The value of C is 0.09, and l is the mixing length. It is defined as ($0.07\ L$) where L is the characteristic length which is the same as the radius of the pipe. The solution obtained from the k-ϵ model serves as a guessed solution for the RSM model. At the boundaries, input for the Reynolds stresses are identical to those required for the k-ϵ model. The inlet stresses in terms of k are given as

$$\overline{u^{\prime} u^{\prime}} = 2\overline{v^{\prime} v^{\prime}} = k$$
$$\overline{u^{\prime} v^{\prime}} = \overline{v^{\prime} u^{\prime}} = 0 \qquad (3.16)$$

For the dissipation rate equation, the inlet value of ϵ is derived from the Eq. (3.15).

3.4 Flame Stabilization Concept

The concept of predicting the stabilization region in diffusion flames has been studied by many experimental and theoretical researchers. The classical approach, due to Vanquickenborne and van Tiggelen [3], assumes that a premixed fuel-air mixture occurs at the flame base. The premixed theory is also supported by Eickhoff et al. [81], who show that more than half of the fuel is burned around the region of flame stabilization. Other studies like the one by Peters [9], Janicka and Peters [10], and Peters and Williams [11] have predicted the lift-off height according to the laminar flamelet concept. The following sections illustrate additional modeling considerations required for locating the flame base.

Turbulent Flame Velocity

As noted earlier, the studies by Vanquickenborne and van Tigglen [3] and Kalaghatgi [7] have shown that the base of flame stabilizes on the stoichiometric surface at the height where the local axial velocity equals the turbulent flame velocity. In order to evaluate this hypothesis numerically, we relate the ratio of turbulent burning velocity to the laminar burning velocity based on a correlation by Kalaghatgi [7]

$$\frac{S_t^2}{S_l^2} = R_l \, . \, K \, . \, f_4 \tag{3.17}$$

where K and f_4 are correlation constants (K ranges from 0.56 to 1.3, but average value of $K=0.93$ has been used, and f_4 is 0.138 for methane and 0.123 for propane). The term R_l is the turbulence Reynolds number, given by

$$R_l = \frac{u' \, l}{\nu} \quad , \qquad u' = \sqrt{\frac{2}{3}k} \tag{3.18}$$

where u' is the root mean square (rms) fluctuation velocity, l is turbulent length scale in the jet mixing layer ($l = 0.07\,x$), x is the axial height, and ν is the kinematic viscosity. The term S_l in Eq. (3.17) is the laminar flame velocity. The expression of S_t is used in the numerical analysis to locate the base of the flame.

Critical Rate of Scalar Dissipation

The alternative approach for locating the base of flame stabilization has been investigated by Peters and Williams [11], Sanders et al. [12], and Bray and Peters [82].

In these studies the flame base is assumed to be located along the stoichiometric line. The base is located at an axial distance along stoichiometric line where the scalar dissipation rate (χ) reaches a critical value (χ_{crt}). The dissipation rate is given as [82]

$$\chi = C_d \frac{\epsilon}{k} g \tag{3.19}$$

where the constant C_d is an empirical and is usually taken as 2.0, and g is the mixture fraction variance. An approximate expression for critical value of the dissipation rate is given as [82]

$$\chi_{crt} = 4 a f_{st}^2 [erfc^{-1}(12 f_{st})]^2 \tag{3.20}$$

where a is the strain rate value at extinction (for methane a ranges from 360 - 420) and $erfc^{-1}$ denotes the inverse of the complementary error function. The parameter f_{st} is the stoichiometric mixture fraction (for methane $f_{st} = 0.055$).

Burnout Rate

A study by Eickhoff et al. [81] has shown that the flame stabilization region can be identified from the axial distribution of the rate of burnout $b(x)$. At a given axial location, $b(x)$ is determined from unburned and partially burned mass fractions c_i by the following relation

$$b(x) = 1 - \left[2\pi \int_0^{\infty} \rho u \sum c_i . h_i r dr \,/\, \dot{M}_0 . h_0 \right] \tag{3.21}$$

where h_i is the enthalpy of species i, h_0 is the inlet enthalpy of formation of the fuel, and M_0 denotes the inlet mass flow rate. It has been shown in Ref. 81, that the value of $b(x)$

obtained from the above equation increases steeply immediately after the flame stabilization region. In this study the value of b(x) is numerically integrated along the radial direction to identify region of flame stabilization.

Chapter 4

RESULTS FOR METHANE INJECTOR

The theoretical formulations and the computational procedure described in Chaps. 2 and 3 are applied to obtain the results for non-premixed subsonic flows. In this chapter results are presented for both reacting and non-reacting flows utilizing the k-ϵ model and the RSM. First, the numerical results for the non-reacting flow are compared with different experimental and numerical studies reported in the literature. These comparisons are part of the validation of the turbulence model namely RSM adopted in this study. The reacting flow results, obtained from the eddy dissipation model in conjunction with the RSM, are also compared with experimental studies by Comer et al. [8], and others. The hypothesis for stabilization of the flame in the premixing region has also been demonstrated from the present numerical results. Results were initially obtained with several grids to establish grid independence of the results.

4.1 Grid Independence of Numerical Results

Studies were conducted to investigate the effect of grid size on the numerical results. Three grids, namely 70x41, 155x61 and 140x81 were used. Figure 4.1 shows a typical non-uniform grid pattern, with more grid points being placed between the injection point and the flame base in order to capture the sharp gradients in properties near the flame base. The influence of grid size has been investigated for reacting flow case, with RSM turbulence model, and two step kinetics model. Figures 4.2 and 4.3 show the

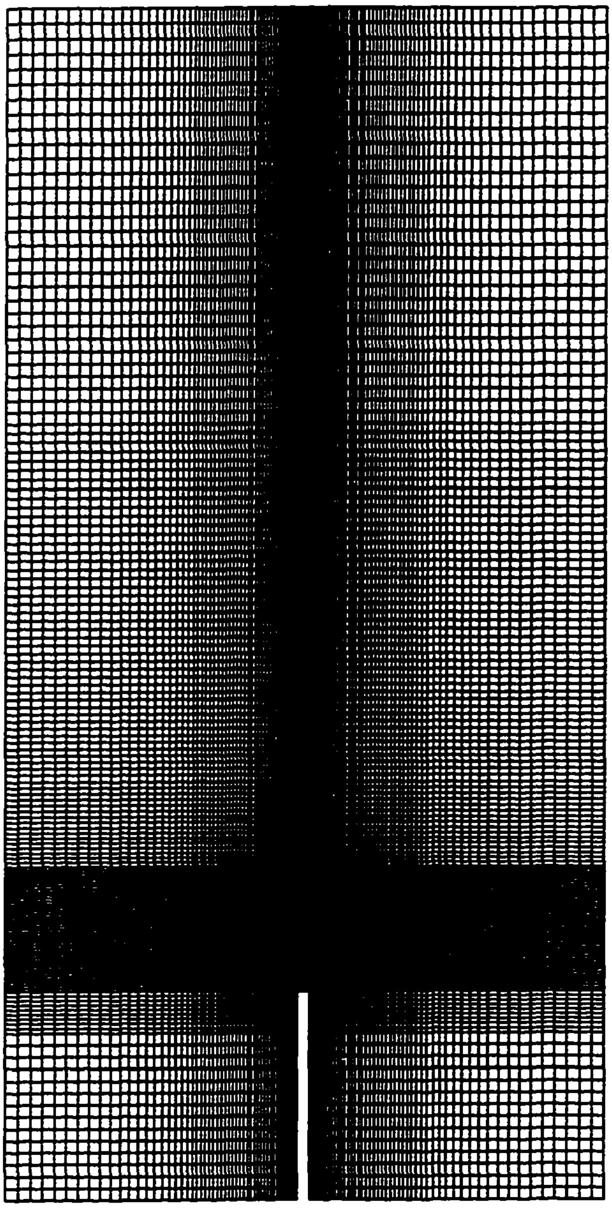

Fig. 4.1 Typical non-uniform grid pattern.

influence of grid size on the axial temperature distribution for jet velocities of 34.7 m/s and 62.5 m/s, respectively. It can be seen that the results generated from 155x61 and 140x81 grid points match each other. However, the results from 70x41 grid compare unfavorably with the other two grids. The effect of grid on the mixture fraction (*f*) is given in Fig. 4.4. It is noted that the mixture fraction accounts for both the fuel and oxidizer mass fractions and is defined in Eq. (2.19). Figure 4.5 shows the radial temperature profile for the jet exit velocity of 34.7 m/s at an axial location of 5.01 cm from the injection point. The influence of grid on the radial variation of temperature is also shown in Fig. 4.6 for the 62.5 m/s jet velocity case. From these figures it is evident that the choice of a grid size of 155x61 would be satisfactory for this study. Table 4.1 shows the effect of grid size on the global flame parameter such as the base flame height. The coarser grid size predicts slightly higher base height as compared to the other two grid sizes.

4.2 Predictions for Turbulent Non-Reacting Jet

The purpose of this section is to obtain results from the RSM for constant density as well as variable density flows. The first case considers an air jet issuing vertically in quiescent air which has been studied experimentally by Wygnanski and Fiedler [83] and numerically by Donaldson [84]. The second case considers the same geometry but methane issues in ambient air. In this case the density variations occur due to mixing of methane with the surrounding air. The results are compared with experimental data of Eickhoff et al. [81] and Horch [85].

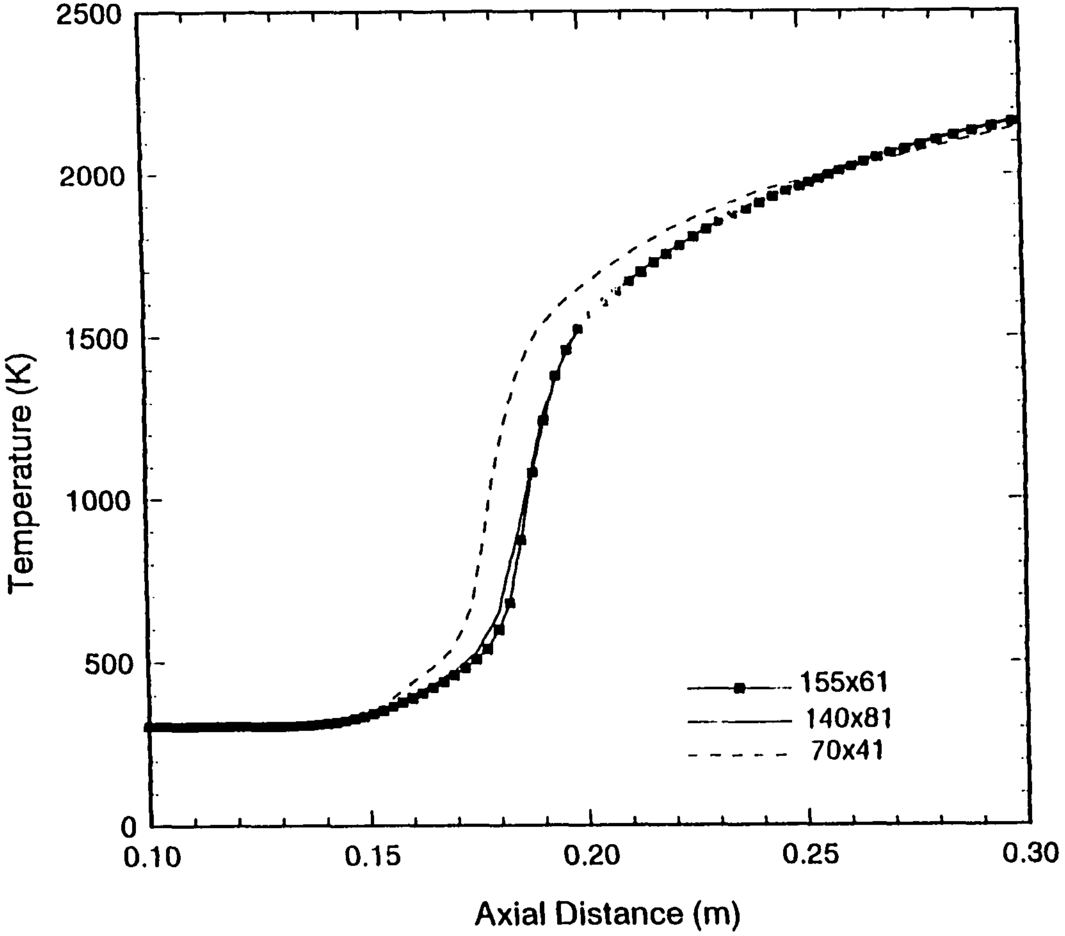

Fig. 4.2 Effect of grid size on axial temperature distribution for jet velocity of 34.7 m/s.

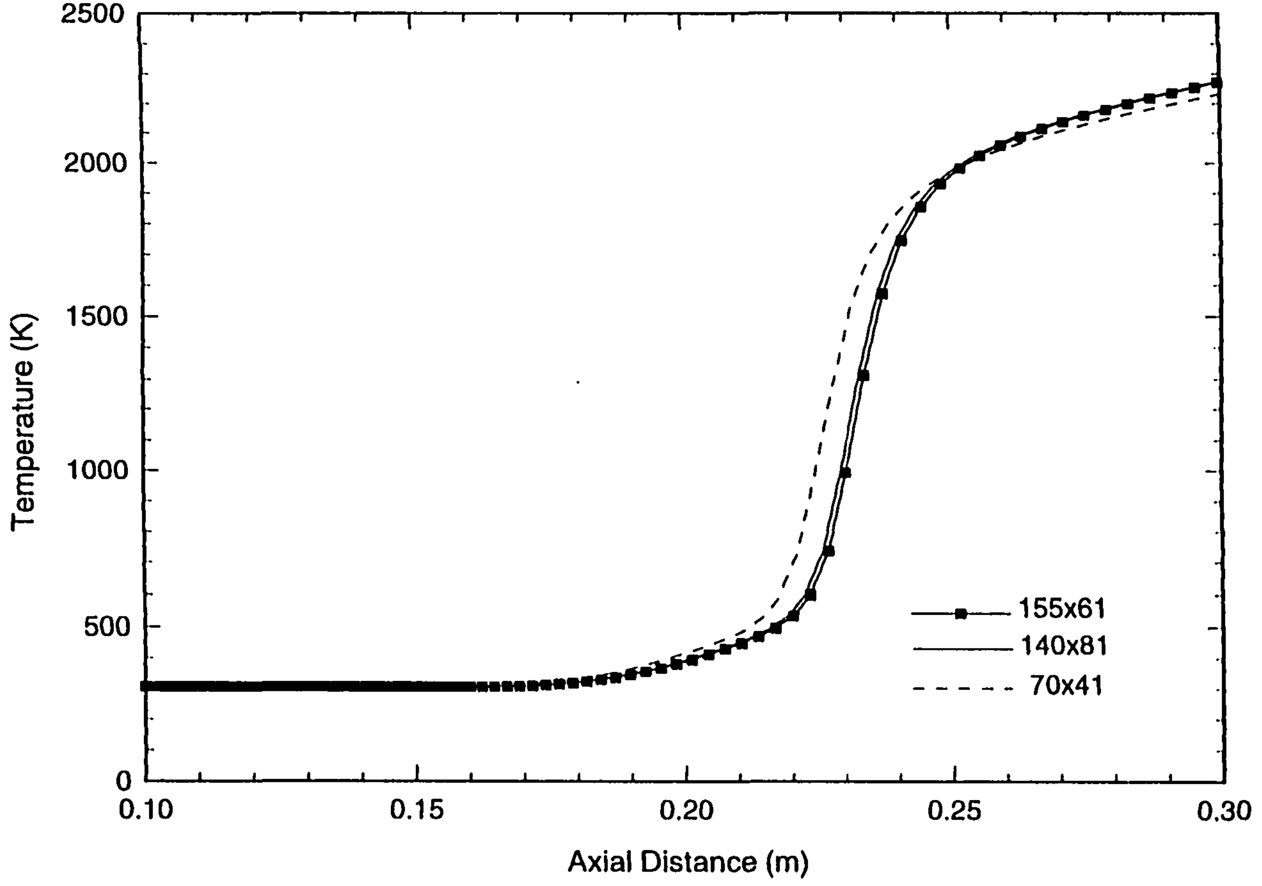

Fig 4.3 Effect of grid size on axial temperature distribution for axial jet veloty of 62.5 m/s.

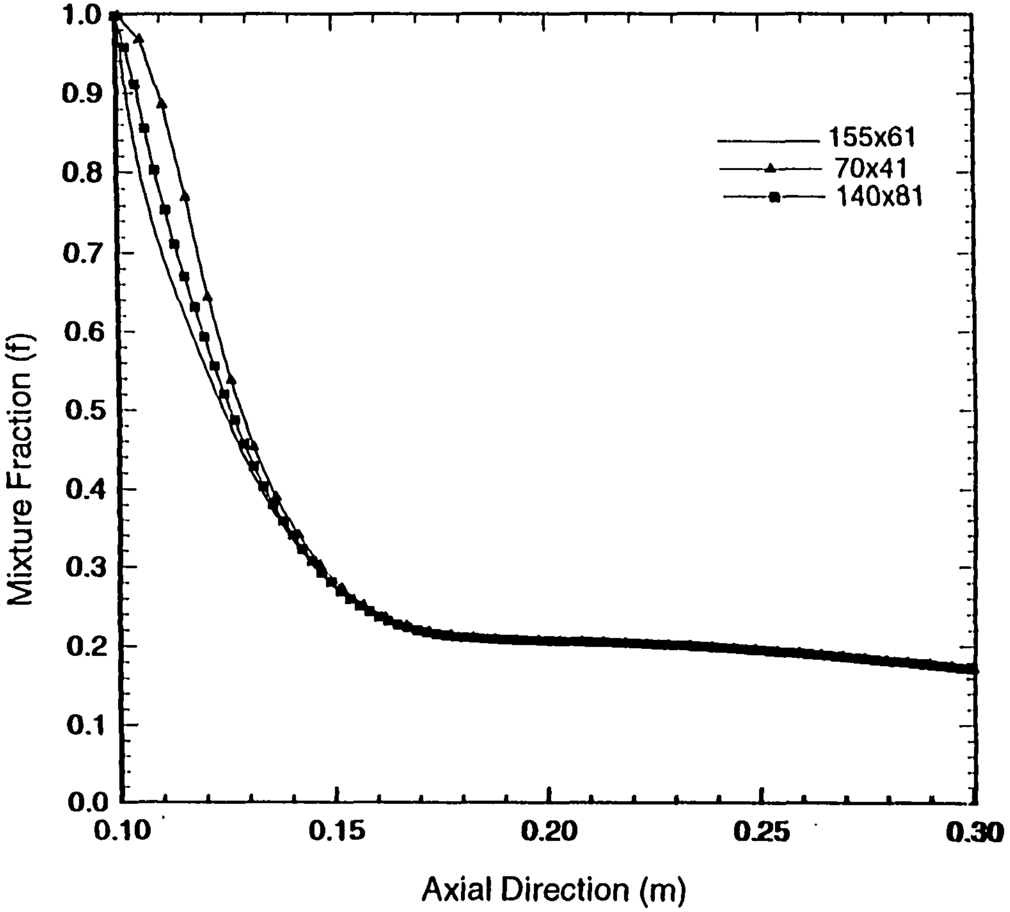

Fig. 4.4 Effect of grid size on prediction of the mixture fraction (f).

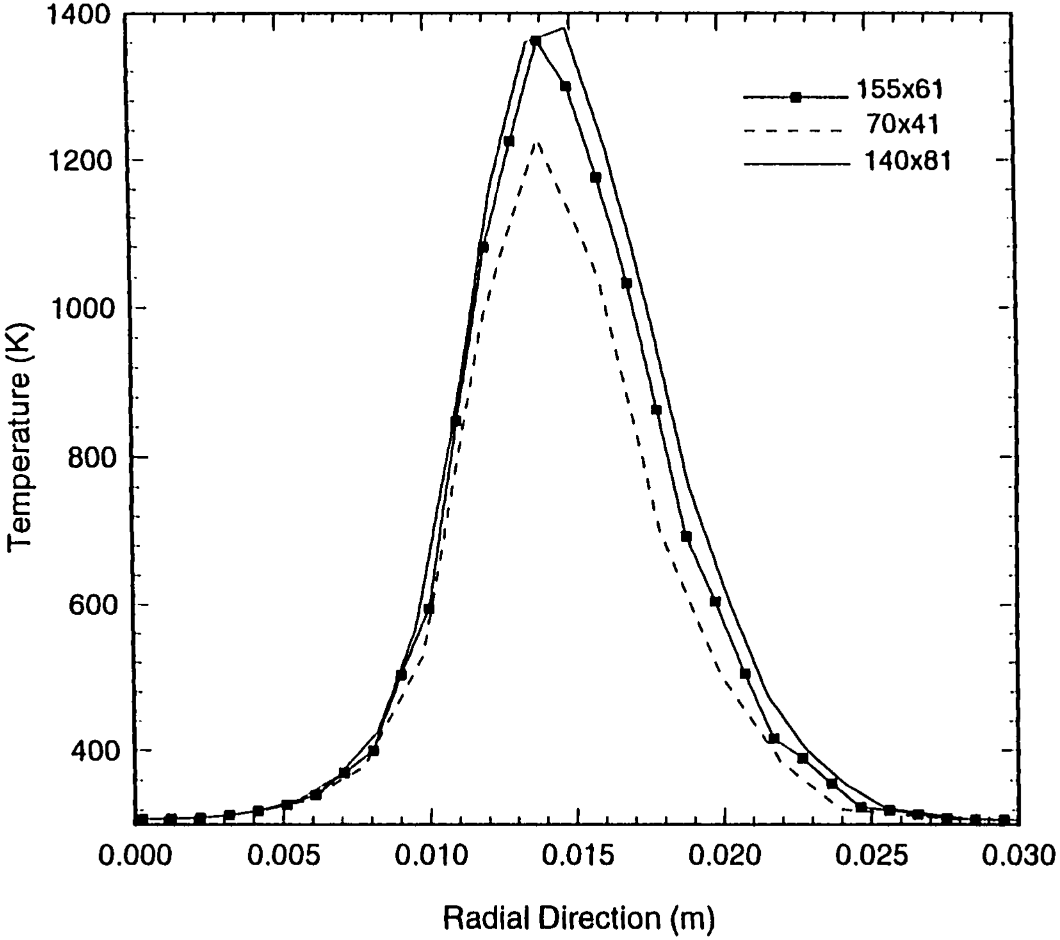

Fig. 4.5 Comparison of the radial temperature profile for three different grid sizes axial location of 5.01 cm and exit jet velocity of 34.7 m/s.

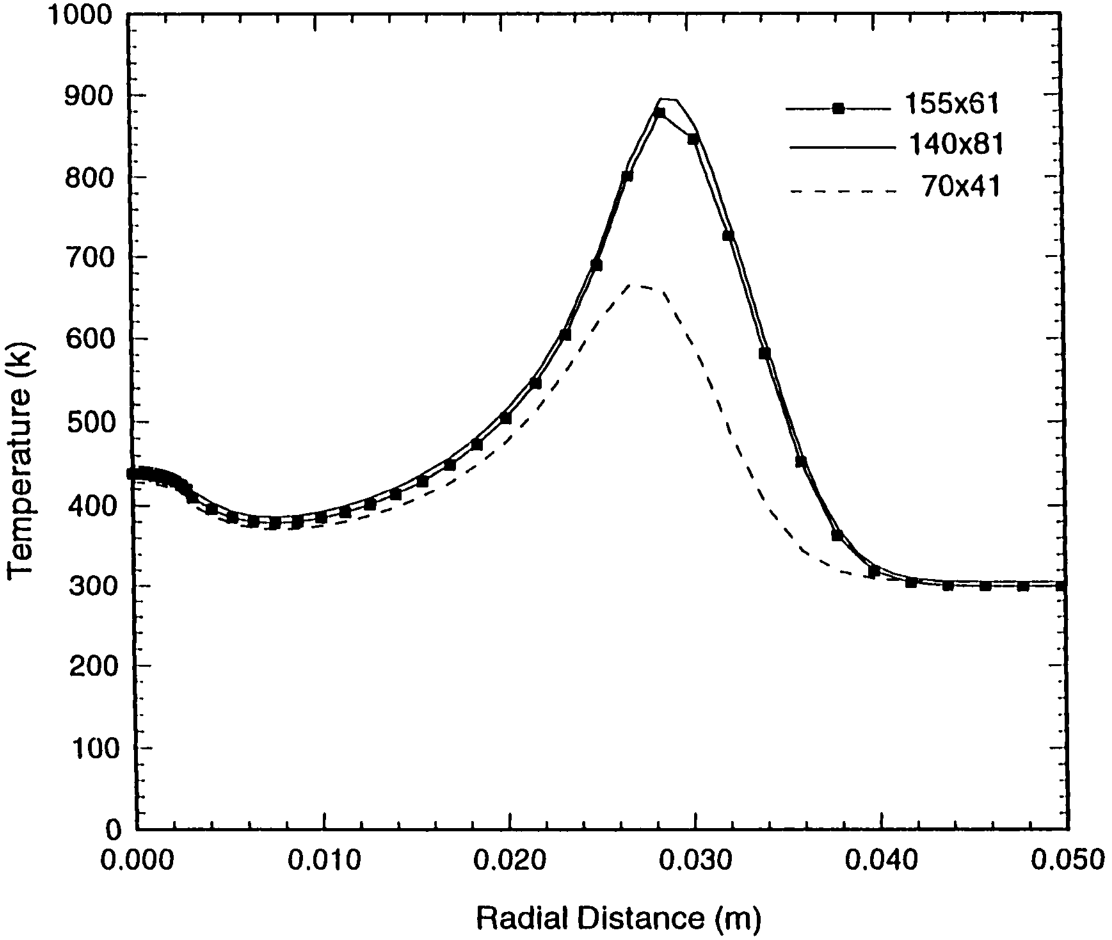

Fig. 4.6 Comparison of radial temperature profile for three different grid sizes at axial location of 10.2 cm from the injection for exit jet velocity of 62.5 m/s.

Table 4.1 Effect of grid size on flame base height. (height in cm)

Grid	height (jet velocity 34.7 m/s)	height (jet velocity 62.5 m/s)
70x41	5.01	11.22
155x61	4.86	10.90
140x81	4.88	11.04

The computations of the air jet are compared with measurements in Figs. 4.7 and 4.8. One can observe that the radial profile of the normal stress $(\overline{u' u'})$ and shear stress $(\overline{u' v'})$ compare favorably with experimental results of Wygnanski and Fiedler [83] and numerical results of Donaldson [84]. These profiles were taken at an axial location of 37 cm. The variable density case involving mixing of non-reacting methane jet in air is depicted in Figs. 4.9 - 4.11. In Figs. 4.9 and 4.10, the computed axial profile of the normal stress for jet exit velocities of 50 m/s and 70 m/s are compared with respective experimental results of Eickhoff et al. [81]. The agreement between the measured and calculations is good in a wide range of the flow domain except at a location near $x/d = 18$ (Fig. 4.9) and $x = 20$ (Fig. 4.10), where a deviation of about *12%* occurs. We note that the present model predicts higher peak values for $(\overline{u' u'})$ and $(\overline{u' v'})$ as compared to experimental results. This deviation may be due to model deficiencies as well as due to experimental uncertainties. Figure 4.11 shows the radial position where the mean mixture fraction (f) equals the stoichiometric value as a function of axial distance for the 70 m/s fuel jet velocity case. The present numerical results for the inert flow case are compared with numerical results of Sanders and Lamers [12] and experimental results of Horch [85]. It is observed that the present numerical results compare very well with experimental results for the entire range of x/d. In contrast the numerical results of Sanders and Lamers [12] predict experimental results very well at low values of x/d but deviate significantly at higher values of x/d.

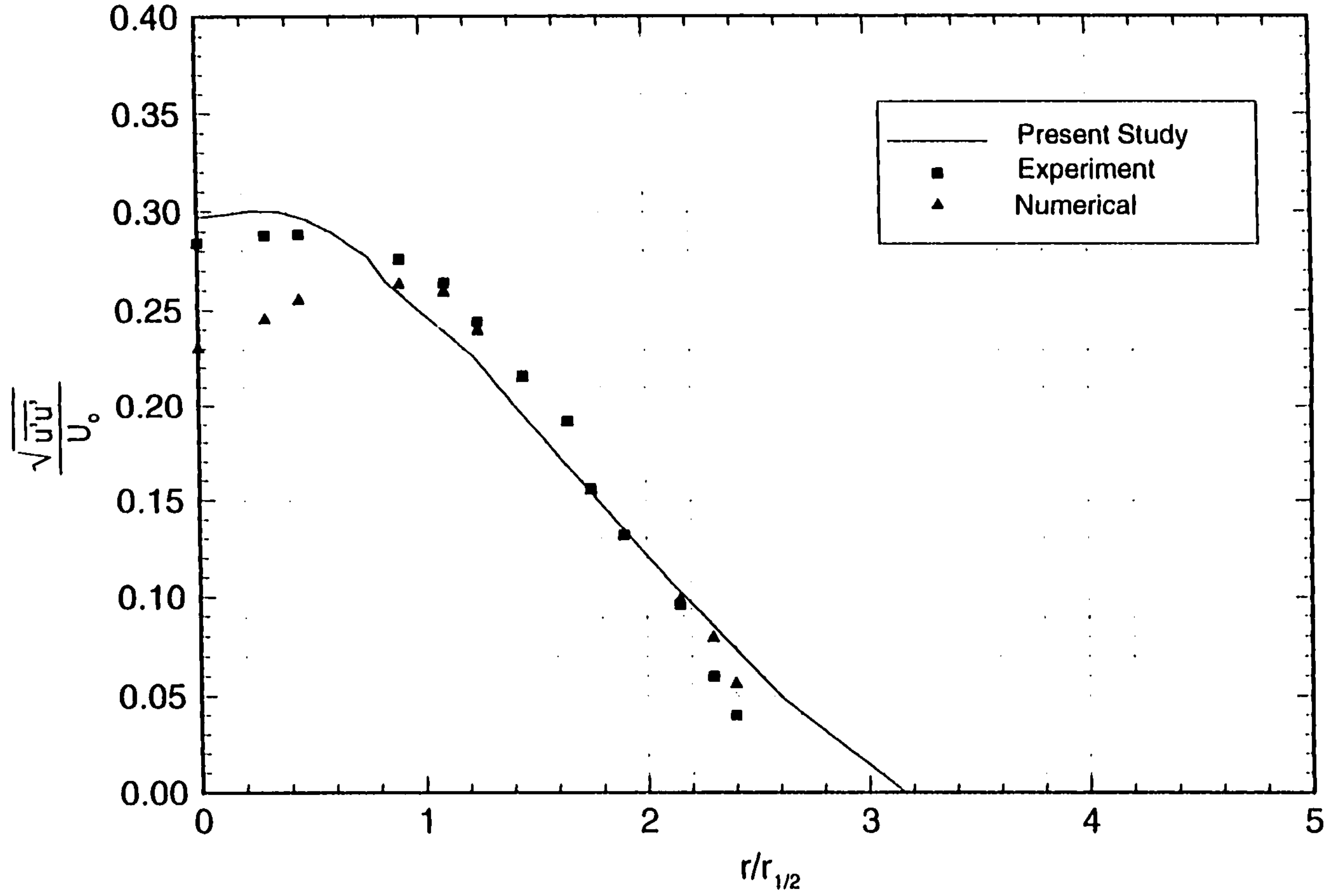

Fig. 4.7 Prediction of u'u' stress at axial location of 37 cm and comparison with experimental results from Wygnanski & Fiedler.

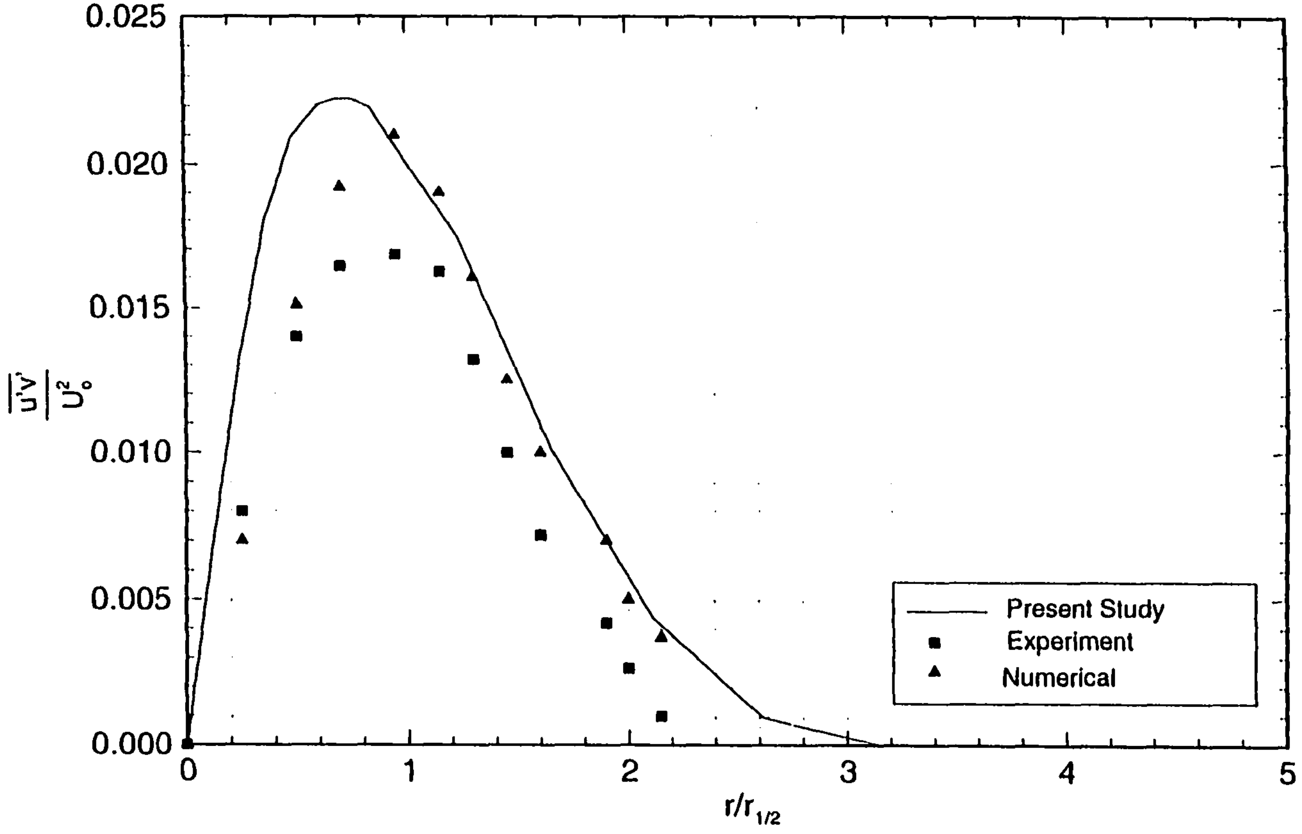

Fig. 4.8 Prediction of $\overline{u'v'}$ stress at axial location of 37 cm and comperison with experimental results from Wynanski & Fiedler.

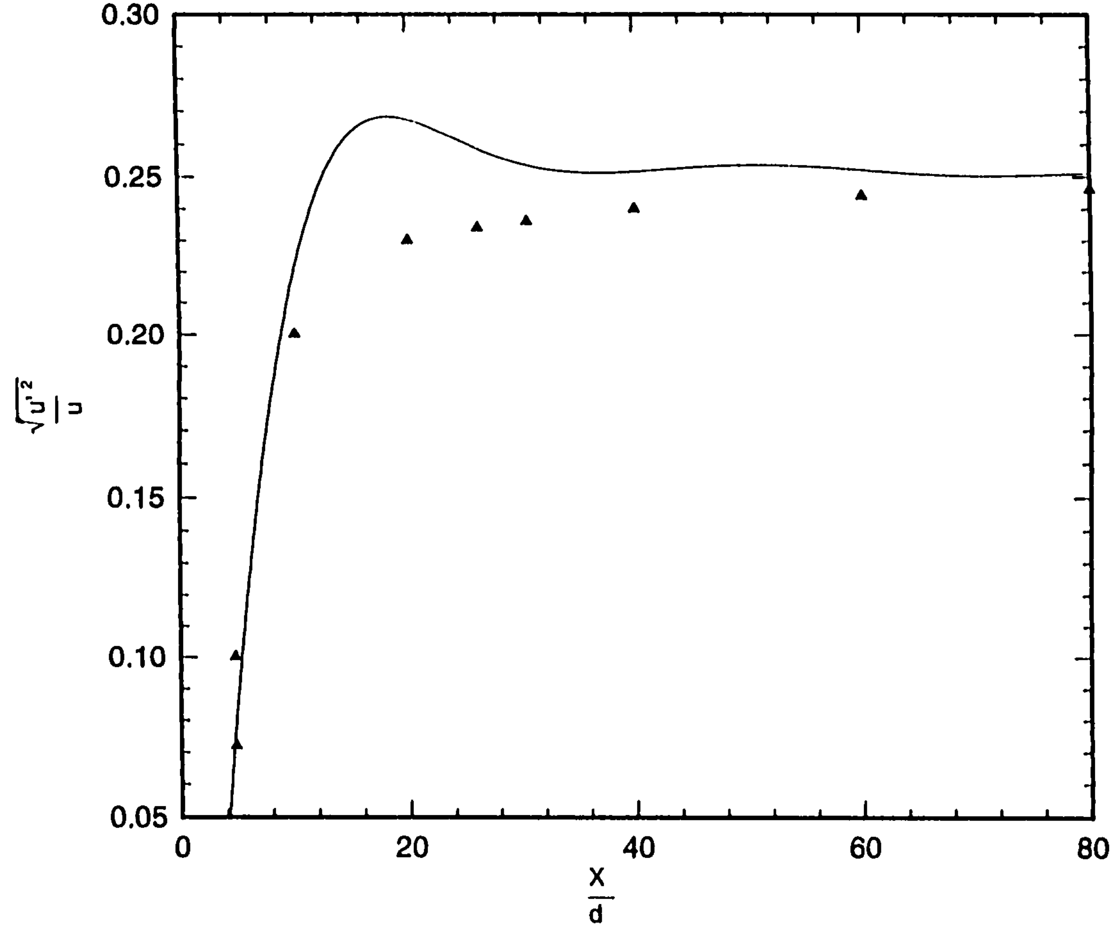

Fig 4.9 Comparison of predicted turbulent intensity (solid line) with experimental results (symbols) for isothermal jet of exit velocity 50 m/s.

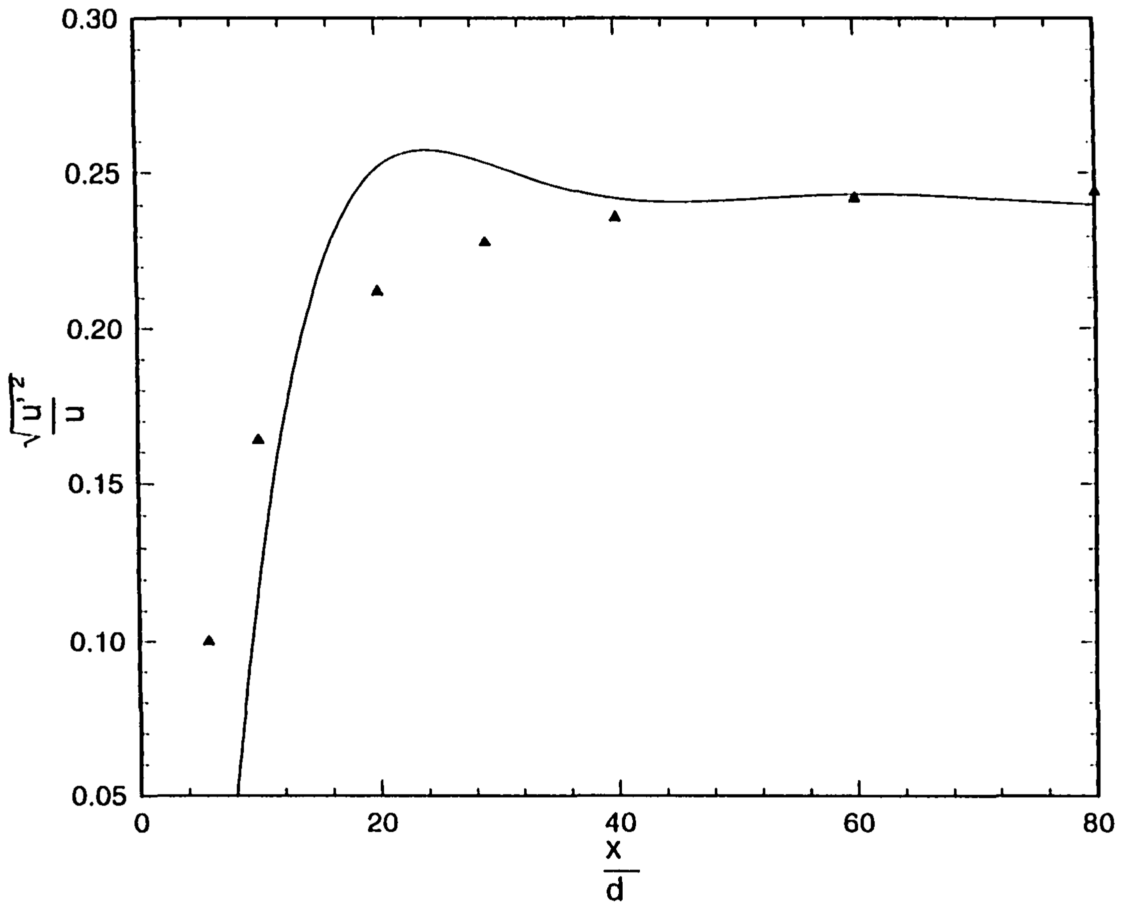

Fig. 4.10 Comparison of predicted turbulent intensity (solid line) with experimental results (symbols) for non-reacting flow. Jext exit velocity 70 m/s.

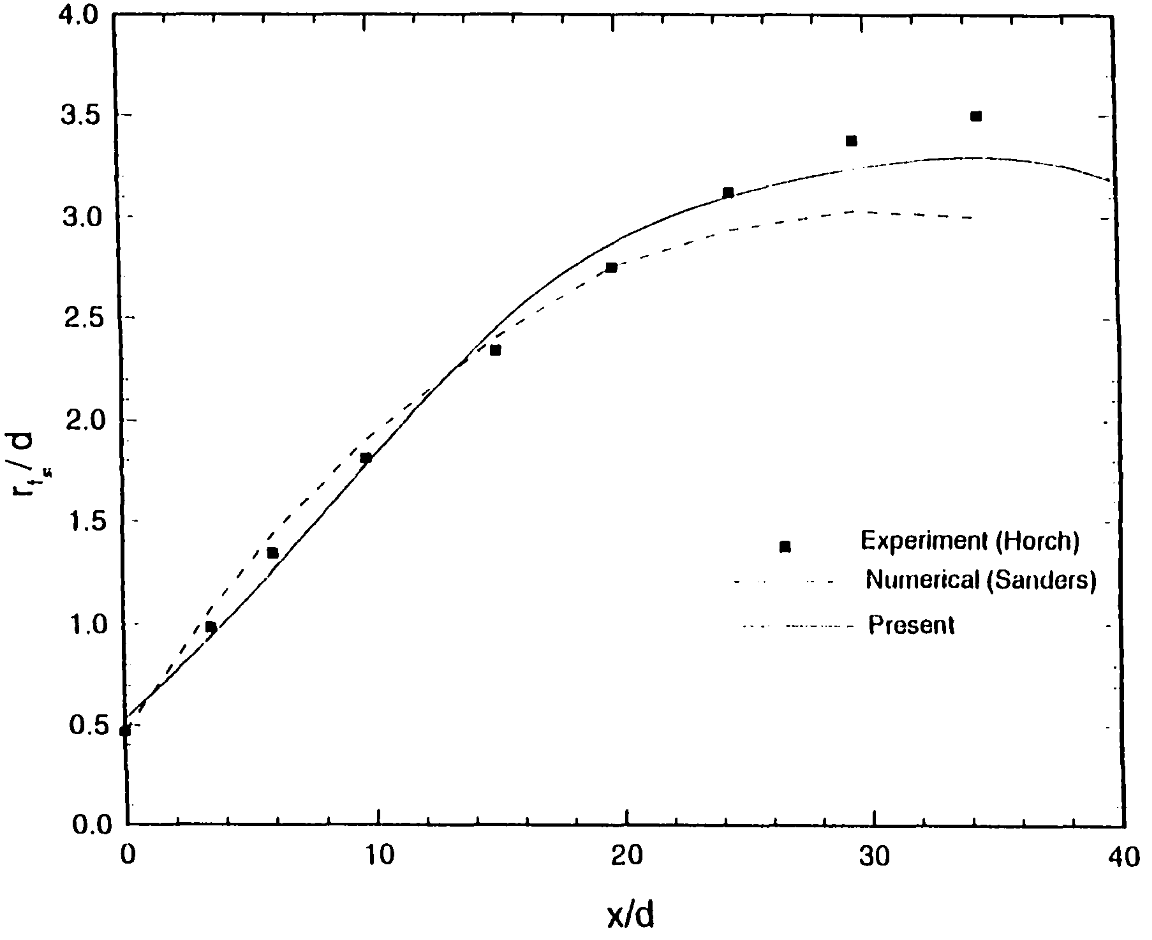

Fig. 4.11 Radial position where the mean mixture fraction equals to the Stoichiometric value as a function of axial distance.

4.3 Reacting Flows Results

The numerical results presented in this section were obtained by using two distinctive turbulence models namely, the k-ϵ and the RSM models. The combustion model, as discussed earlier, uses a two-step chemical kinetics model, and the eddy dissipation model to determine the process limiting reaction rate. Results obtained from the present numerical procedure were compared with experimental results reported by Comer et al. [8]. In their study the flame base height was measured experimentally for various fuel-jet velocities. For numerical solutions, the tube diameter, tube length and tube thickness were chosen identical to those used by Comer et al. [8] and these values are described in Chap. 2.

Figure 4.12 shows the flame predicted from the (k-ϵ) model at an axial jet velocity of 34.7 m/s. The predicted flame base height of 1.3 cm compares very unfavorably with the experimentally observed value of 5.9 cm as reported by Comer et al. [8]. The reasons for this deviation will be discussed later in this chapter. Figure 4.13 shows the flame structure computed using the RSM. The flame base height of 5.1 cm compares favorably with the observed value of 5.9 cm. Figures 4.14 and 4.15 show the comparison of the numerically obtained flame shape with the Schlieren photographs (Comer et al. [8]) of the flame for the jet velocities of 34.7 m/s and 62.5 m/s. Both the numerical and experimental results show a premixed region prior to establishment of the flame base at a distance downstream of the injection point. The flame shape, flame base width and maximum flame width obtained from computations compared favorably with experimental results. For the jet velocity of 62.5 m/s (Fig. 4.15), the widening of flame base, and increase in

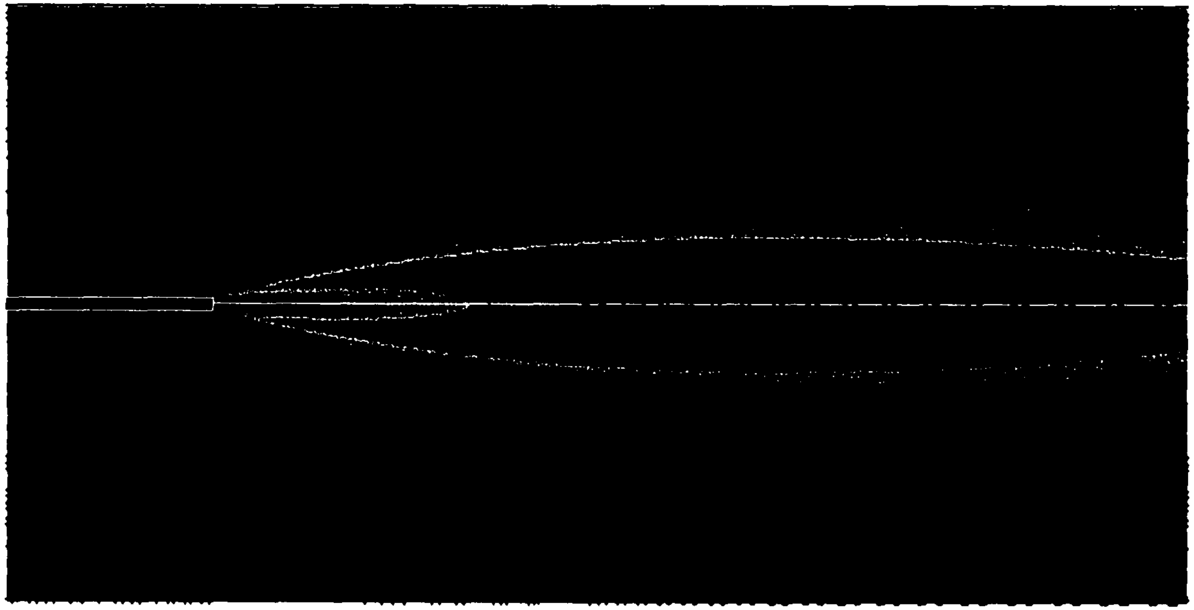

Fig. 4.12 Lifted flame structure predicted by the k-ϵ model for a fuel jet exit velocity of 34.7 m/s.

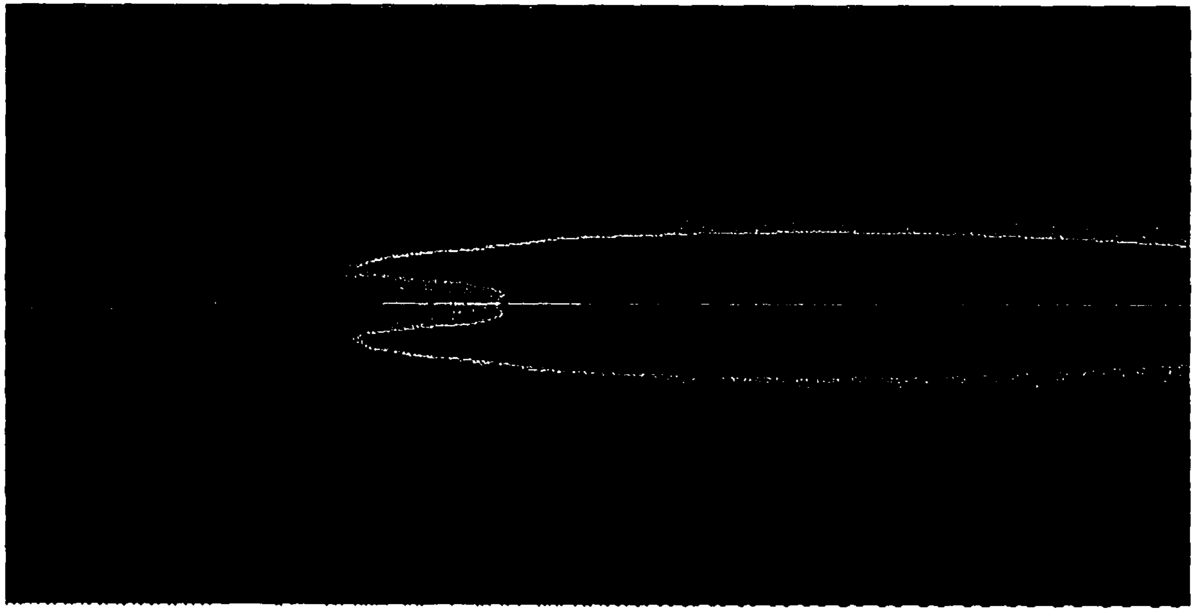

Fig. 4.13 Lifted flame structure predicted by the (RSM) model for a fuel jet exit velocity of 34.7 m/s.

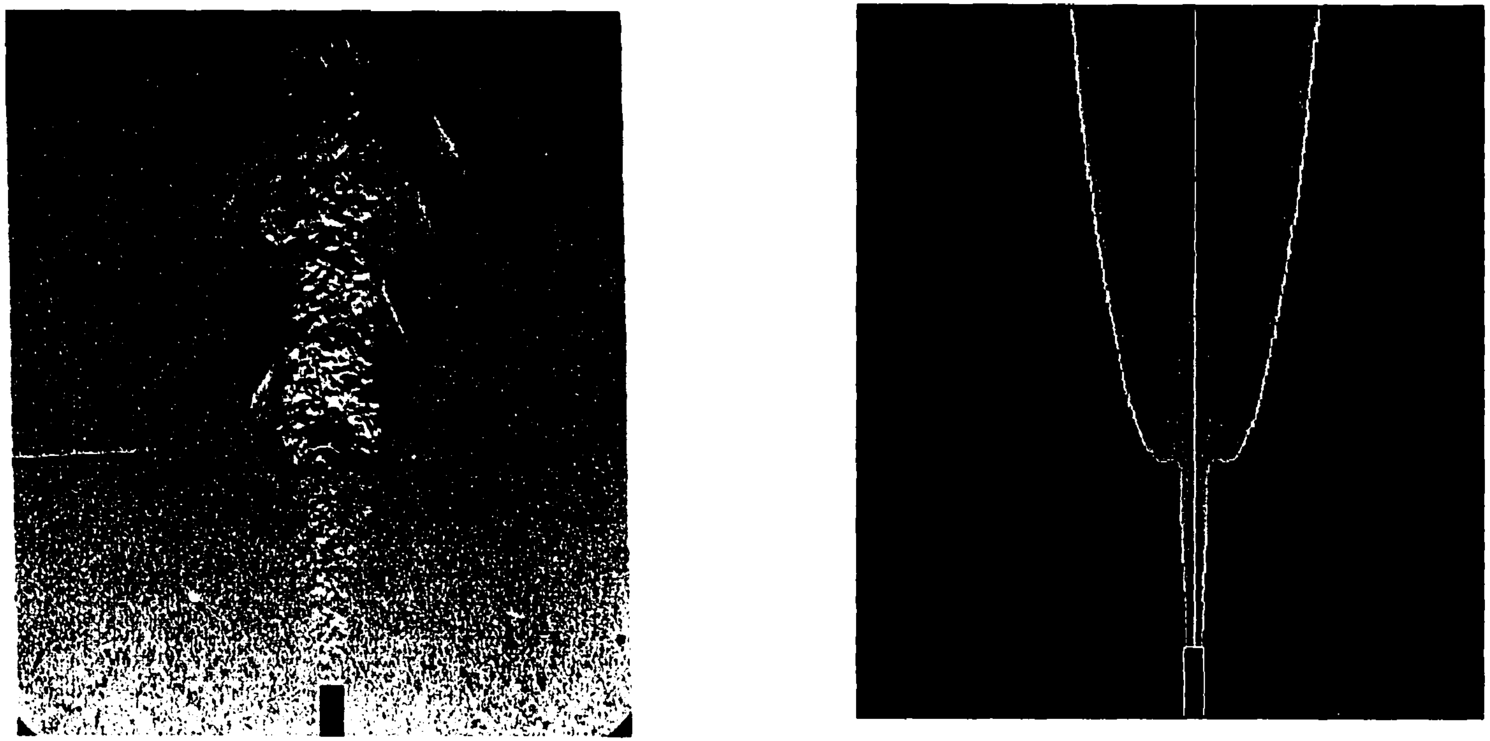

Experimental Results

Numerical Results

Fig. 4.14 Numerical prediction of flame structure as compared to experimental results. Fuel jet exit velocity 34.7 m/s, and flame base height of 5.9 cm (Exp) and 5.1 cm (Num.).

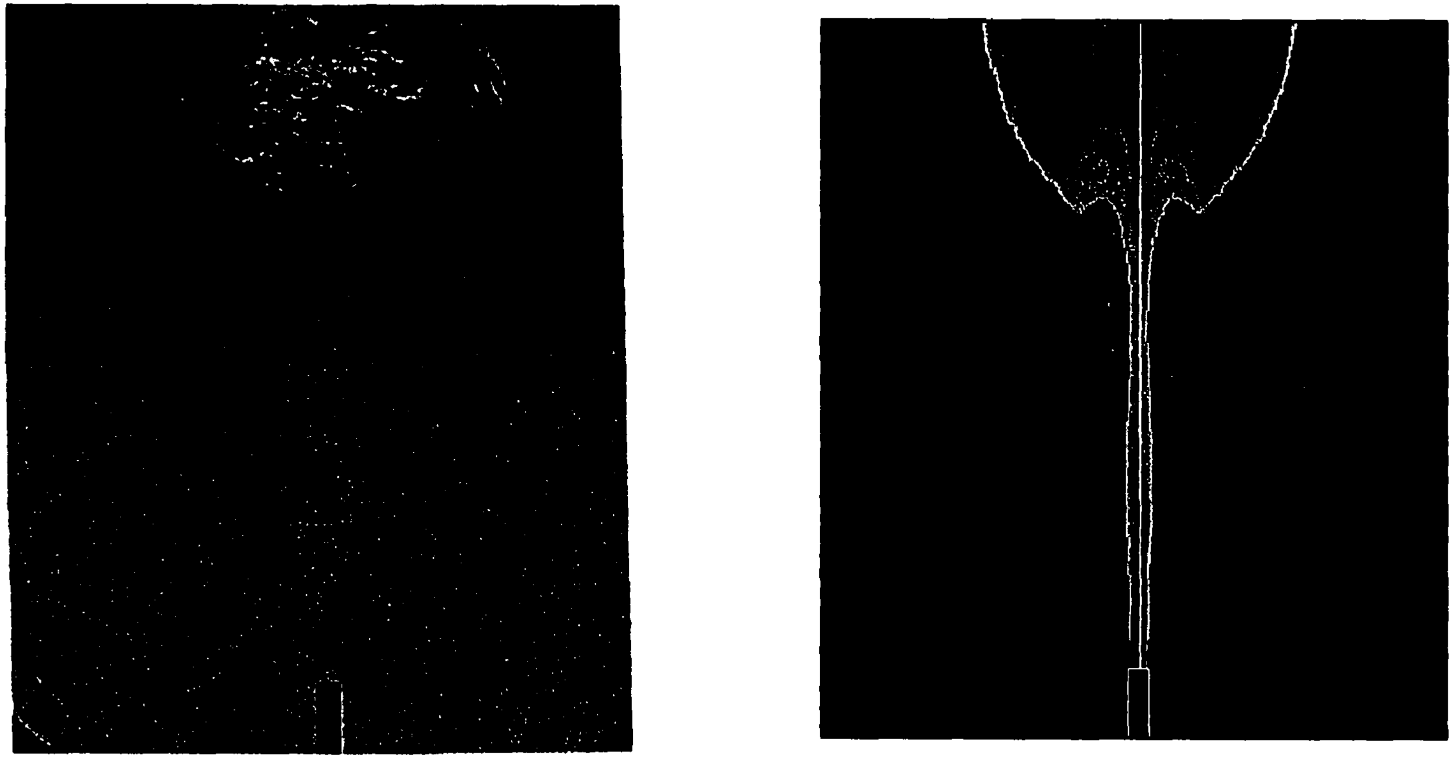

Experimental Results

Numerical Results

Fig. 4.15 Numerical prediction of flame structure as compared to experimental results. Fuel jet exit velocity 62.5 m/s, and flame base height 12.7 cm (Exp.) and 10.9 (Num.)

flame base height are also evident from both cases. Figures 4.16 and 4.17 show the flame temperature contours predicted in the present study for fuel jet velocities ranging from 19 m/s to 62.5 m/s. Some general observations can be made concerning the flame structure. The first one relates to the fact that for all jet velocities the flame is clearly lifted from the injection point. Also, the flame base height increases as the fuel jet velocity is increased. One visible effect is that the flame, as expected, becomes wider and longer in height and the flame base width increases with the increasing fuel jet velocity. It can also be observed that for every flame except the one for 62.5 m/s case, there is a conical core region centered around the axis where the unreacted fuel penetrates into the interior region of the flame. This region is characterized by high methane and low oxygen concentrations, and low temperature. The unreacted fuel jet penetration depth relative to the flame base height decreases with increasing jet velocity, thus resulting in the flame base flattening as evident from the highest velocity case. In fact, in this case the numerical flame exhibits a double dip. The flame front advances upstream in the axial region, thus forming a local flame base, in addition to the flame base at an off-axis location for other jet velocity cases. This flame base broadening is also evident in the Schlieren photograph (Fig. 4.15) taken from the study by Comer et al. [8]. All flames shown in these figures extend in axial direction beyond the chosen numerical domain. In order to resolve the question of truncated computational domain affecting the flame base height calculations, a longer axial domain of about one meter length was chosen as shown in Fig. 4.18 for the 34.7 m/s jet velocity case. This calculation produced a full flame in the computational domain. The flame base height calculated from the larger domain

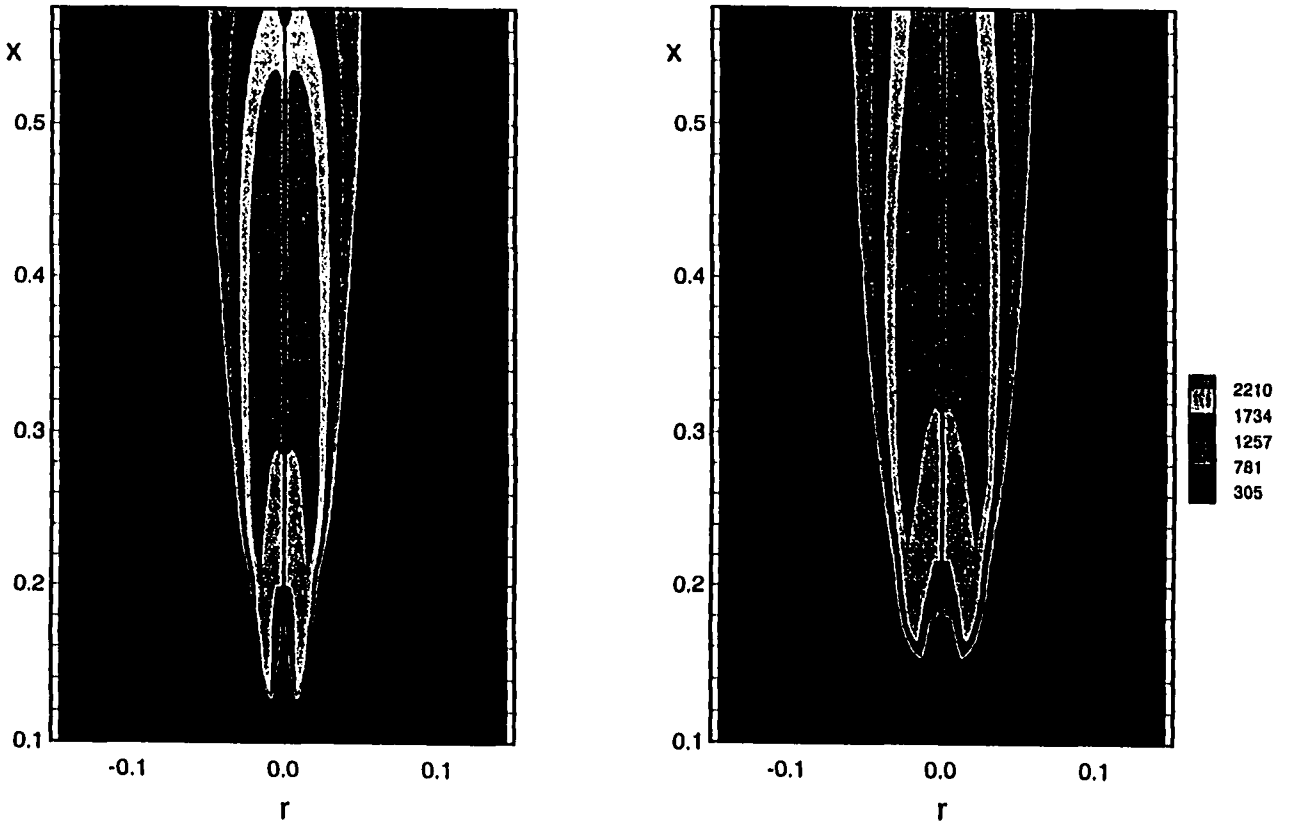

(a) (b)

Fig. 4.16 Prediction of temperature field for flames at exit jet velocities of (a) 19 m/s, and (b) 34.7 m/s.

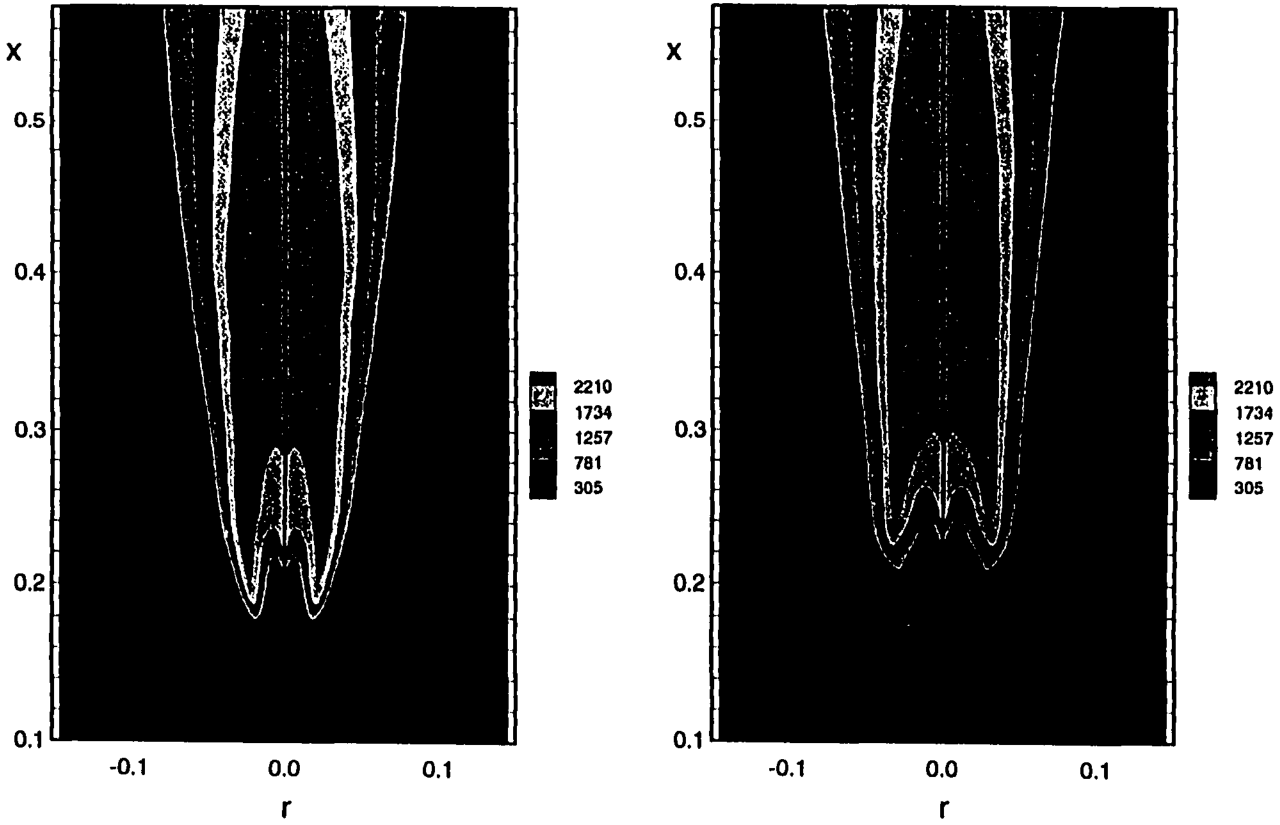

(a) (b)

Fig. 4.17 Prediction of temperature field for flames at exit jet velocities of (a) 47.5 m/s, and (b) 62.5 m/s.

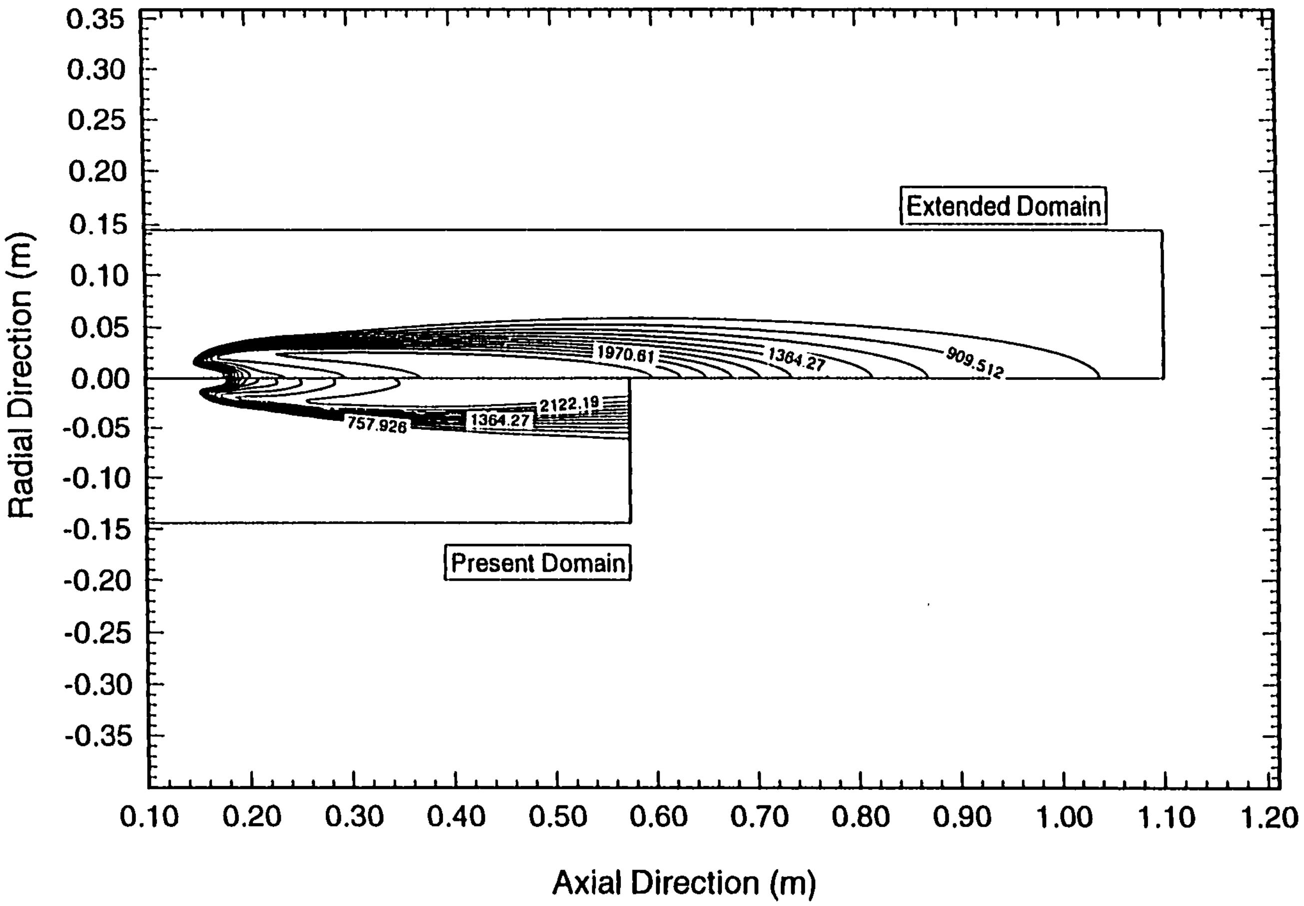

Fig. 4.18 Effect of extended domain length on the flame lift-off and structure predicted by (RSM) model for a fuel jet exit velocity of 34.7 m/s.

differed from the one for the truncated flame in the smaller domain flame (Fig. 4.18) by less than 0.5 %. This validated the present approach of reducing the computational domain to calculate the flame base height.

Species Concentrations

Detailed measurements of species using the methane burner are not available in Ref. 8 for many of the velocity values used in present study. In order to assess the accuracy of the turbulence and combustion models presented in the study, detailed comparison of predicted species concentrations with experiments must be accomplished. A comparison of predicted numerical results with the experimental data by Eickhoff and coworkers [81] has been made in this section. First, results of species profiles, predicted for the jet exit velocity of 34.7 m/s and tube diameter of 4.6 mm, are reported. Subsequently results for a different jet velocity and diameter are compared with results of Eickhoff et al. [81]. Figures 4.19 shows the computed profiles of O_2, CH_4, CO and CO_2 mass concentrations at four axial locations, namely $x = 2.325, 4.425, 4.863$, and $5.337\ cm$ respectively. The first two locations are upstream of the flame base stabilization point, the third location is near the flame stabilization point, and the last axial location is slightly after the stabilization point. The sharp decrease in O_2 concentrations and increase in CO and CO_2 concentration near the flame base is evident. It is further noted that there is depletion of oxygen concentration just before the flame base, primarily due to gradual build up of reaction rate as the flame base is approached along the axial traverse.

The comparison of the species concentration profiles predicted from the present study with experimental results from Eickhoff et al. [81] are given in Figs. 4.20 - 4.22. The mean radial profile of CH_4 mole fraction at a location of 8 cm downstream of the flame base is shown in Fig. 4.20. The numerical and experimental values are in good agreement. Figures 4.21 and 4.22 show the radial profiles of the mole fractions of CO and CO_2 respectively. The comparison is good with the experiments except in the region near the axis. Similar discrepancies in the mole fraction profiles have also been observed in other numerical studies [69, 86, 87] when compared with experiments.

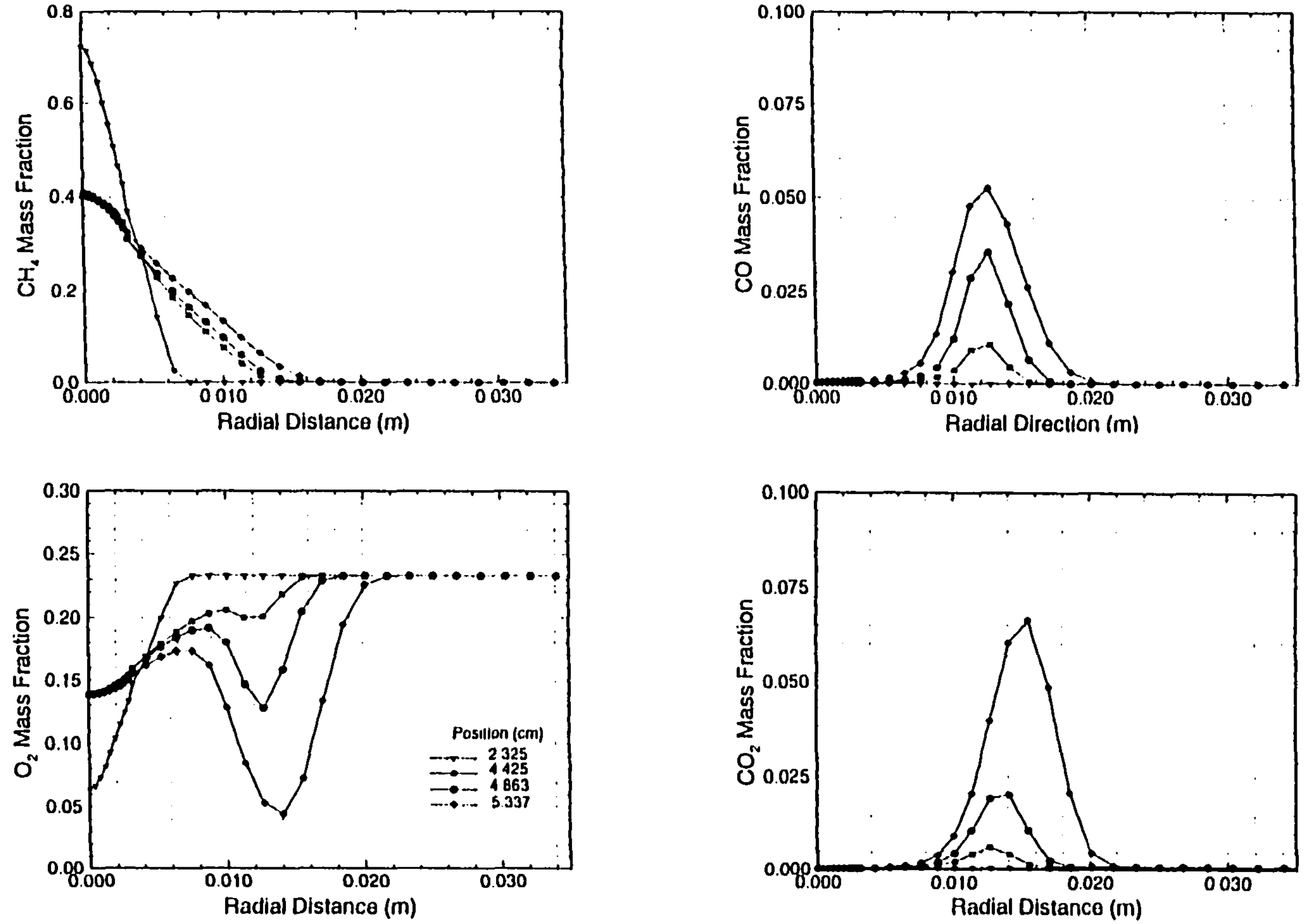

Fig. 4.19 Radial profiles of species mass concentrations at different axial locations for jet exit velocity of 34.7 m/s.

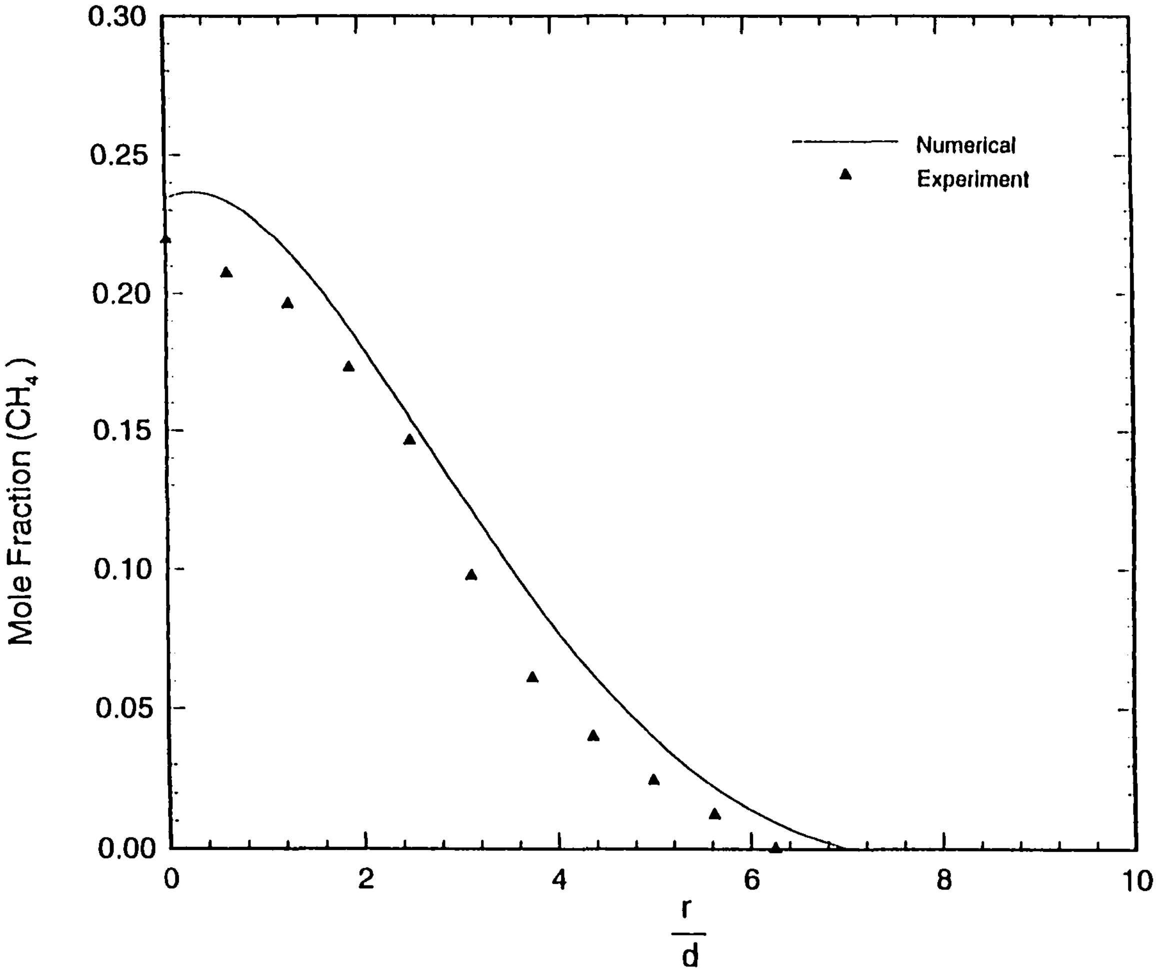

Fig. 4.20 Comparison of predicted CH_4 concentration with experimental measurements at an axial location 8 cm from the base.

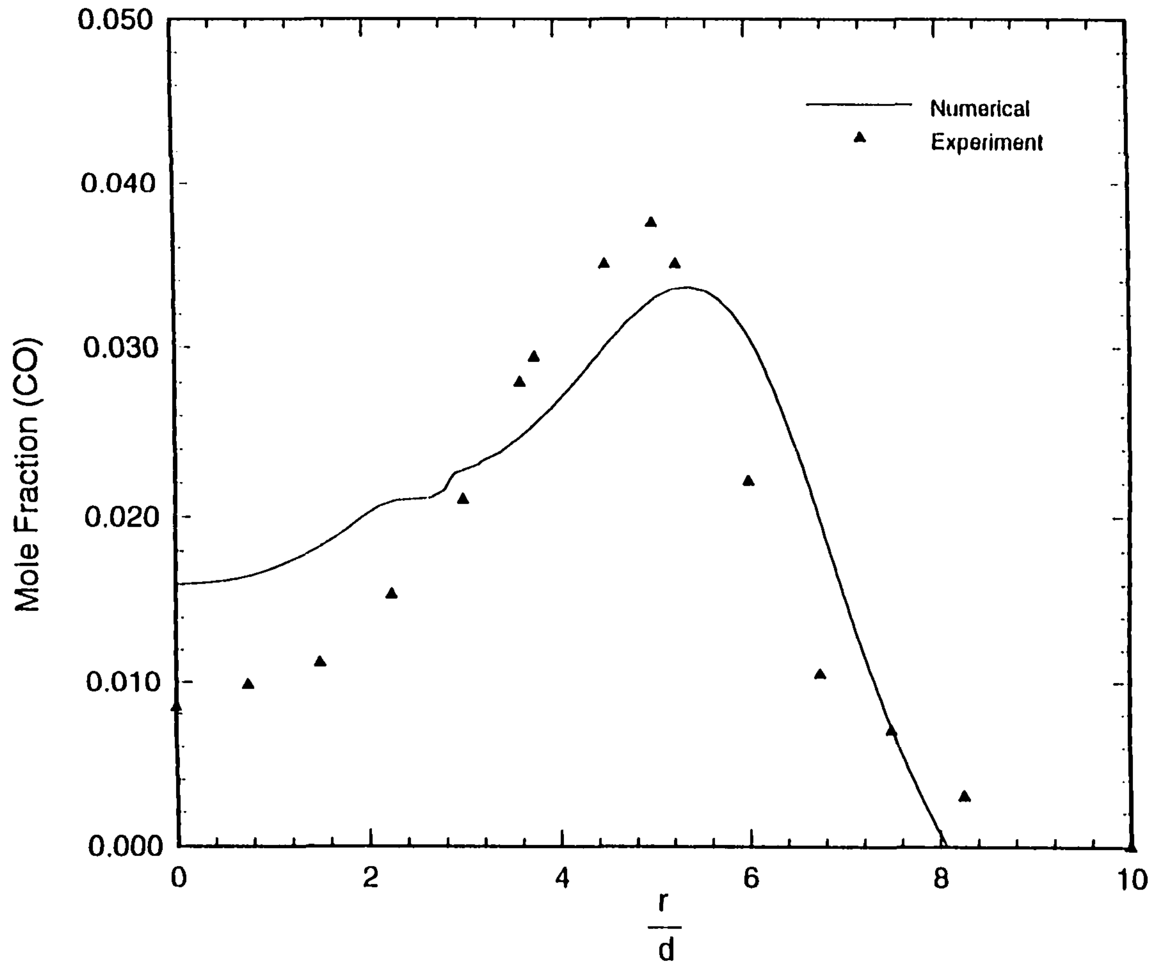

Fig 4.21 Comparison of predicted CO concentration with experimental measurements at an axial location 8 cm from the base.

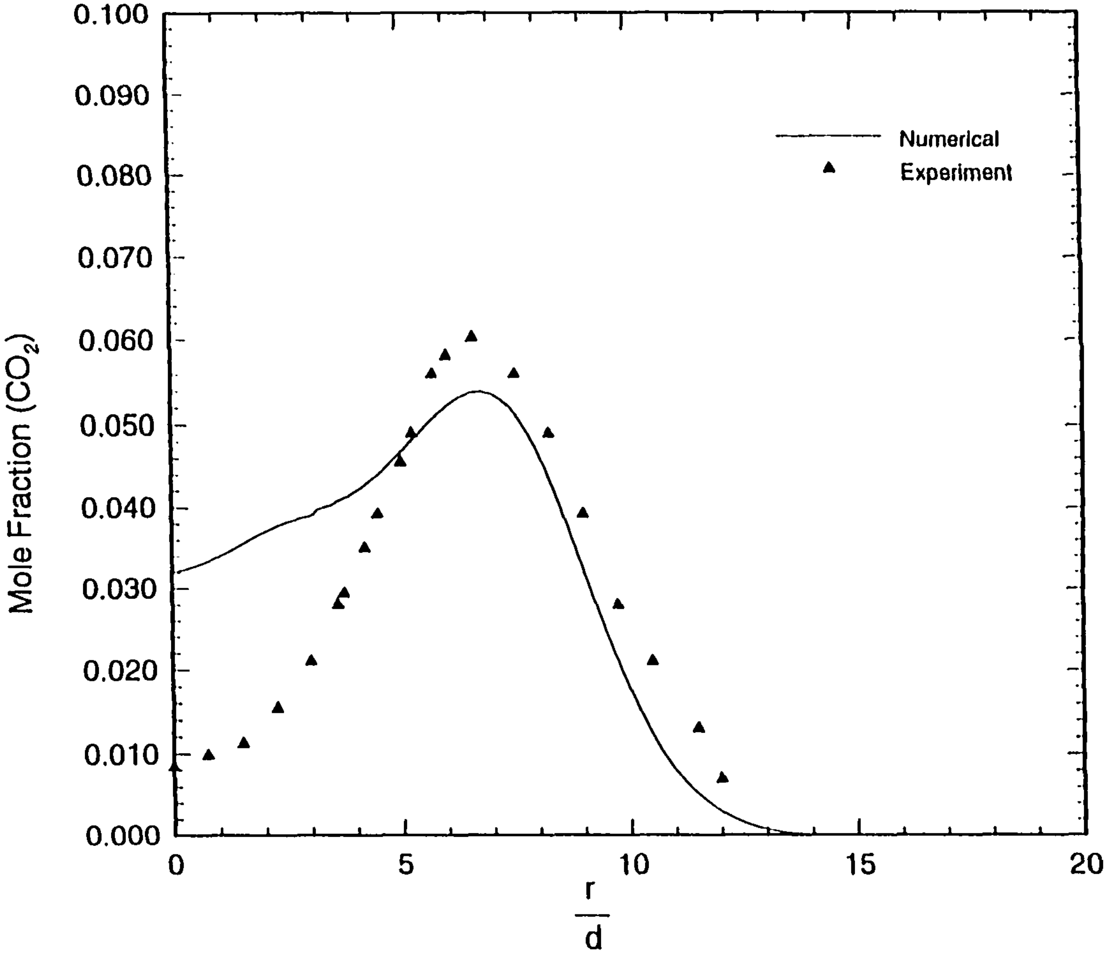

Fig. 4.22 Comparison of predicted CO_2 concentration with experimental measurements at an axial location 8 cm from the base.

4.4 Flame Lift-off Results

Prediction of the flame base height is important in design of combustors, and in determination of thermal loads on flame holders and other combustor surfaces. As illustrated in Section 3.4, there are different approaches for locating the flame base. In this section, the concept of premixed flame base and turbulent flame speed (S_t), based on hypothesis of Vanquickenborne and van Tiggelen [3] is used to predict the flame base height. Figure 4.23a shows a sketch of radial variation of turbulent flame velocity (S_t) along with the variation of the local flow velocity (u). This figure was proposed by Vanquickenborne and van Tiggelen to demonstrate the mechanism for locating the flame base in diffusion flames. It is noted that at all axial locations $x<h$, where h is the flame base height, the values of S_t remain smaller than that of u at all r locations. However, at one value of radial location the S_t curve is tangent to the u curve at the axial location $x=h$. According to the hypothesis, this is the flame stabilization point. In order to keep the flame in stable equilibrium, it is necessary that at any height, $x>h$, the flow velocity should remain smaller than S_t, at least over a certain width, Figure 4.23b shows the hypothetical shape of turbulent flame. One observes that the flame base is anchored in a premixed region, bounded by the upper and lower flammability limits.

Figure 4.24 shows the radial variations of axial component of flow velocity, and the turbulent flame velocity obtained here from the present procedure using the RSM and the eddy dissipation model. Three axial locations namely $x = 4.2\ cm$ (upstream of the flame base), $x = 5.1\ cm$ (flame base) and $x = 6.0\ cm$ (downstream) are shown. At the upstream location, the flame velocity is lower than the flow velocity at all radial

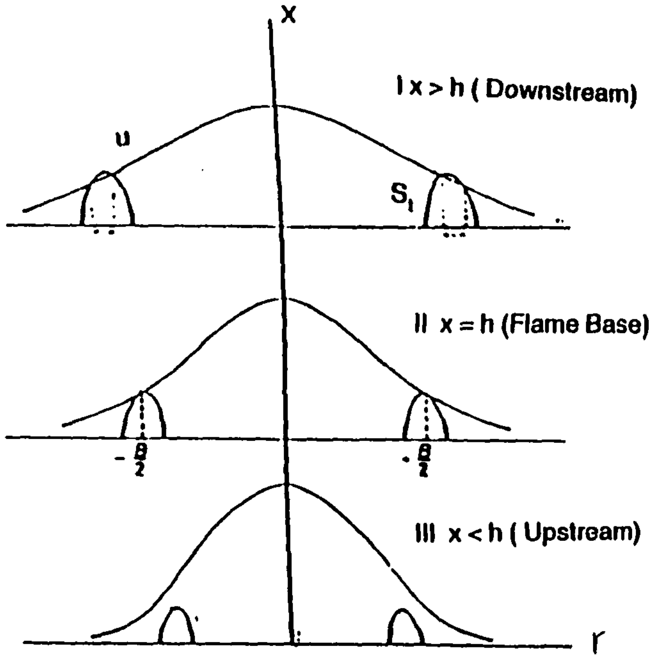

Fig. 4.23a Velocity and turbulent flame speed at three axial locations.

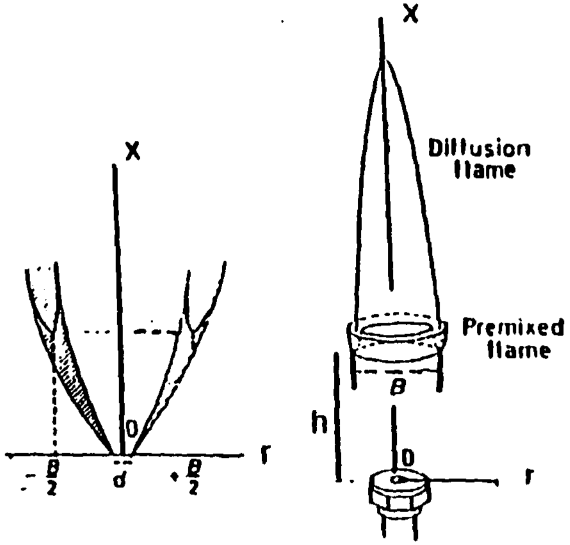

Fig. 4.23b Hypothetical shape of premixed flame with the upper and lower flammability limits.

locations. The profiles at the flame base exhibits the tangency condition, while profiles at the downstream location show that the flame velocity is greater than the flow velocity at several radial locations. These computed results are remarkably similar to those described by Vanquickenbourn and van Tigglen in their classical paper dealing with flame stabilization. Similar behavior was also observed for numerical results in Fig. 4.25 for the jet velocity of 62.5 m/s. At the point of tangency, characterizing flame stabilization point, the turbulent flame velocity equals the flow velocity. This condition has been used in the present study to determine the axial location of the flame base. It should also be remarked that the numerically calculated point at which the flame stabilizes lies on the stoichiometric line.

Figure 4.26 shows an expanded view of temperature contours near the flame base. Also superimposed on this figure are the numerically obtained values of mixture fraction. The 0.119, 0.05 and 0.033 values represent the upper flammability (rich) limit, stoichiometry case and the lower flammability (lean) limit, respectively. One observes that the potentially flammable region, based on the stability criterion, expands from a narrow width at the injection point to a larger width near the flame base. In this regard, one should also note a remarkable similarity between this figure and the one given by Vanquickenborne and van Tiggelen [3], Fig. 4.23b, who postulated anchoring of the lifted diffusion flame in a premixed region. From Fig. 4.26 one observes that the numerical flame is stabilized in the flammable region in the proximity of the stoichiometric methane contour. Similar observations also apply to cases with different jet velocity of 47.5 and 62.5 m/s, as depicted in Figs. 4.27 and 4.28.

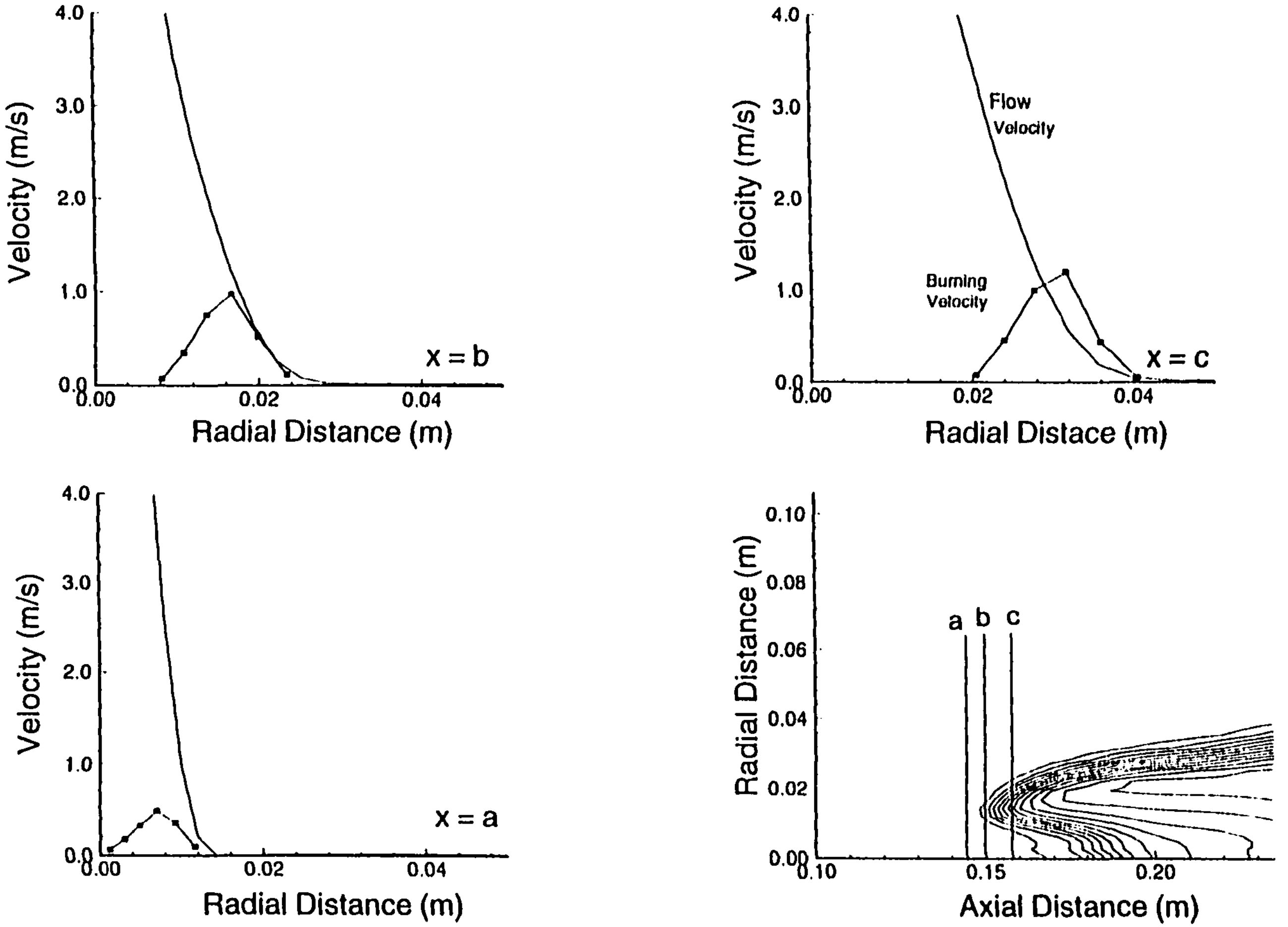

Fig. 4.24 Velocity profiles at different axial locations (a=.042m, b=.051m & c=.06m) for a fuel jet exit velocity of 34.7 m/s. —— flow velocity, ▪ turbulent burning velocity

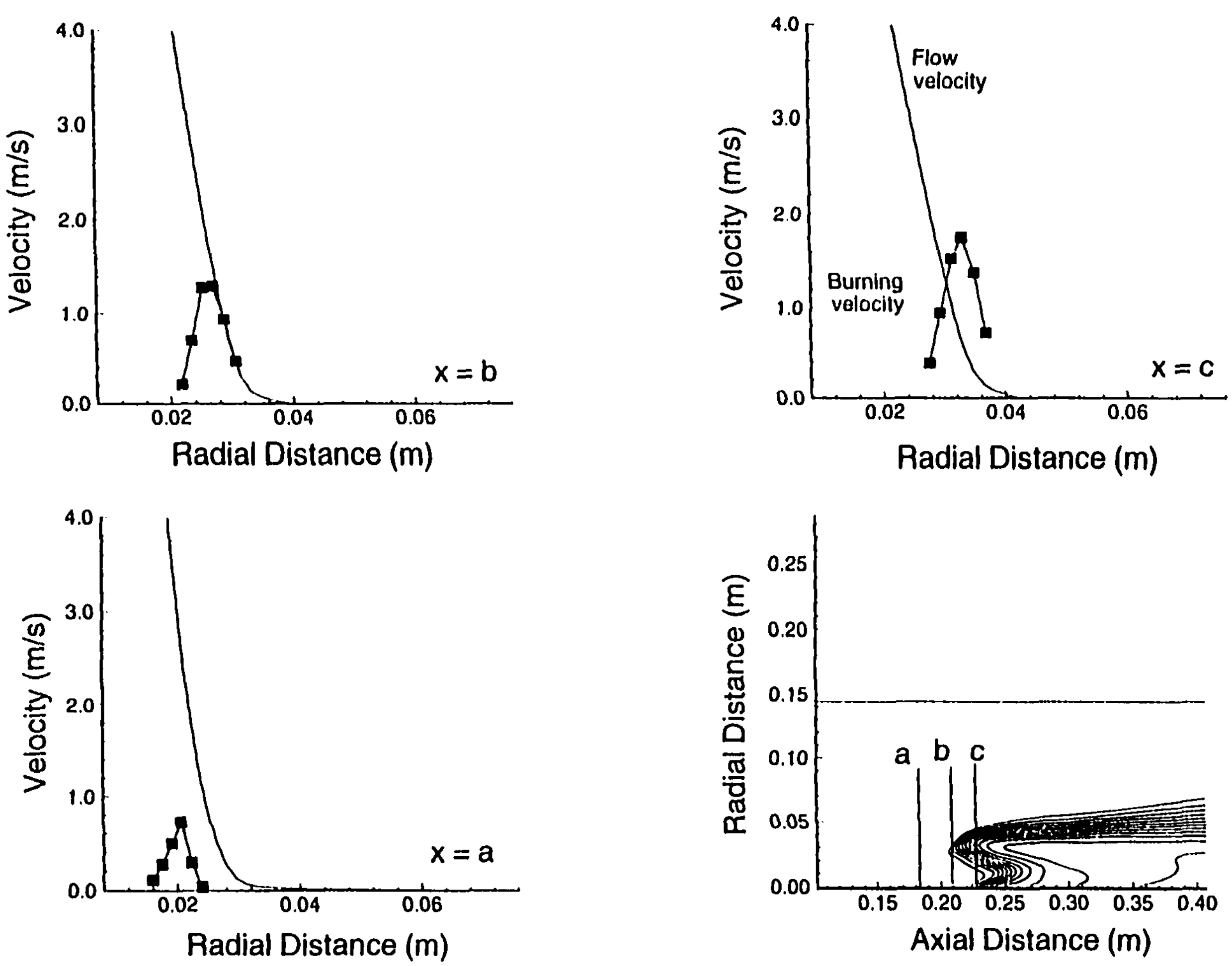

Fig. 4.25 Velocity profiles at different axial locations (a=0.071m, b=0.109m & c=0.125m) for a fuel jet exit velocity of 62.5 m/s. flow velocity, --■-- turbulent burning velocity

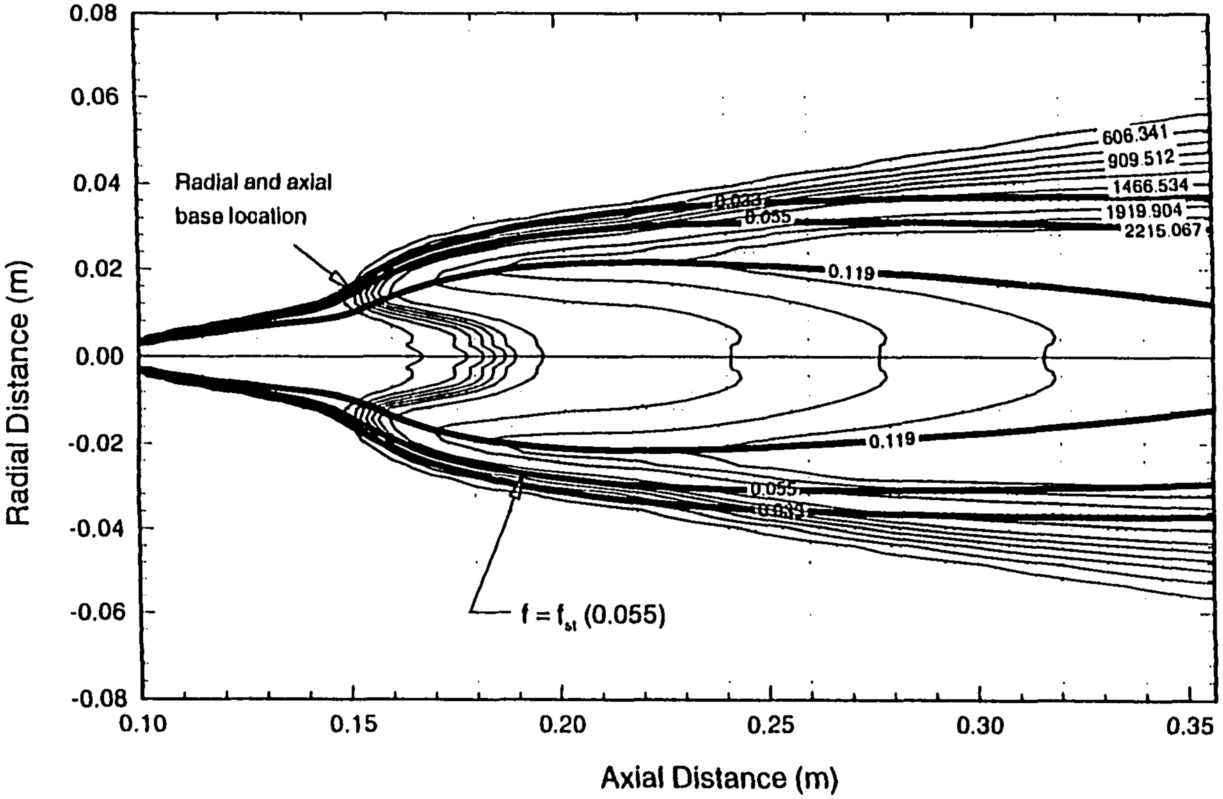

Fig. 4.26 Expanded view of temperature and mixture fraction (f) contours for the fuel jet exit velocity of 34.7 m/s.

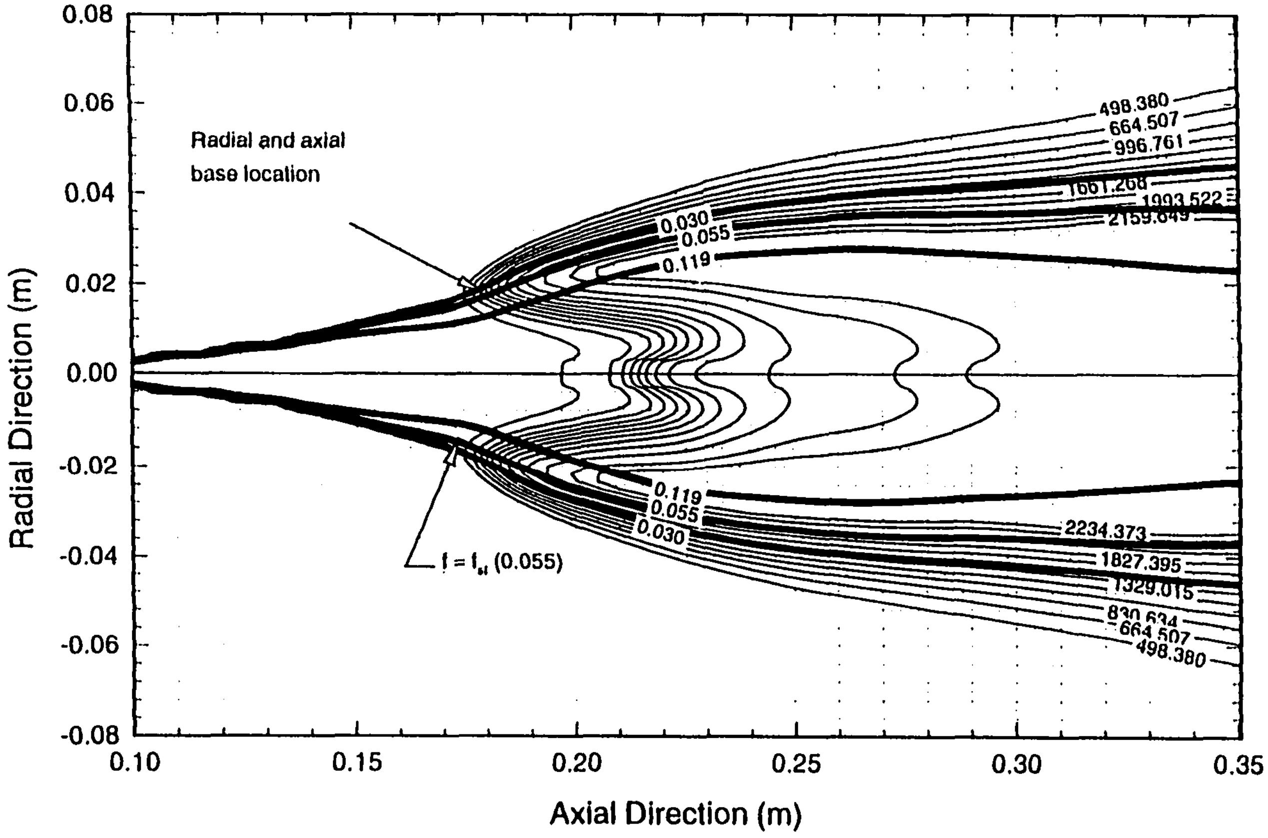

Fig. 4.27 Expanded view of temperature and mixture fraction (f) contours for the fuel jet exit velocity of 47.5 m/s.

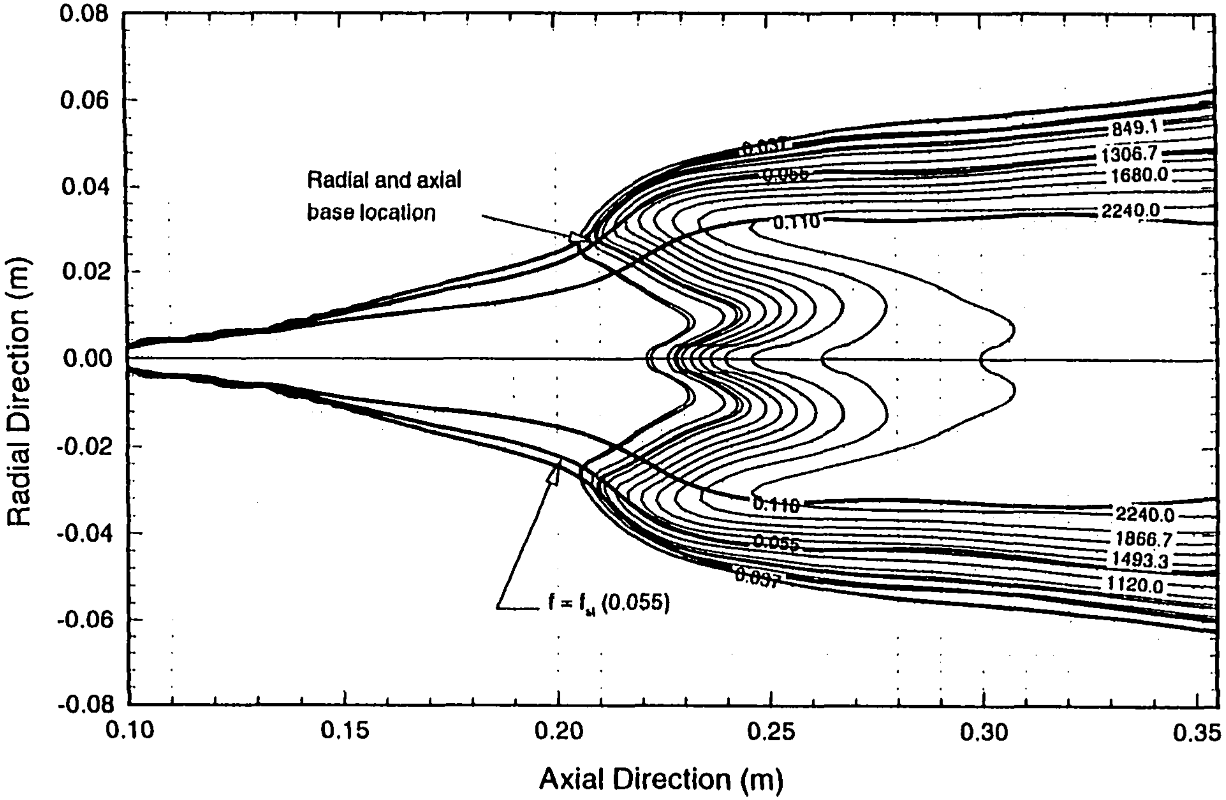

Fig. 4.28 Expanded view of temperature and mixture fraction (f) contours for the fuel jet exit velocity of 62.5 m/s.

Figure 4.29a shows the variation of flame base height (*h*), calculated from the present RSM and k-ϵ model, with the jet velocity. The criteria for predicting *h* is based on the tangency condition described in Figs. 4.24 and 4.25. Also, Fig. 4.29b shows the variation of the flame base height to tube diameter ratio with jet velocity to diameter ratio. Results from the present study are compared with other existing numerical as well as experimental results. This figure clearly indicates the fact that experimental results of various previous studies do not agree quantitatively with one another. For example, results reported by Annushkin and Sverdlov are much lower compared to those reported by Kalaghatgi. It is noted that the present numerical results are in reasonable agreement with experimental results reported by Comer et al. [8]. As indicated earlier, and seen from Fig. 4.29a, it is evident that the k-ϵ model grossly underestimates the flame base height. Present results underestimate experimental results of Kalaghatgi at low *u/d* values. However, a better accord with experimental results is achieved at larger values of *u/d*. Numerical results also reveal a linear relationship between the flame base height and the fuel jet exit velocity. The numerical results of Peters and Williams, using laminar flamelet theory, generally underpredict the experimental results of Kalaghatgi. The slope of the flame base height versus jet velocity curve, reported by Rokke et al. [31] using Peters and Williams model, has a value of 1.3×10^{-3} as a compared to a value of 1.45×10^{-3} obtained from the present study.

Figure 4.30 shows the variation of the u-component of velocity and temperature along an axial traverse at a radial location of $r = 0.0165\ m$, a location coincident with the flame base stabilization point for the 34.7 m/s jet velocity case. The temperature remains

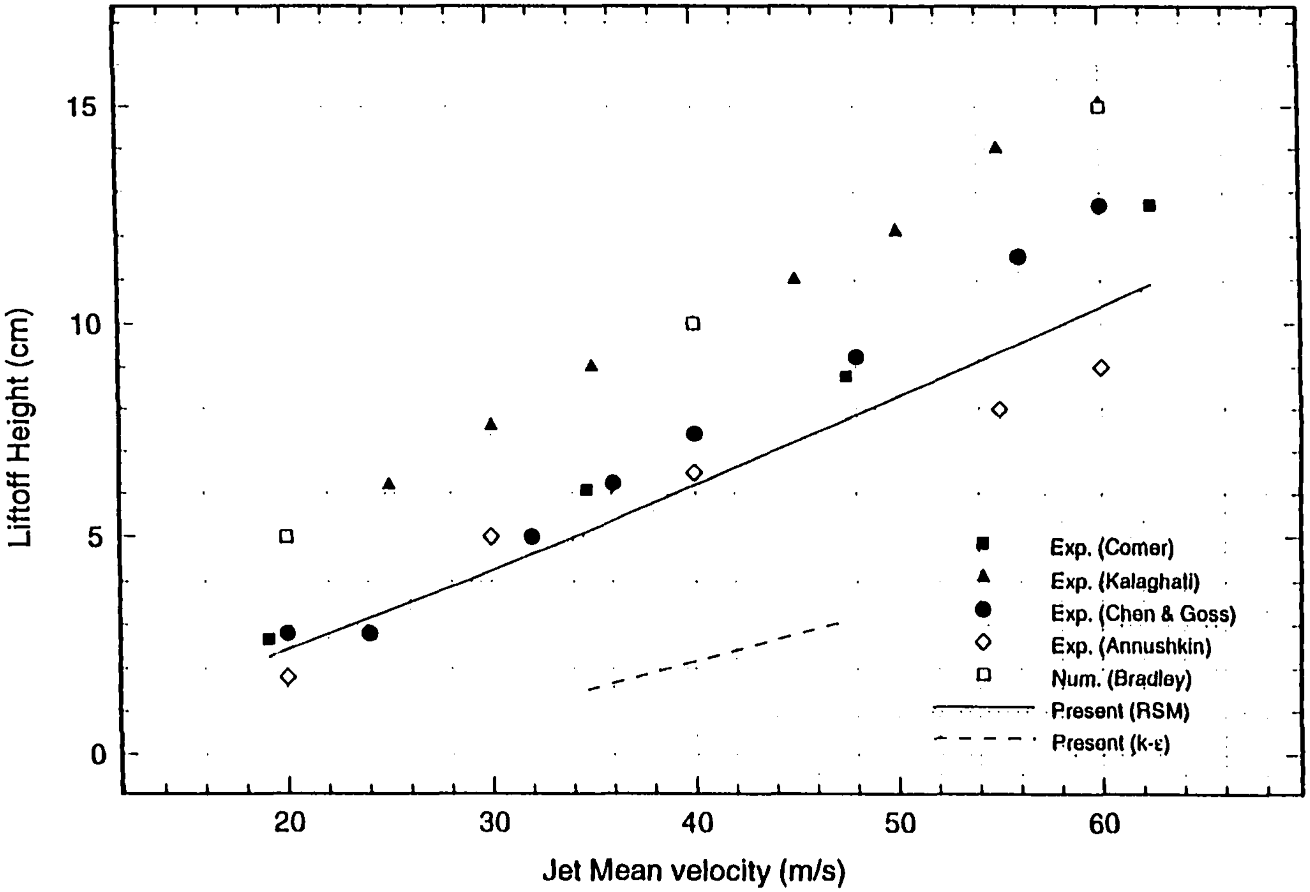

Fig. 4.29a Variation of flame base height with jet exit velocity, and comaprison with experiments and other numerical results.

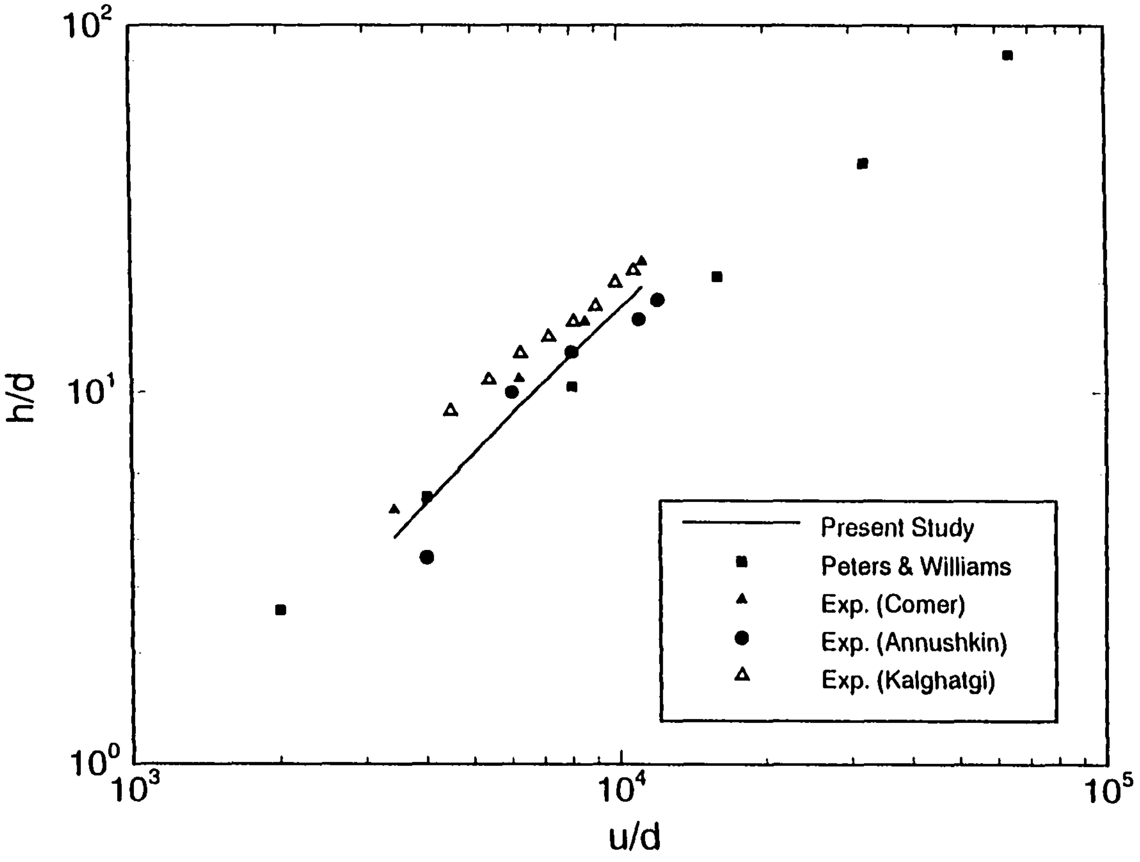

Fig.4.29b Variation of flame base height to tube diameter ratio with fuel jet velocity to diameter ratio.

relatively constant in the region upstream of the flame base, and then rises steeply as the flame base is approached. The u-velocity component first shows a steady decline along the x-direction, reaches a zero value and then increases sharply due to the heat release that causes a sharp drop in density. This feature has been described by Bradley et al. [13] as the thermal expansion zone. This is further illustrated in Fig. 4.31 which shows the velocity field superimposed on the temperature field of the flame. The fuel jet entrains surrounding air which sustains combustion in the flame. It is also noted that at off axis locations has a velocity field in which the u-component of velocity is quite small. However, in the premixed region near the flame base, due to thermal expansion, the u-component of velocity vector becomes quite large, and shows a sharp rise along the x-direction.

Figure 4.32 shows the temperature field superimposed with the contours of the strain rate ($a=\epsilon/k$) and the mixture fraction (f). This figure is used to locate the stoichiometric value of a that is used to compute the non-dimensional scalar dissipation rate at different flame base height (Fig. 4.33). This figure shows an agreement with the experimental data by Bray et al. [82]. The term ΔZ_F is constant with a value 0.19 given in the reference.

Figure 4.34 demonstrates a different method for predicting the flame stabilization region through the calculation the fuel burnout rate. This methodology, due to Eickhoff et al. [81], was discussed in Chap. 3. The sudden steep rise in the burnout rates b(x) is

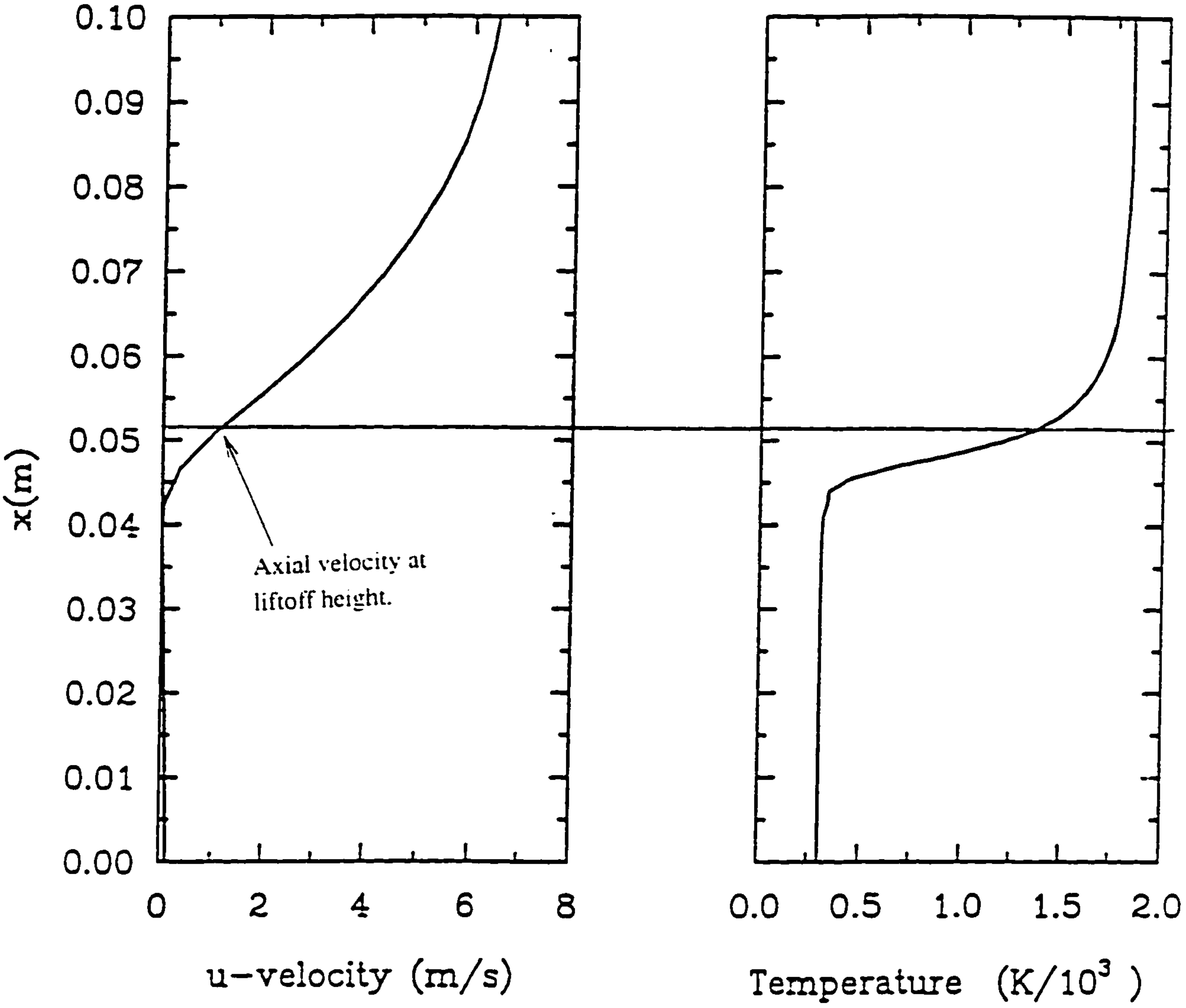

Fig. 4.30 Variation of u–component and temperature along axial traverse at radial location of 0.0165 m.

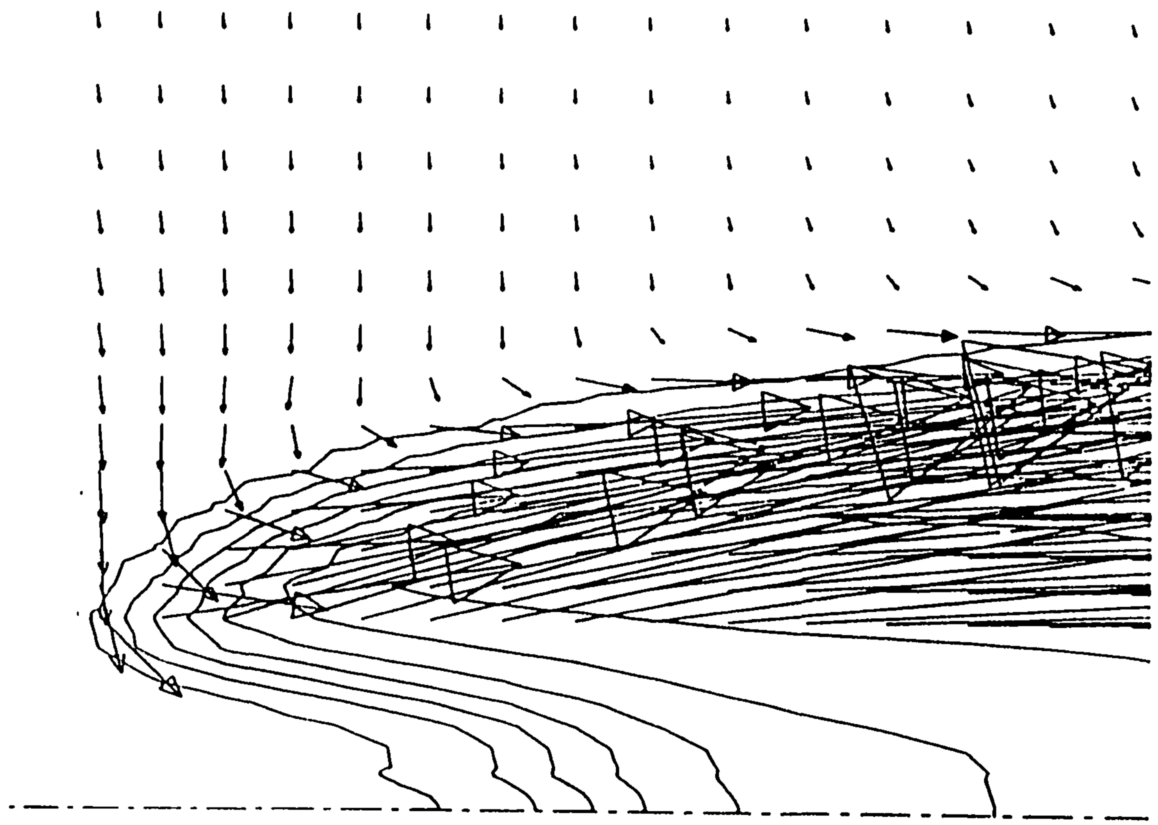

Fig. 4.31 Magnified view of velocity vectors and temperature field at the flame base

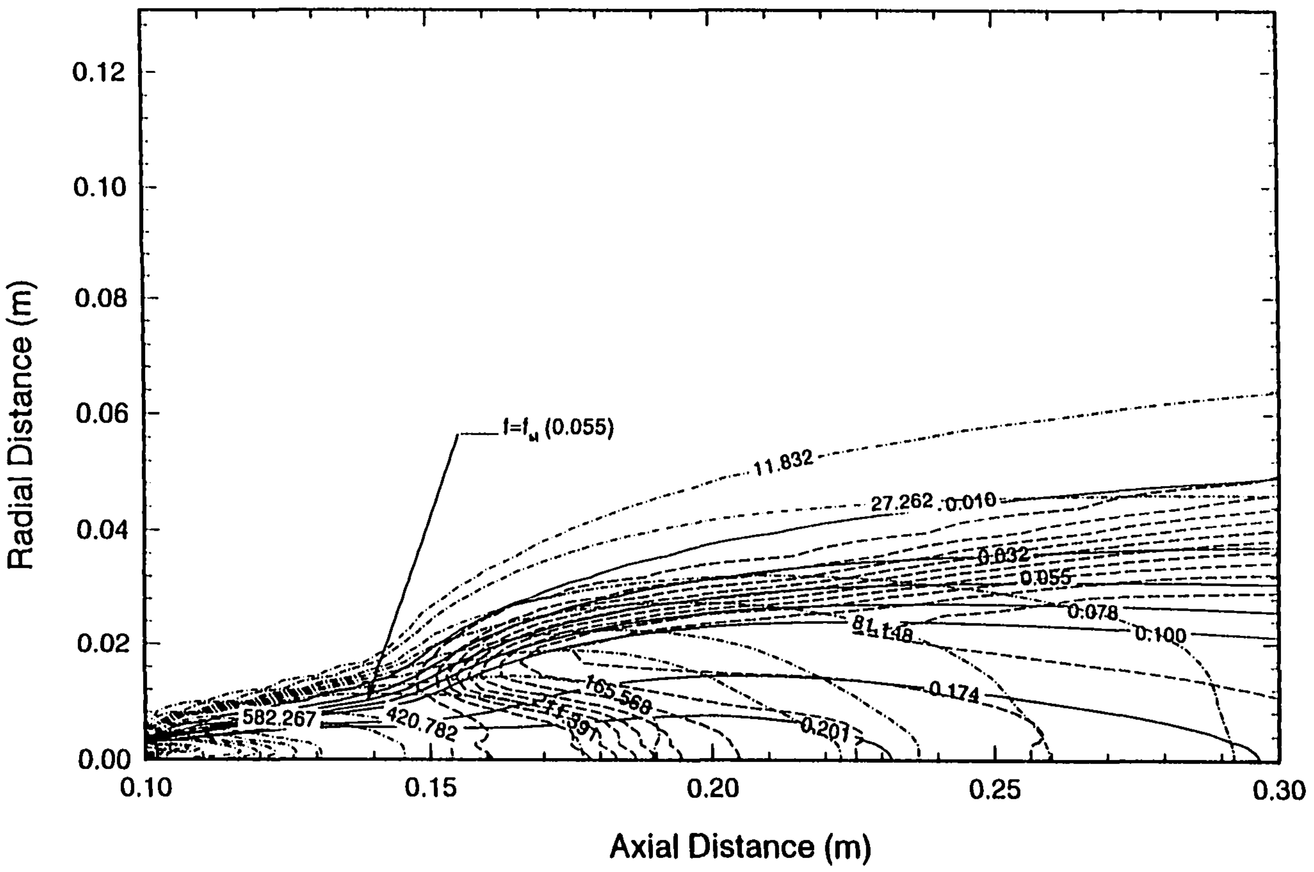

Fig. 4.32 Expanded view of temperature near the flame base along with contours for mixture fraction and strain rate (a=ε/k). Fuel jet exit velocity of 34.7 m/s.

—— Mixture Fraction — — Temperature (K) -·-·- Strain Rate

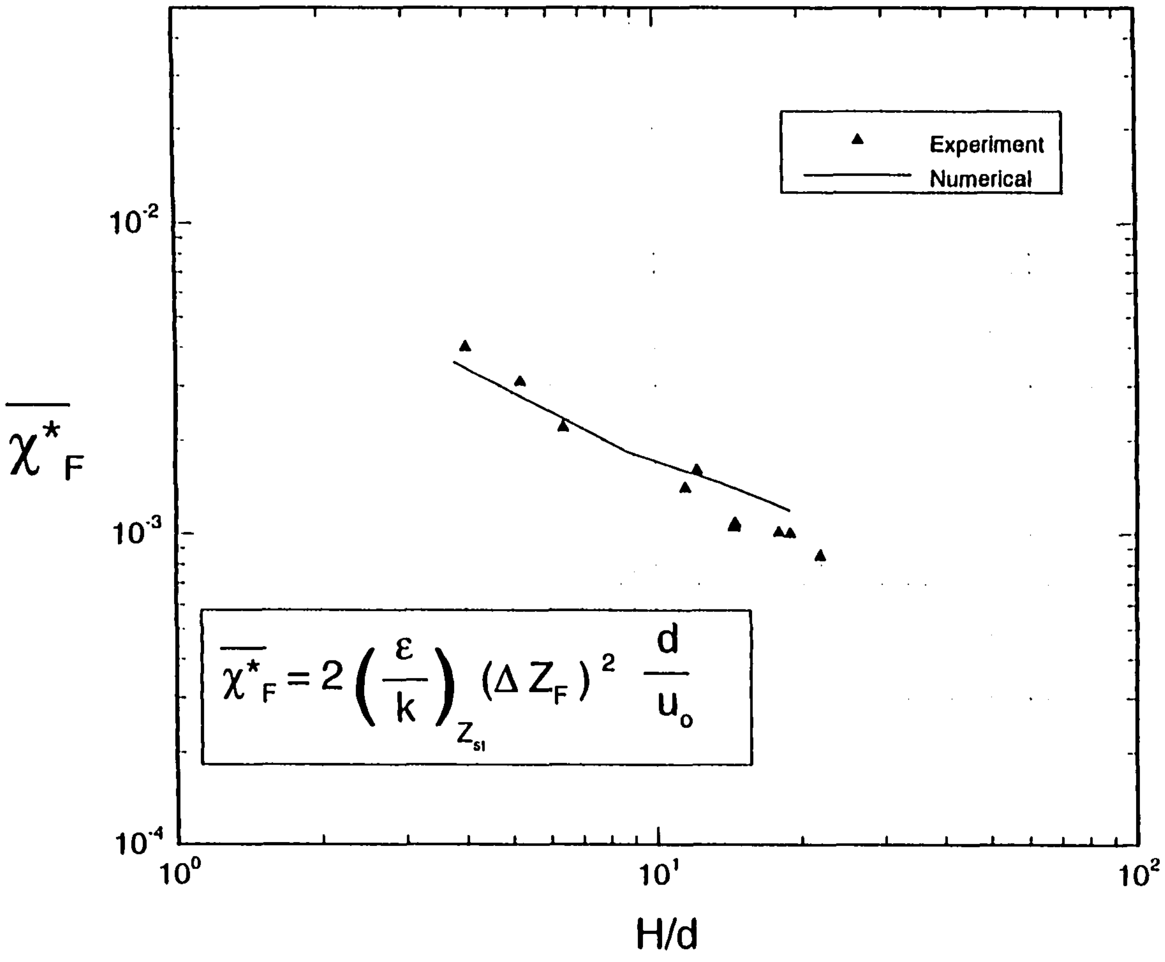

Fig. 4.33 Comparison of predicted non-dimensional scalar dissipation with experimental data for lifted methane flames.

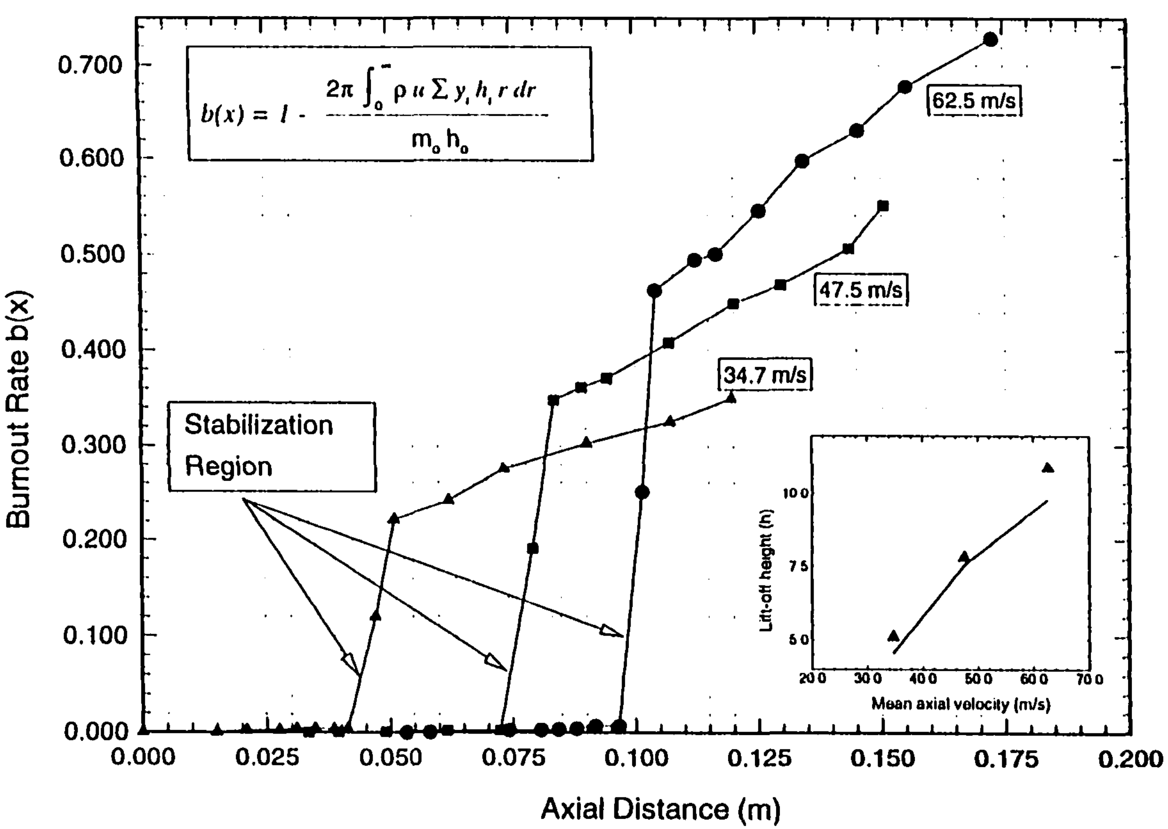

Fig. 4.34 Prediction of burnout rate along axial direction for jet exit velocity of 34.7 m/s, 47.5 and 62.5 m/s. Small graph represents lift-off height predicted using turbulent flame speed criteria (symbols) as compared to the above criteria (lines).

an indication of the axial location characterizing the beginning of the combustion and the base region of the flame. The lift-off height is compiled from the above figure and compared with the values obtained from the criterion based on the turbulent flame speed. The deviation is about 3 to 5 percent between the two predicted values of the lift-off height.

Prediction of Lift-off from Isothermal Jet

There is very little chemical activity between the flame base and the injection holder. Consequently, the flow field predicted in the non-reacting case should be similar to the one for the reacting case. We have conducted calculations for the non-reacting case to see if the above hypothesis is correct. Furthermore, we also explore the possibility if the flame base can be predicted approximately by consideration of this non-reacting case. Figure 4.35 shows the variation of axial velocity for the reacting and non-reacting cases. The non-reacting case shows a sustained decay with the axial distance, while the reacting case shows a bump in the axial velocity in the combustion zone. Similar behavior has been reported by Sanders and Lamers [12] in their numerical procedure. It is noted that upstream of the flame base (or the bump), results for both reacting and non-reacting cases are very close to one another. This is further illustrated in Figs. 4.36 and 4.37 by comparison of the numerically predicted results with reacting and non-reacting experimental results of $u'u'/u$ by Eickhoff et al. [81]. In these two figures the jet axial velocities are 50 and 70 m/s, respectively. From the experimental as well as numerical results, it is observed that the flow field upstream of the flame base is almost identical for both reacting and non-reacting cases. It should also to be noted that the agreement

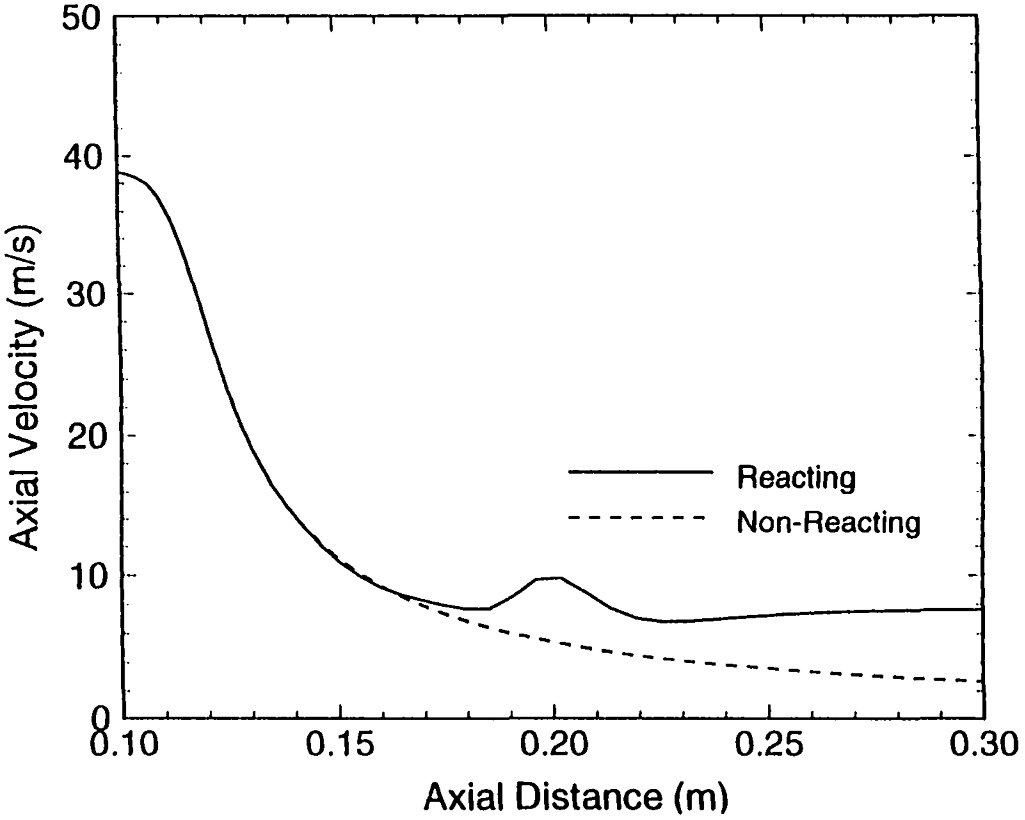

Fig.4.35 Computed axial velocity for reacting and non-reacting flows.

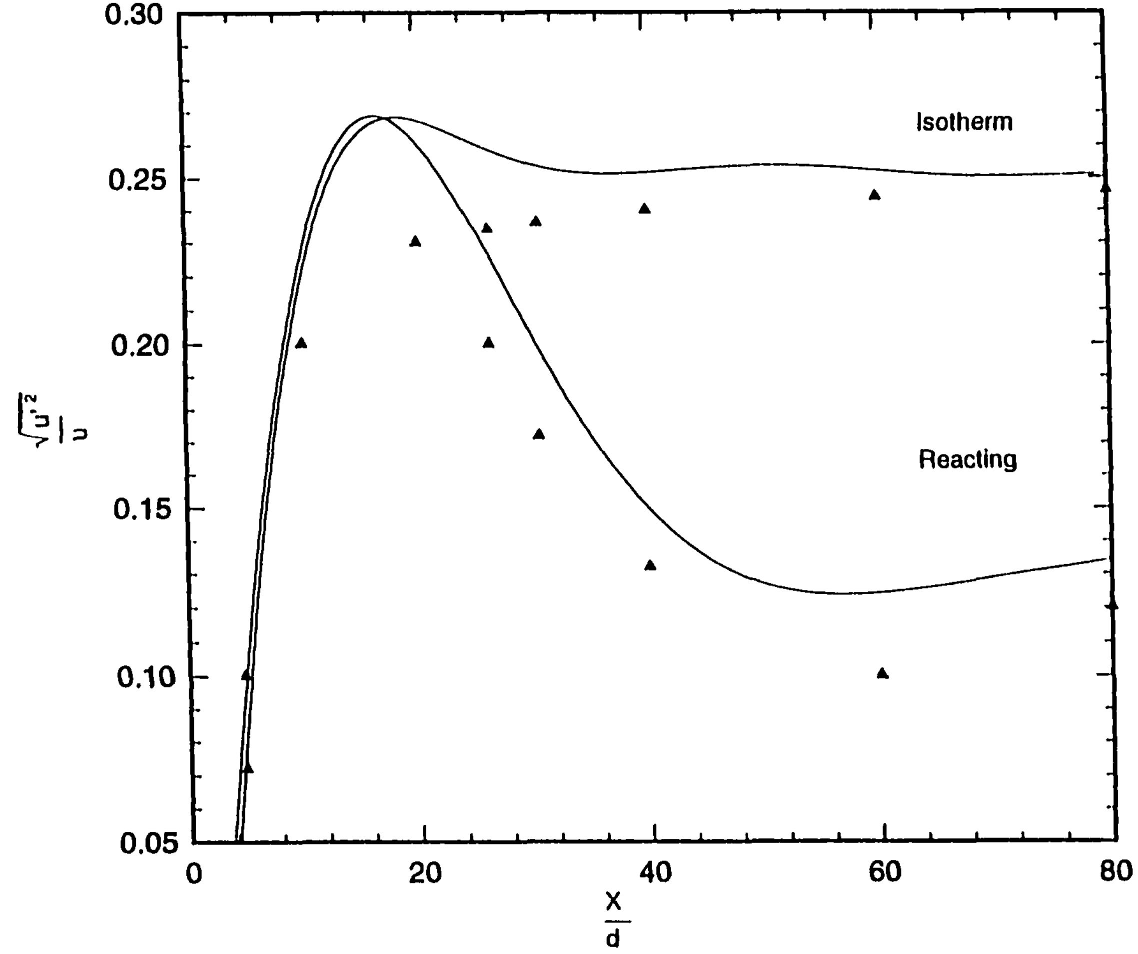

Fig. 4.36 Values of calculated turbulent intensity (solid line) as compared with experimental measurements (symbols) for the jet exit velocity of 50 m/s.

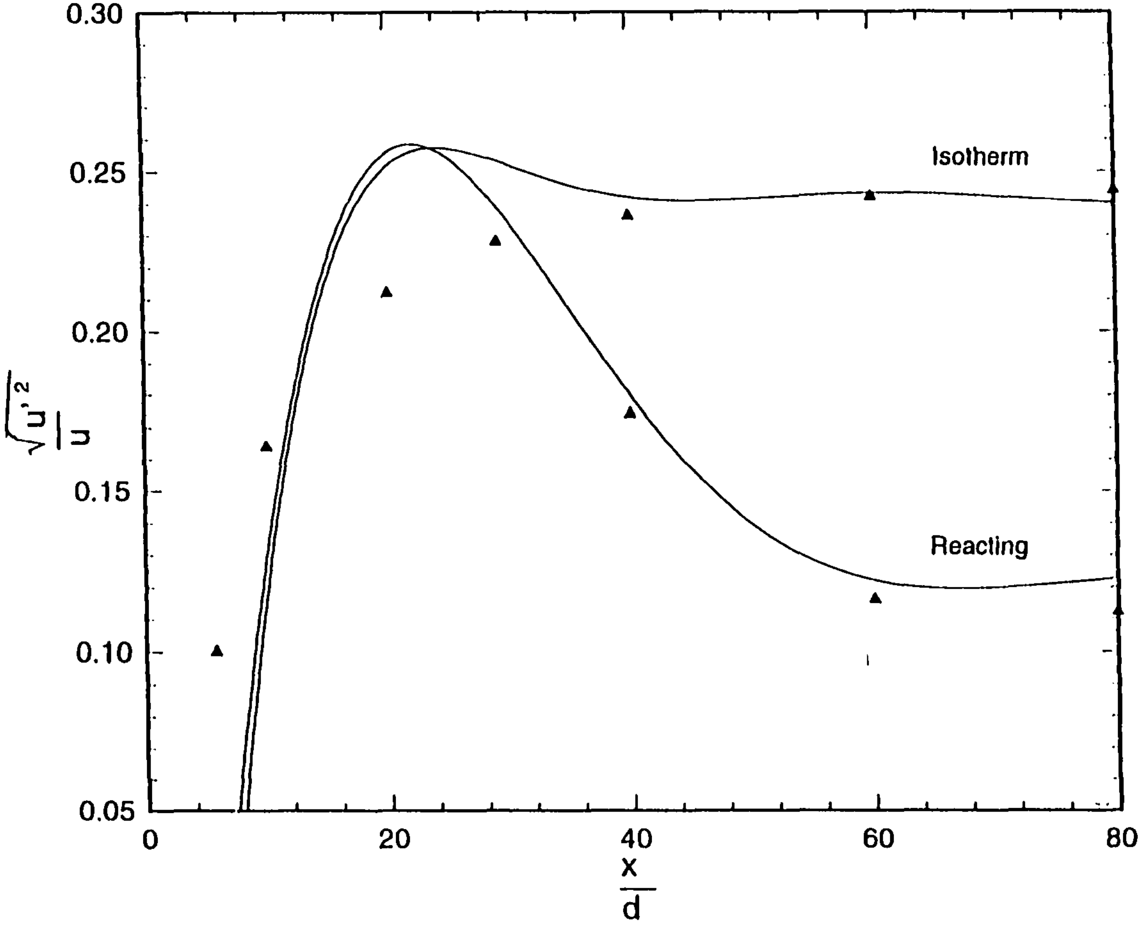

Fig. 4.37 Values of calculated turbulent intensity (solid line) as compared with experimental measurements (symbols) for the jet exit velocity of 70 m/s.

between the numerical calculations is reasonably good except for the peak values which are somewhat overpredicted in the numerical cases. Also the axial locations of the peak value point are somewhat underestimated in the numerical calculations.

We have attempted to identify the potential location of the flame base in the non-reacting case by using the procedure described in the previous section based on the tangency condition for the turbulent flame speed and the mean flow velocity profiles. Figure 4.38 shows the variation of the u-component of velocity and the turbulent flame velocity for the non-reacting case at four axial locations namely, x=0.022 m, x=0.034 m (upstream), x=0.049 (potential flame base location) and x=0.06 (downstream). It is noted that even in the non-reacting case the patterns are remarkably similar to those predicted for the reacting case. The tangency condition predicts the potential location of the flame base at x=0.049 for the 34.7 m/s jet axial velocity case. This compares well with a value of x=0.051 m for the reacting case. Figure 4.39 shows results for the axial jet velocity of 62.5 m/s. Again four axial locations are considered. The first two locations are upstream of the flame base, namely x=0.059 m and 0.066 m, the third location is at x=0.098m (potential flame base location) and the fourth location is at x=0.135 m (downstream). The value of flame base height of 0.098 m, based on tangency condition, compares well with a value of 0.109 m for the reacting case. Figure 4.40 shows the variation of the flame base height with the fuel jet velocity as predicted from both reacting as well as non-reacting cases. All results were calculated using the Reynolds stress model. The results for the non-reacting case are within 10 percent of the reacting

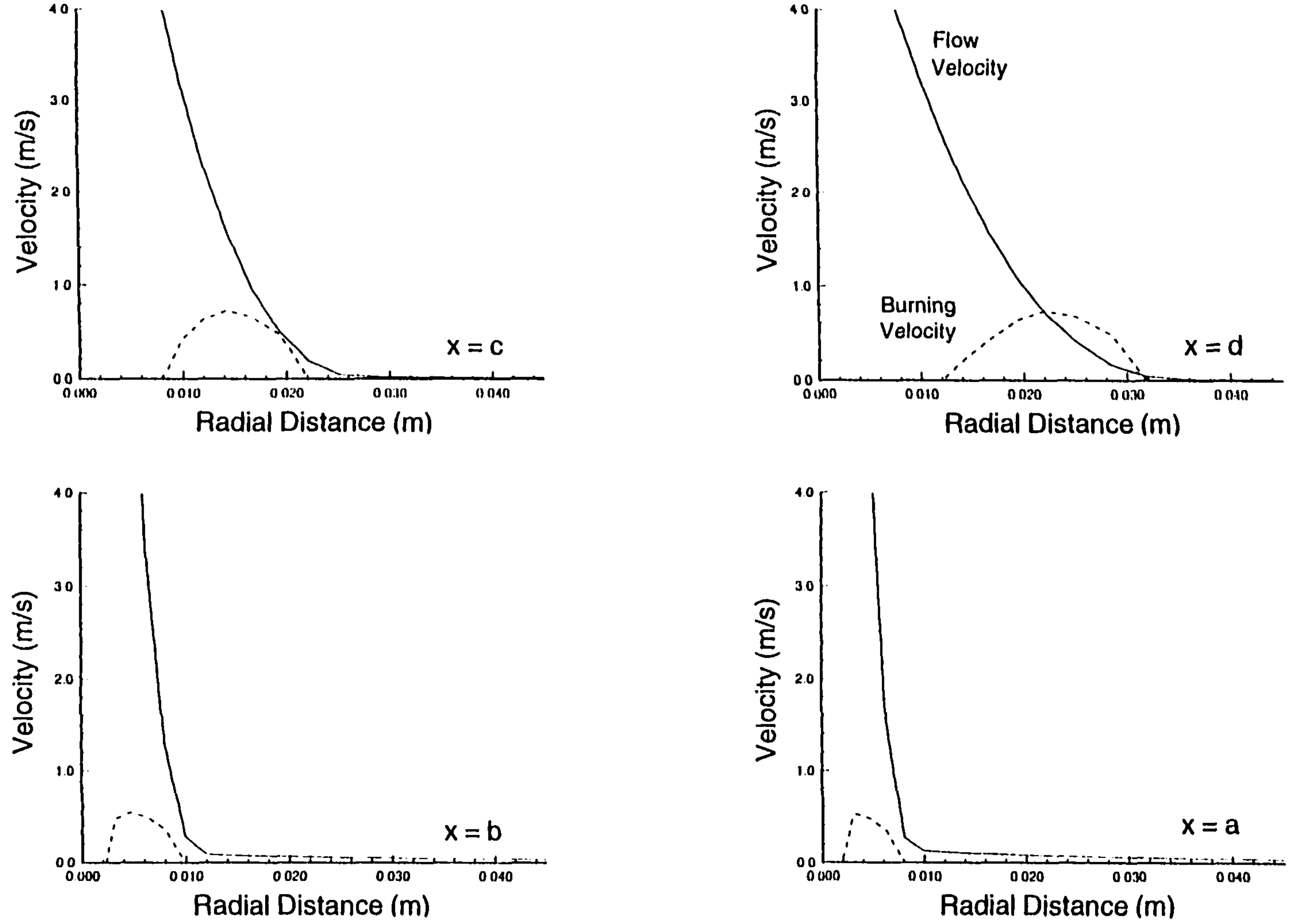

Fig. 4.38 Velocity profiles at different axial locations (a=0.022m, b=0.034m, c=0.049m & d=0.06m) for an isothermal flow and jet exit velocity of 34.7 m/s.

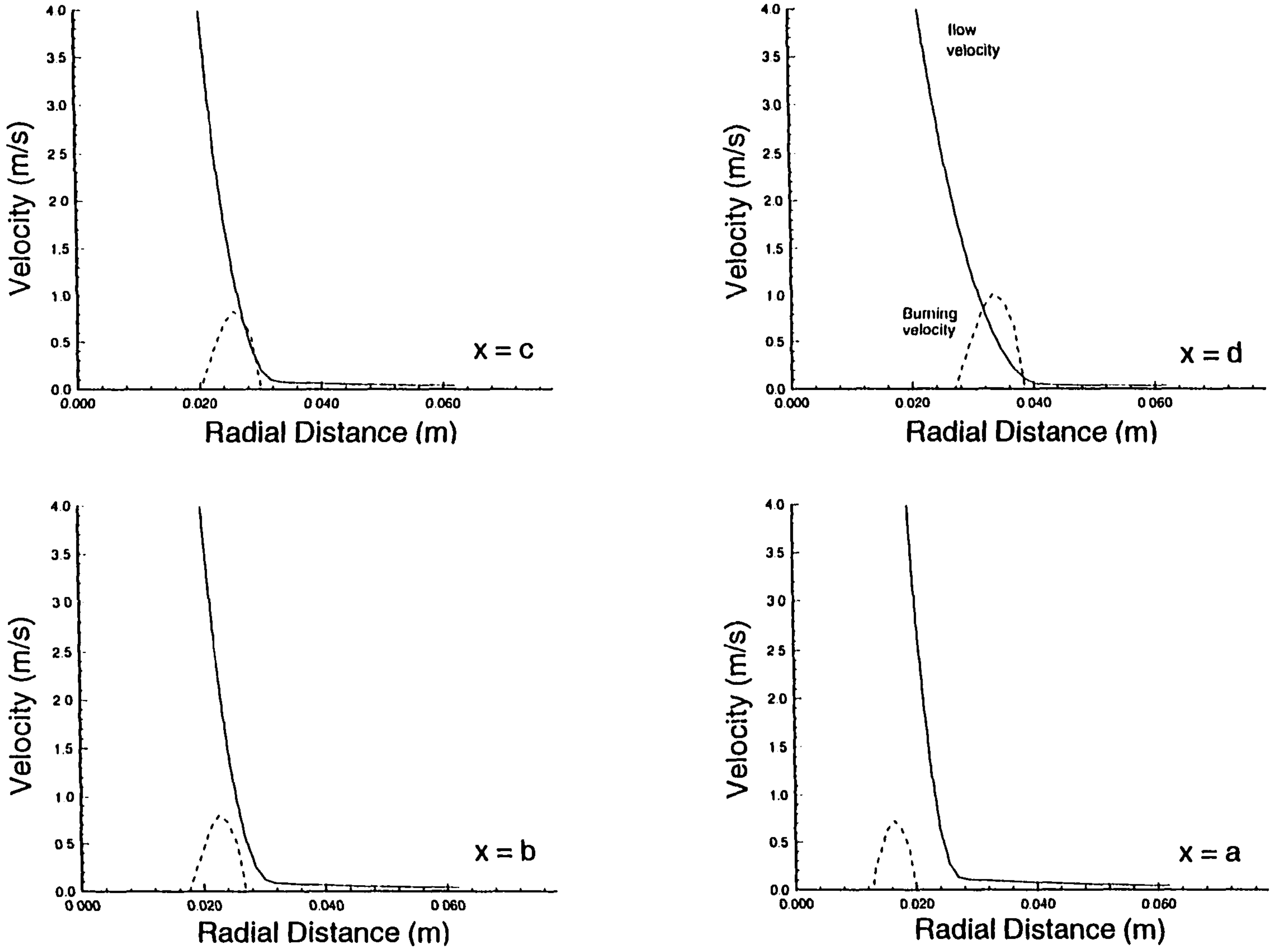

Fig. 4.39 Velocity profiles at different axial locations (a=0.059m, b=.066m, c=0.098m & d=0.135m) for an isothermal flow and jet exit velocity of 62.5 m/s.

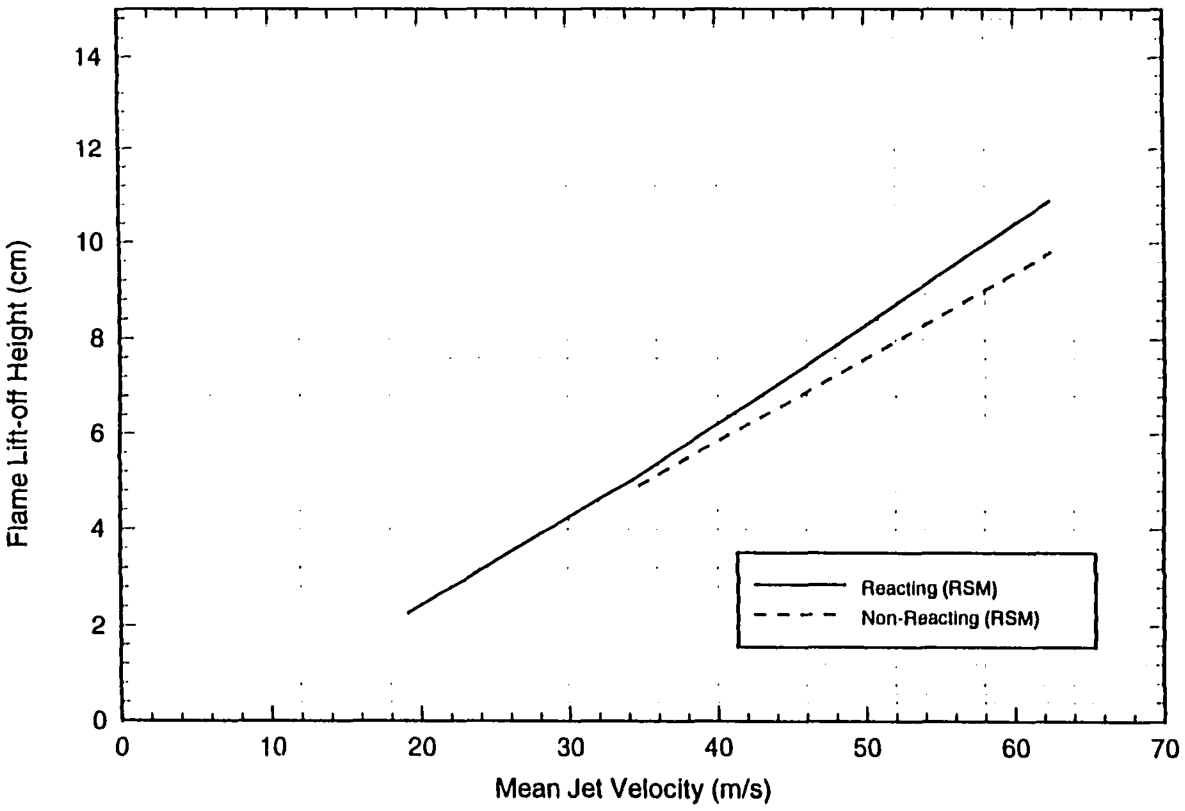

Fig. 4.40 Variation of predicted flame lift-off height with mean exit jet velocity, comparison between non-reacting calculations and reacting calculations.

case for all velocity cases considered in this study. From these results it is evident that the flame base height can be predicted approximately by analyzing the turbulent mixing characteristics of the non-reacting fuel jet. This conclusion is in agreement with the results reported by Pitts [86].

4.5 Comparison of Turbulence Models (Non-Reacting Flow)

All calculations obtained in the previous section are based on eddy dissipation model [33] that is used in conjunction with the Reynolds stress model and the two-step kinetics model. It has been indicated earlier that the k-ϵ model fails to predict the lift-off phenomena in diffusion flames (Fig. 4.12). As demonstrated earlier the flame is stabilized at a location where the mean flow velocity is equal to the turbulent flame velocity. The turbulence flame velocity depends on the accuracy of prediction of the turbulence quantities such as $\overline{u'u'}$ in the flow field, the characteristic turbulence length, and the kinematic viscosity (ν). Figures 4.41 and 4.42 show the comparison of predicted u-component of velocity and k values for the k-ϵ model and the RSM for the non-reacting case. These two figures show that the predicted results from both turbulence models are different near the axial region. This may account for different results for the turbulent flame speed in the two models. Figure 4.43 shows the radial profiles of calculated turbulent flame velocity and the axial component flow velocity for both turbulence models. It is indicated that the turbulent flame speed profile for the case of k-ϵ model reaches the tangency condition with the flow velocity at locations much closer to the injection point than that with the RSM case. In Fig. 4.43, the RSM does not predict tangency condition at all since the axial location is so closed to the injection point. For

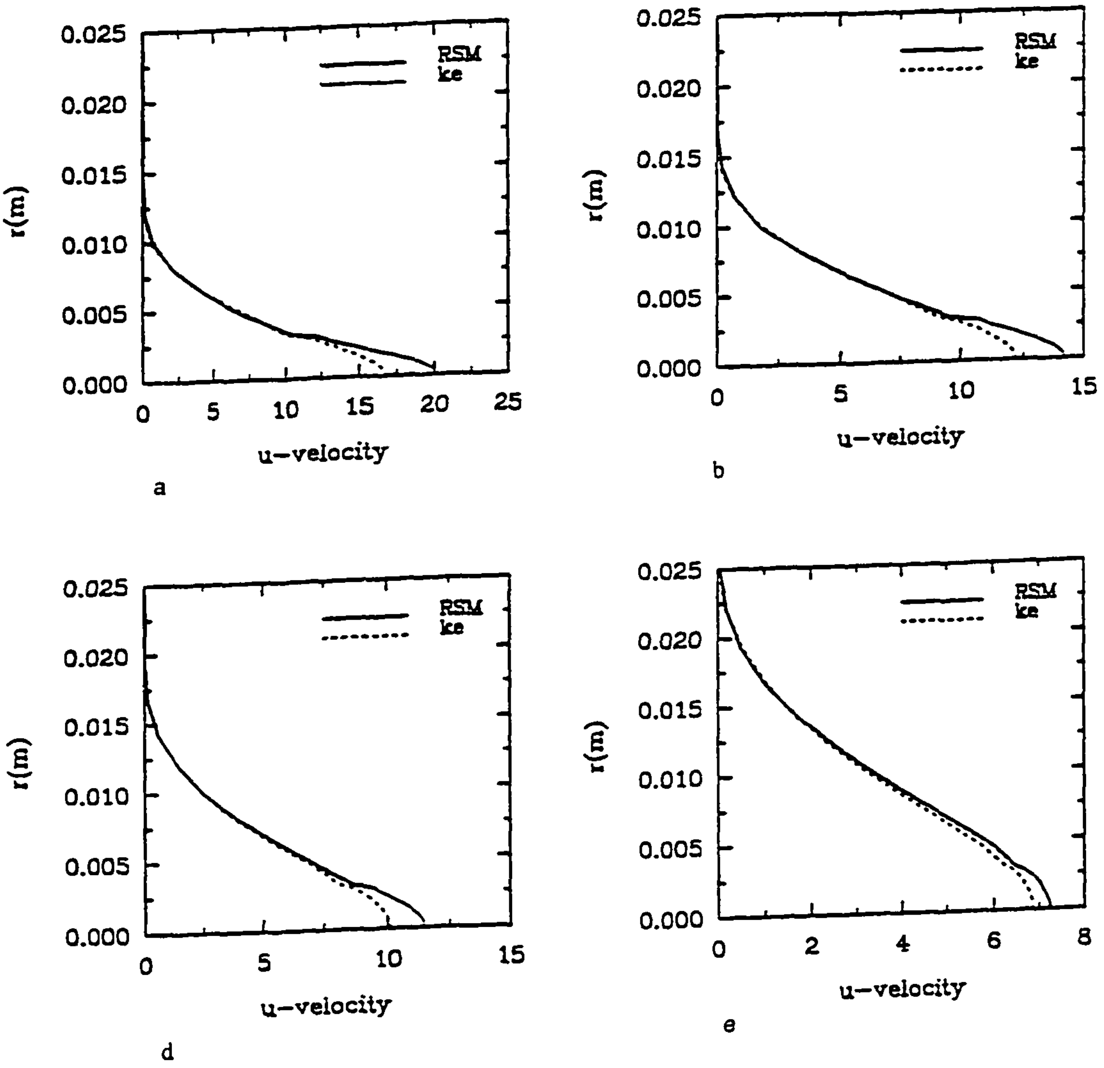

Fig. 4.41 Radial variation of u-velocity at different axial locations using the k-ε and the RSM. (a=1.5cm, b=3.4cm, d=4.8cm & e=6.2cm)

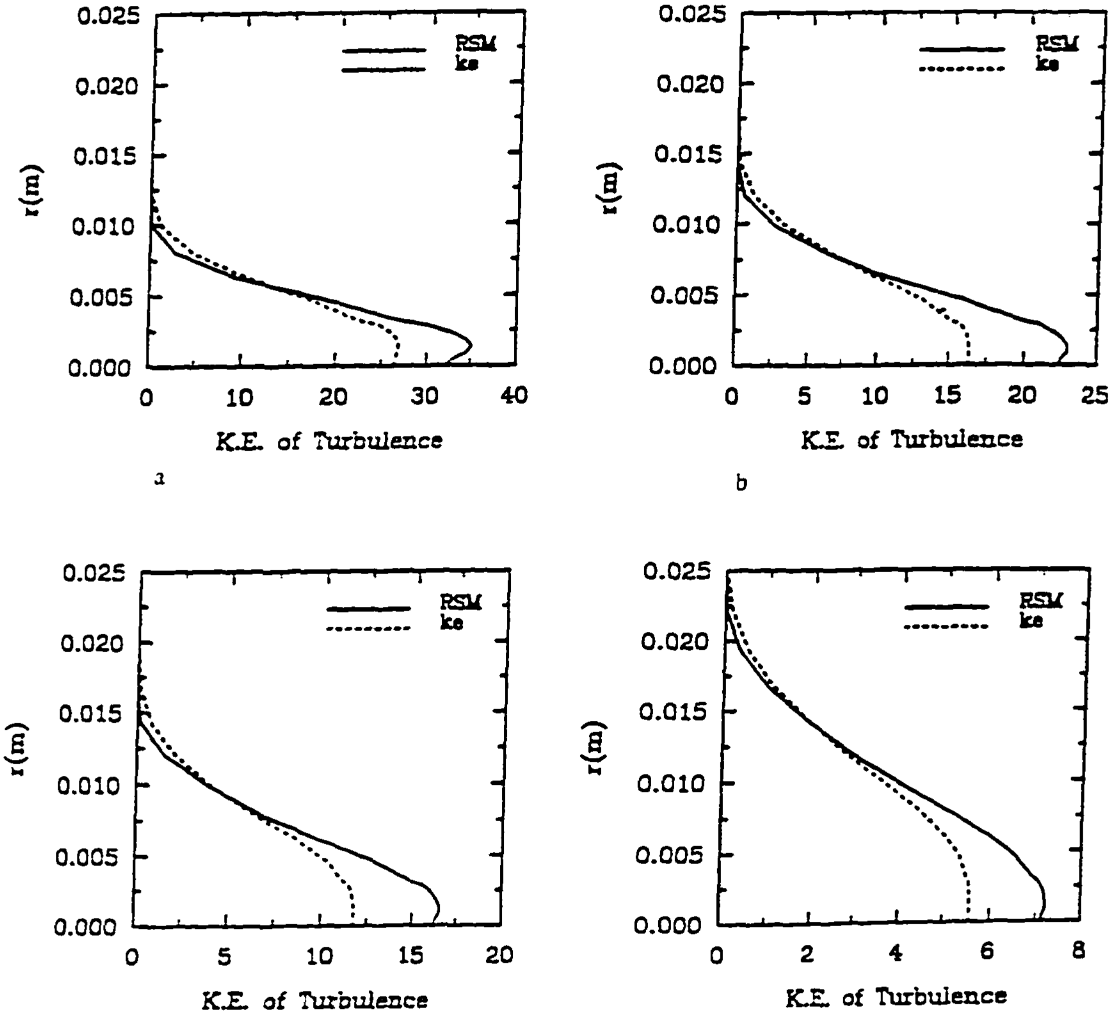

a

b

d

e

Fig. 4.42 Radial variation of K.E. of turbulence at different axial locations using the k-ε and the RSM. (a=1.5cm, b=3.4cm, d=4.8cm & e=6.2cm)

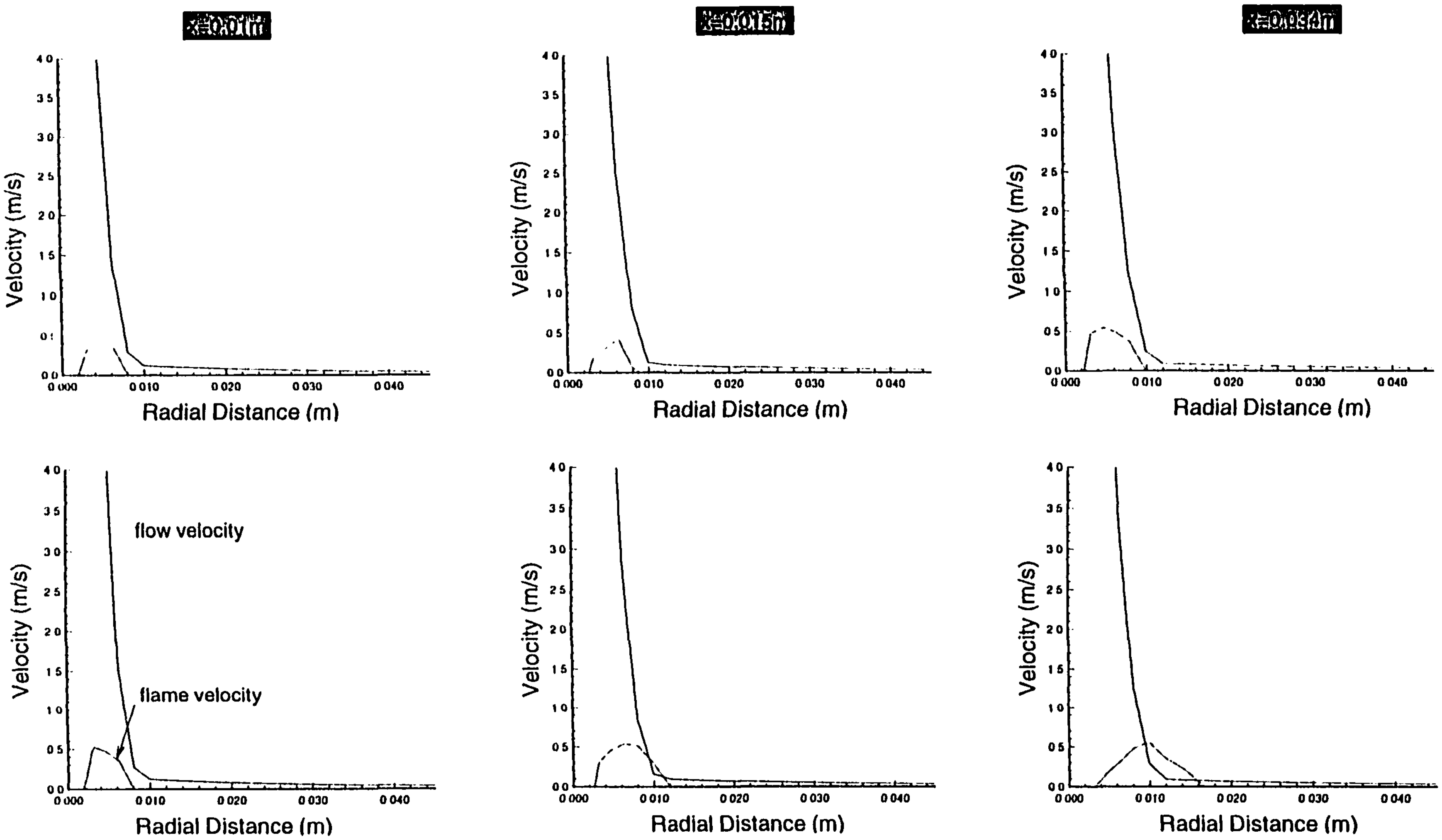

Fig. 4.43 Radial prediction of flame velocity at different axial locations resulted from RSM model (upper row) and k-ε model (lower row) for jet exit velocity of 34.5 m/s (non-reacting).

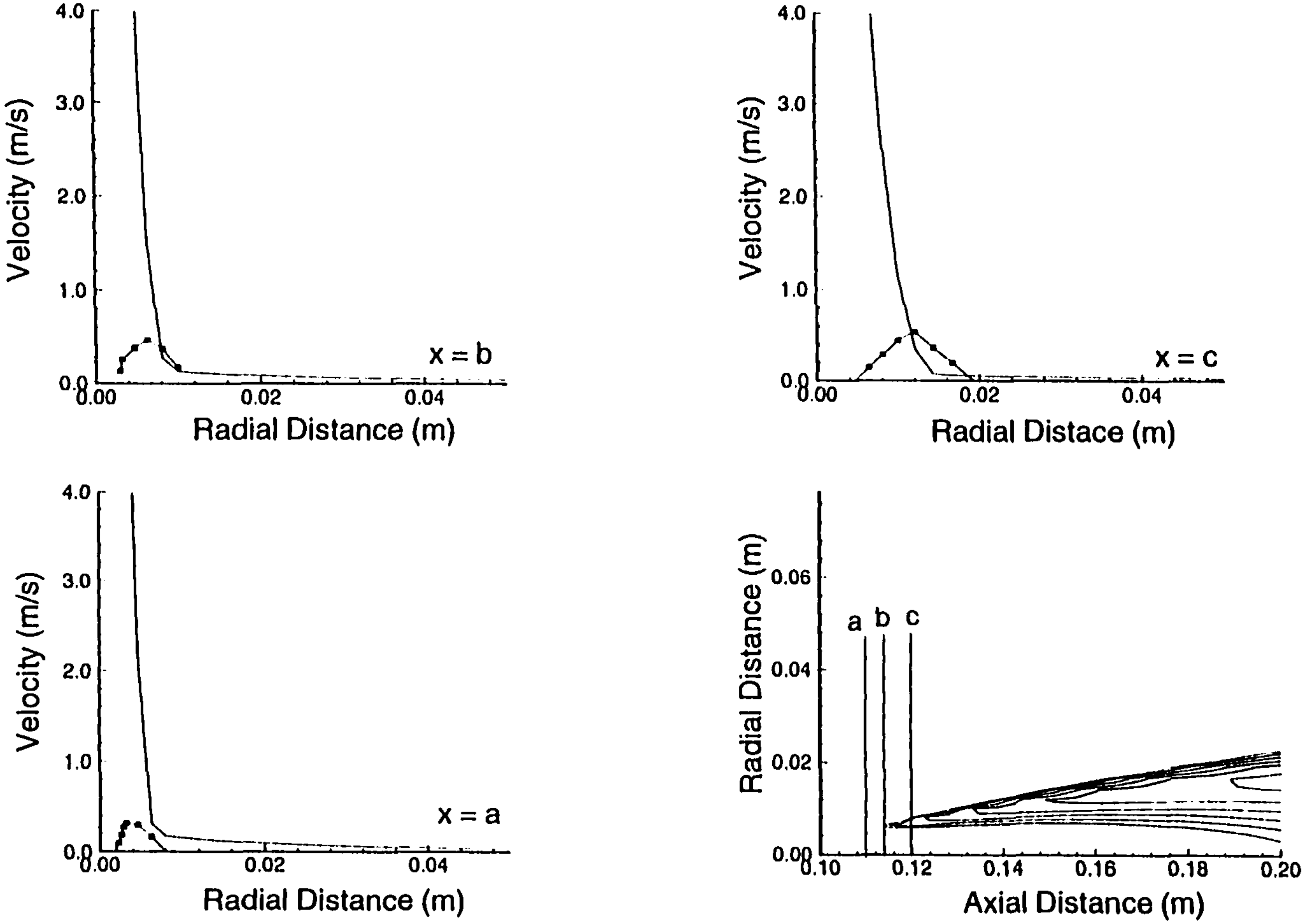

Fig. 4.44 Velocity profiles at different axial locations (a=.01m, b=.015m & c=.021m) for a fuel jet exit velocity of 34.7 m/s. —— flow velocity, ■ turbulent burning velocity (Results from k-ε model)

the reacting case, the predicted flame base location for the k-ϵ model is also underestimated as shown in Fig. 4.44. As noted earlier the flame base height of 0.015 m from the k-ϵ model compares very unfavorably with the value of 0.051 from the RSM.

Comparison of the RSM and the k-ϵ Model (Reacting Flow)

Extensive comparison of the two turbulence models with regard to their capability for predicting the axial variations of turbulent parameters (k, ϵ, μ_{eff}) and temperature is shown in Fig. 4.45. The two models show different results in the near field region. However, in the far field region ($x > 0.25\ m$), both models predict similar results. This is further seen in Fig. 4.46, where the radial profile of predicted temperature from the k-ϵ model is compared favorably with the results predicted from the RSM at an axial location of 0.23 m from the injection point.

The effect of inlet turbulence intensity on the flame structure is demonstrated in Fig. 4.47. All computations were performed with inlet turbulence intensity of 9%. It can be seen from Fig. 4.47 that the inlet intensity does not have a significant effect on the lift-off phenomena. However, calculations with the inlet turbulence intensity of 15% showed that increasing the intensity results in thinning of the flame base.

Effect of Kinetics Model

The source terms in the energy and mass transport equations depend on the reaction rate which in turn depends on whether the reaction is kinetically or diffusion controlled. In kinetically controlled regime, the reaction rate is computed from the Arrehenius expression which depends on the kinetic models. Figure 4.48 shows the comparison of flame structure for one-step and two-step reaction models. It is evident that

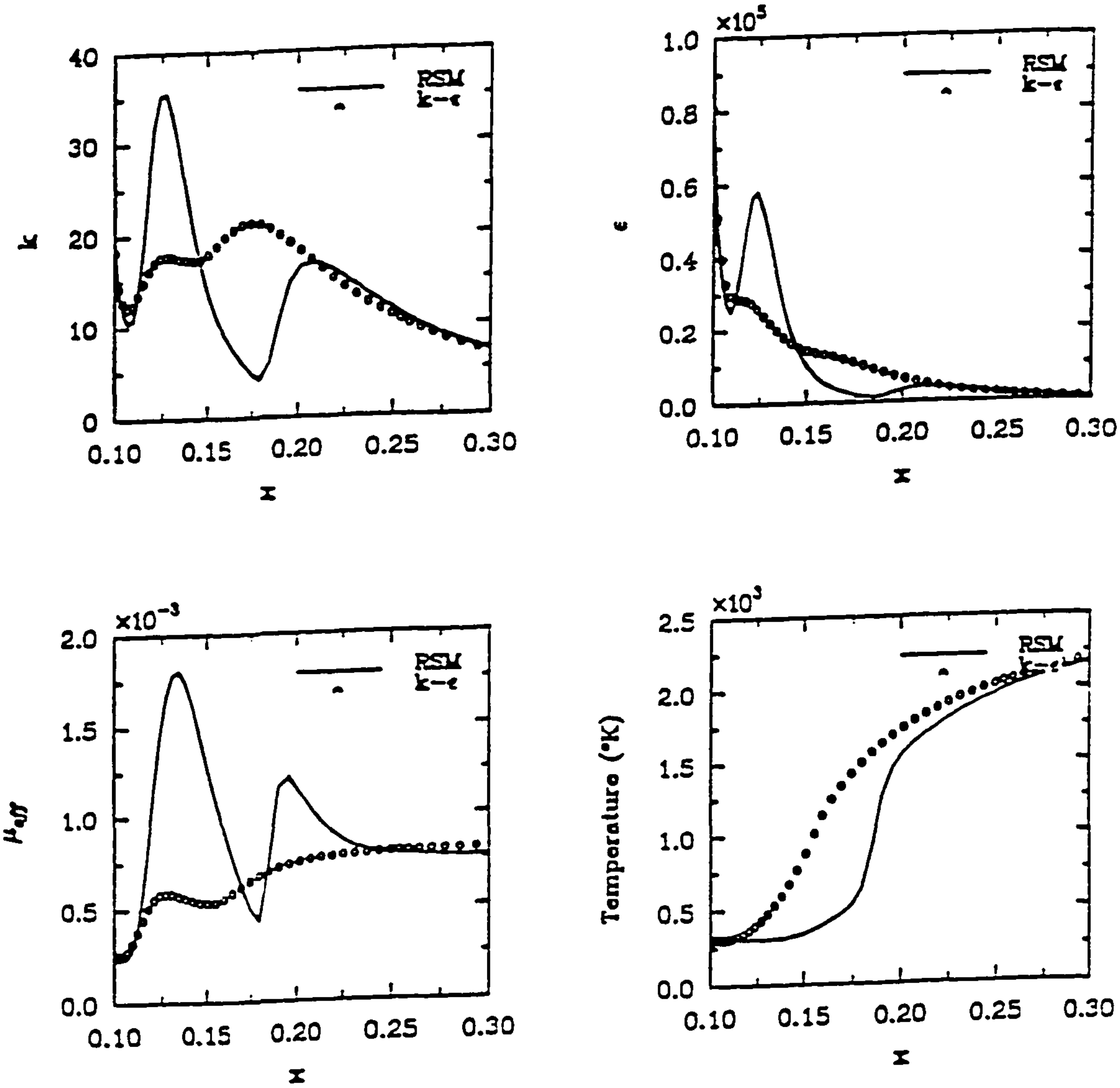

Fig. 4.45 Results of two turbulence models along the axis (reacting).

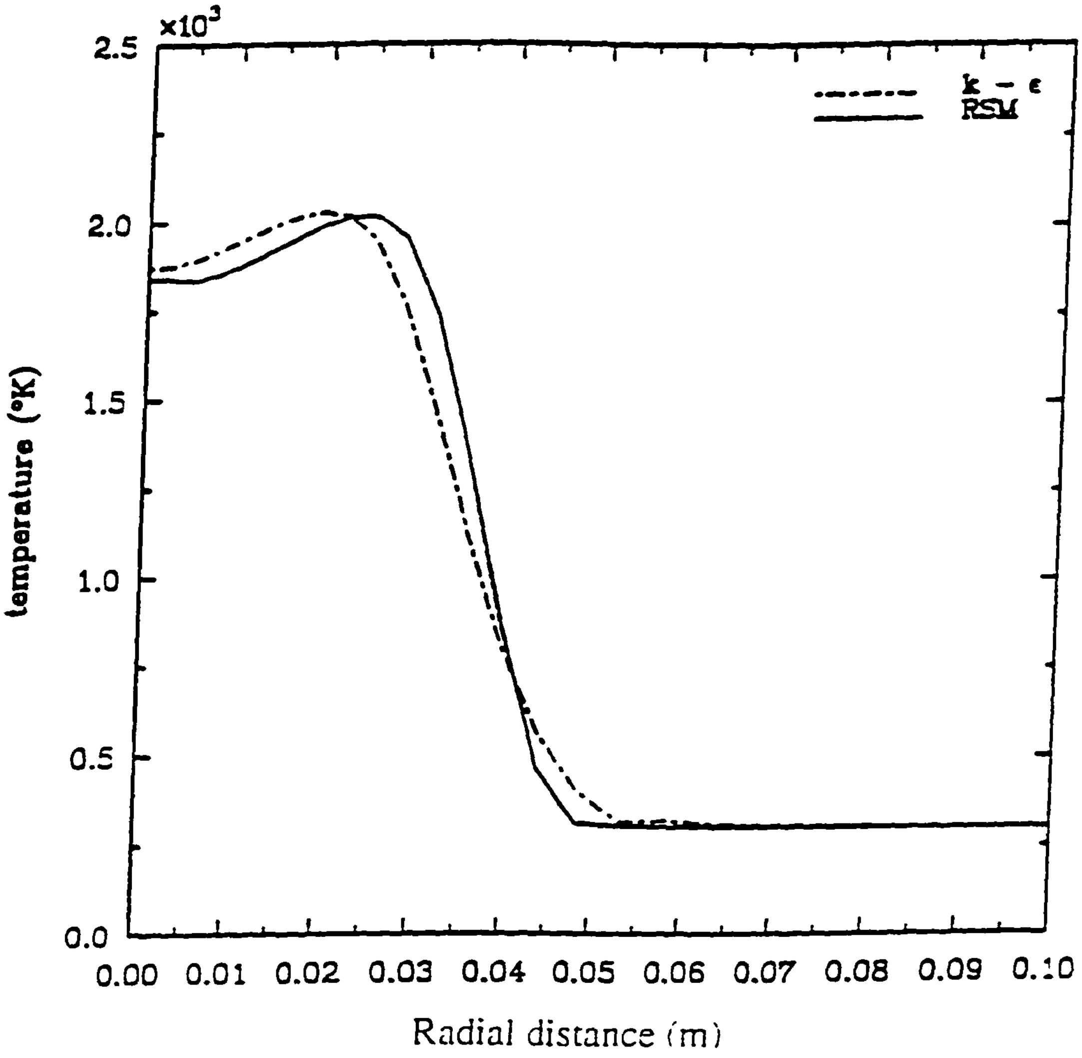

Fig. 4.46 Comparison of two turbulence models at 23 cm from the injection point.

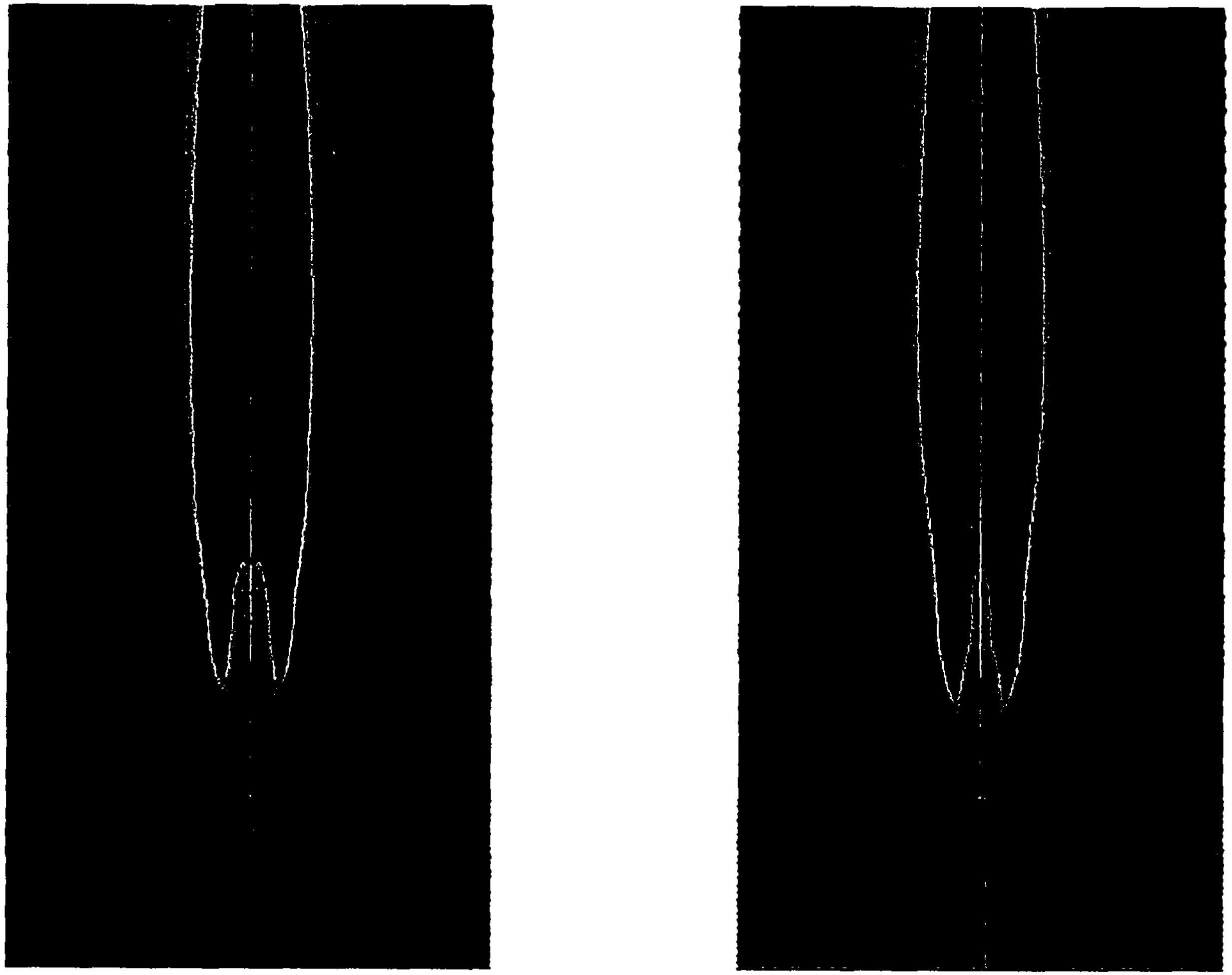

I = 9% (Present)

I =15%

Fig. 4.47 Effect of turbulence intensity on the flame structure.

the one-step model under-predicts the flame lift-off height by about 30% as compared to the two step model. This has also been observed in Ref. 66 which also showed the comparison of one-step and two-step models.

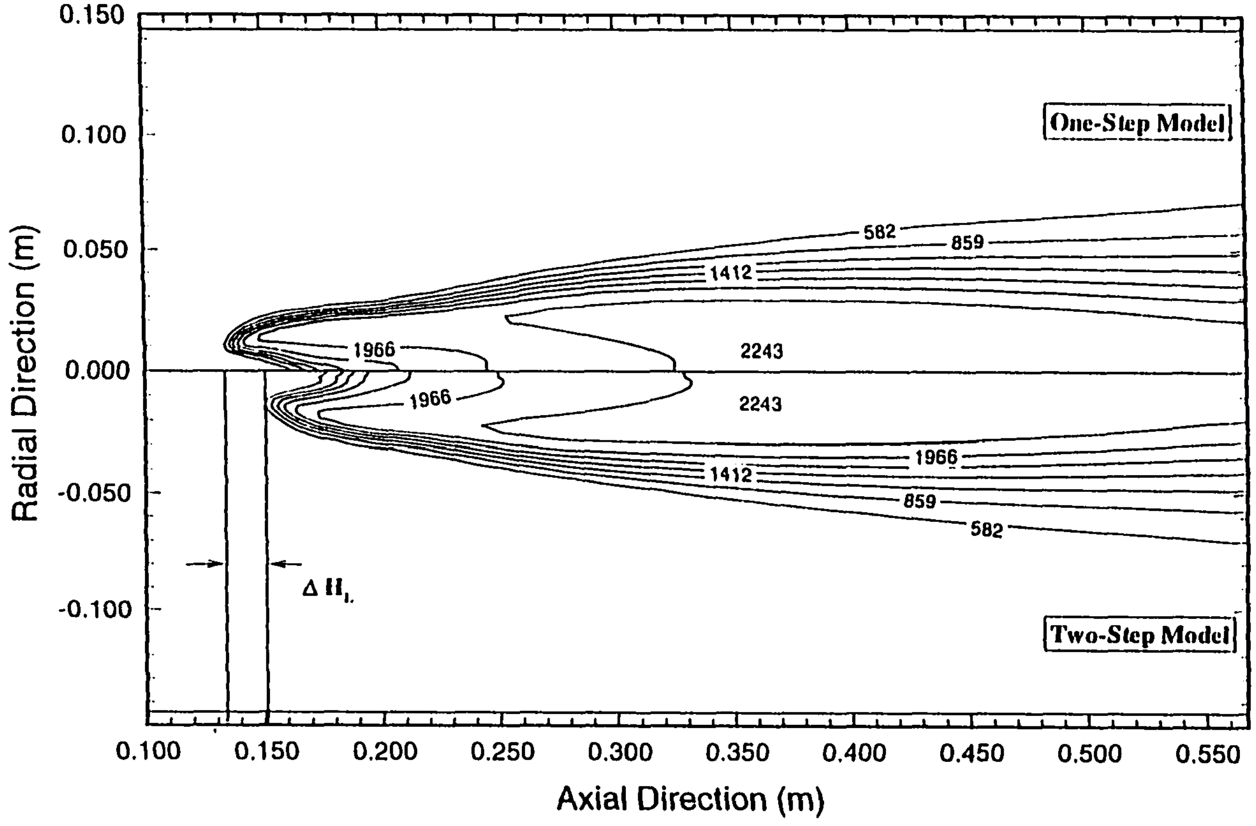

Fig. 4.48 Effect of chemical kinetics on the flame structure predicted by (RSM) model for a fuel jet exit velocity of 34.7 m/s.

Chapter 5

CONSIDERATION OF VARIOUS FUEL TYPES AND GEOMETRY

The structure of the base region of a lifted turbulent flame has been discussed for methane in the preceding chapter. In Chap. 4, results for methane fuel injector showed that calculations were in good agreement with the hypothesis suggested by Vanquickenbourn and van Tiggelen [3] concerning the existence of a premixed region near the flame base. This chapter examines the validity of the hypothesis regarding the flame stabilization for propane and methane-hydrogen mixtures. Results for flow involving swirling motion are also presented. Finally, reacting flow results also are obtained from the PDF/flame sheet model.

5.1 Results for Propane Injector

The computations of propane flames are compared with experimental results by Annushkin and Sverdlov [5], Kalaghatgi [7], and Chen and Kollman [87]. The geometric configuration is identical to the one considered in the previous chapter. The eddy dissipation model in conjunction with the RSM model has been used to determine the turbulent flame structure. The only modeling difference between methane and propane calculations is that in the former we have used a two-step kinetics while in the latter a one-step kinetics model is used. This is primarily due to unavailability of a two-step kinetics model for propane in the literature that is compatible with the FLUENT code requirements. Before presenting detailed results, the grid sensitivity of results was analyzed and the results are summarized in Fig. 5.1 which includes axial and radial profiles of temperature and velocity. From this figure, it is clear that the choice of 155x61 grid size is adequate for this study.

Figures 5.2 and 5.3 show the calculated temperature field for propane for the jet exit velocity ranging from 20 m/s to 60 m/s. It can be observed that the structure of the flame is strongly governed by the jet exit velocity. As the jet velocity increases, the flame width and base height are increased. Propane results for 34.7 m/s jet velocity are compared with the results obtained from the corresponding methane fuel jet in Fig. 5.4, which shows the oxygen concentration field for methane and propane cases. For propane which is heavier than air, the jet shear layer contains finer structure and the propane jet expands less rapidly compared to the methane jet in the near flow field. It is also noted that the propane case shows small scale perturbations in the flame outer profile. In contrast the methane flame profile is much smoother.

Figure 5.5 presents the predicted centerline profiles for the mean propane concentration along with the experimental data and numerical results of Chen and Kollmann [87]. The corresponding comparison of radial profiles at 40 and 80 diameters downstream are shown in Fig. 5.6. From these comparisons one observes that the present results compare reasonably with the experimental results for the propane flame. In fact, the present calculations showed better comparison with experimental results than the ones predicted by the PDF model at axial locations greater than 50 diameter. Figure 5.7 shows the radial variation of mixture fraction. These results are compared with results of Chen and Kollmann. However, concentration of CO_2 is overpredicted as compared to the experimental data, especially at 40 diameter downstream of the injection point (Fig. 5.8).

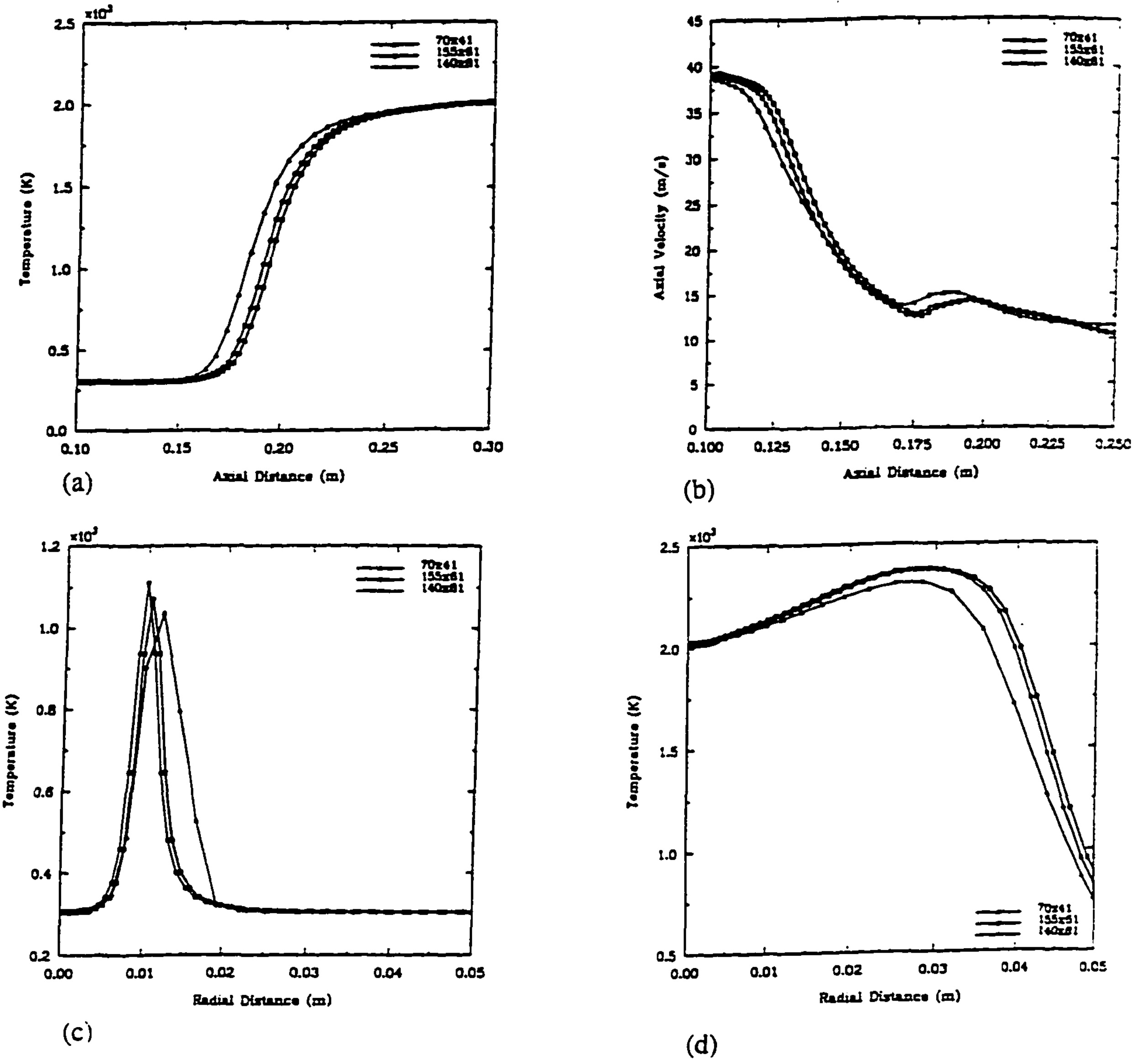

(a) (b) (c) (d)

Fig. 5.1 Effect of grid size on prediction of (a) axial temperature distribution, (b) axial velocity distribution, (c) radial temperature profile at x=4.84 cm and (d) radial temperature profile at x=23 cm.

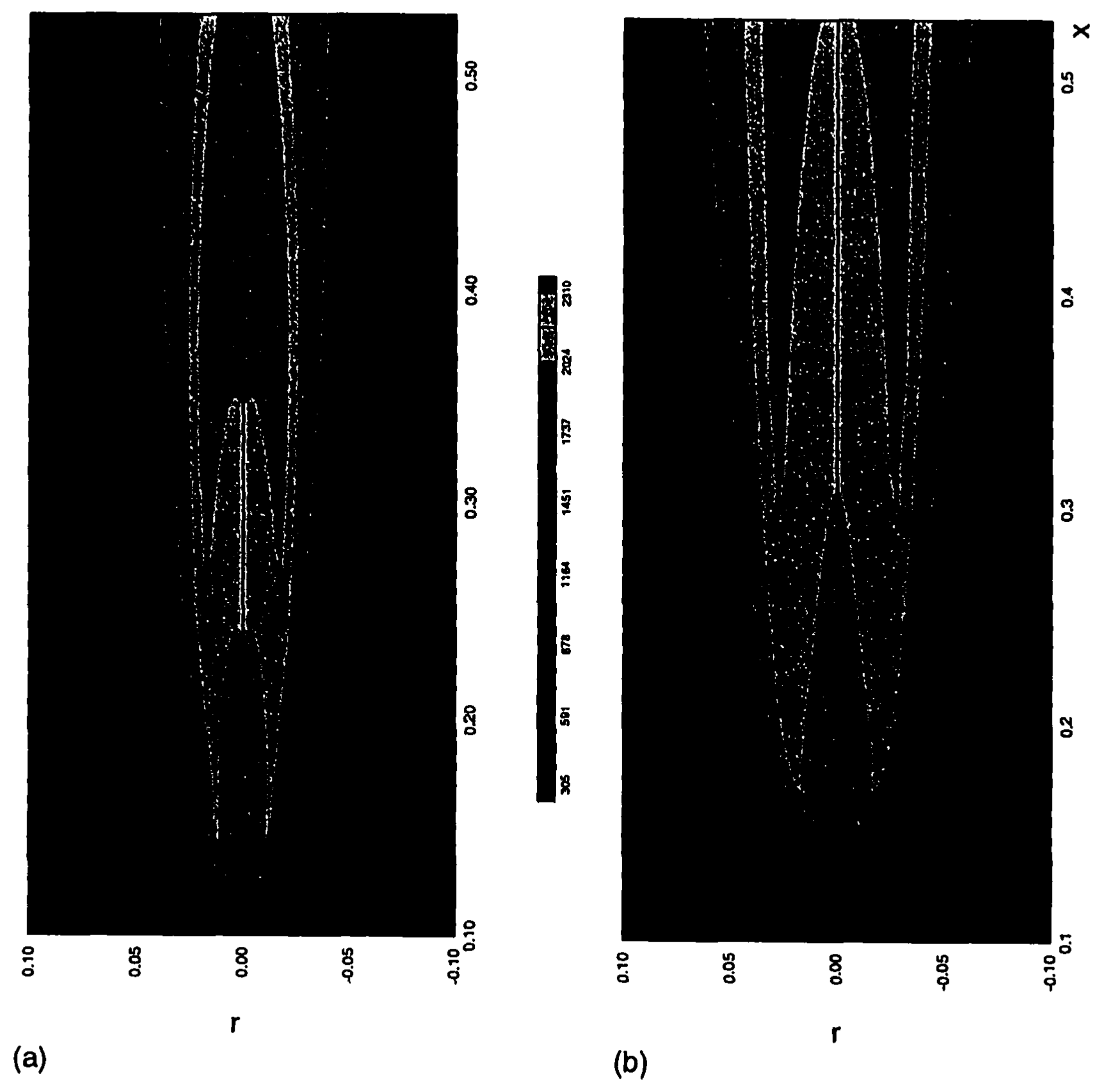

(a) (b)

Fig. 5.2 Predicted temperature field for flames exit velocity of (a) 20 m/s and (b) 34.7 m/s.

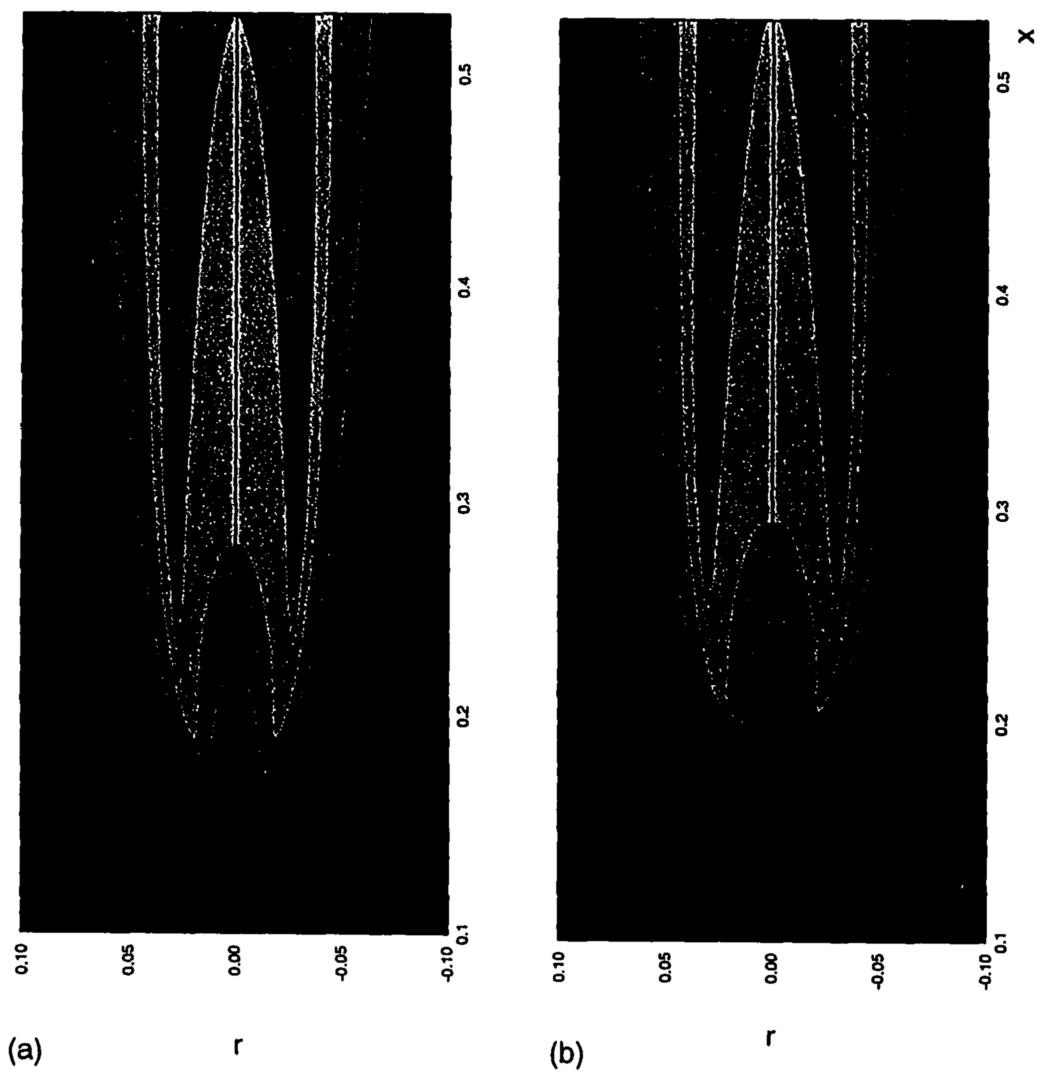

Fig. 5.3 Predicted temperature field for flames exit velocity of (a) 47.5 m/s and (b) 60.0 m/s.

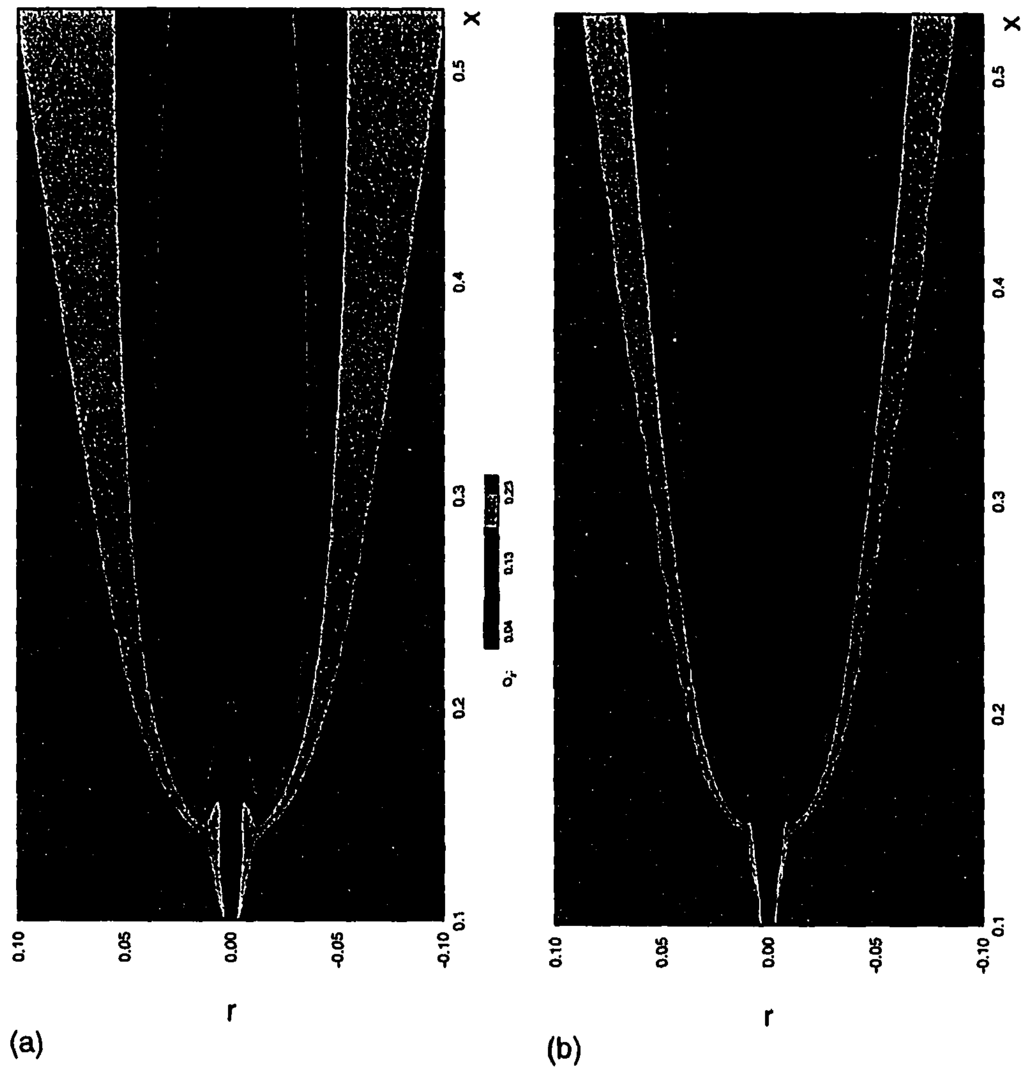

Fig. 5.4 Prediction of oxygen field for jet exit velocity of 34.7 m/s (a) methane flame and (b) propane flame.

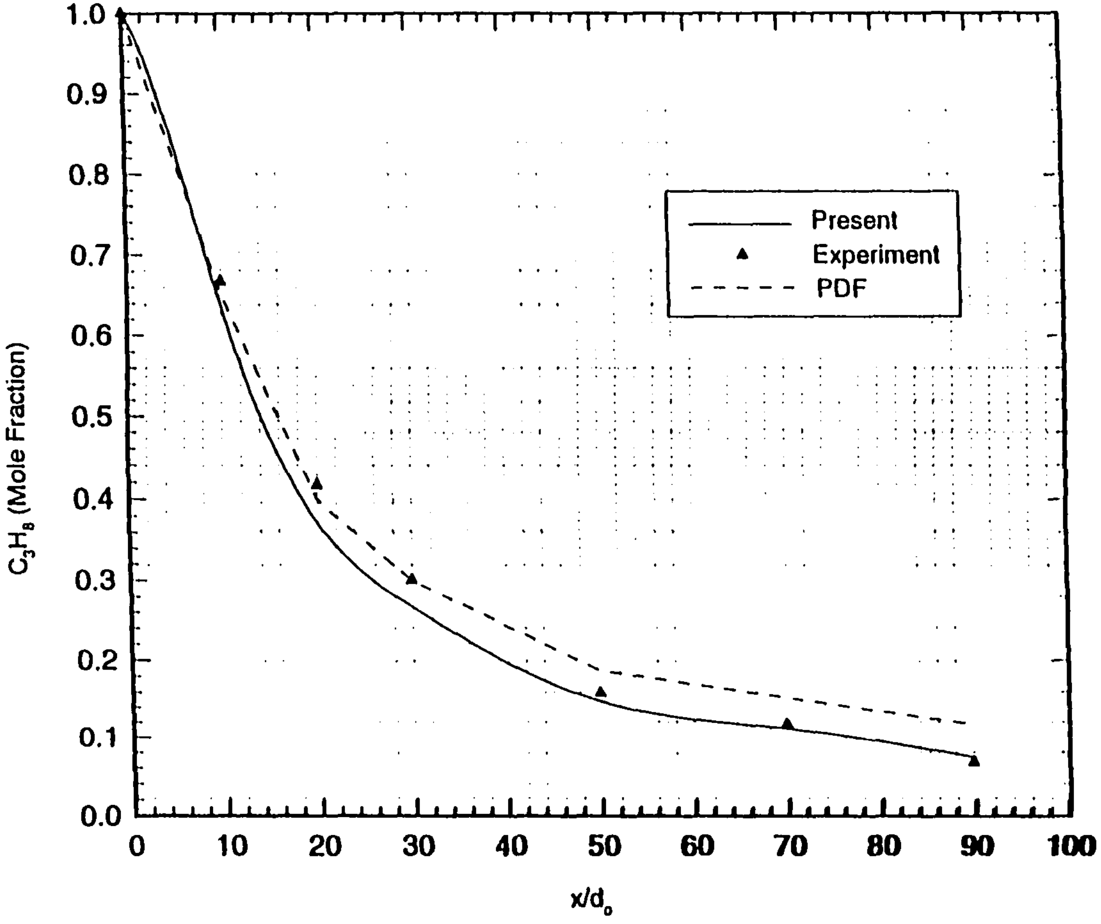

Fig. 5.5 Prediction of propane mole fraction along the center axis and comparison with experimental and PDF results from Chen and Kollmann.

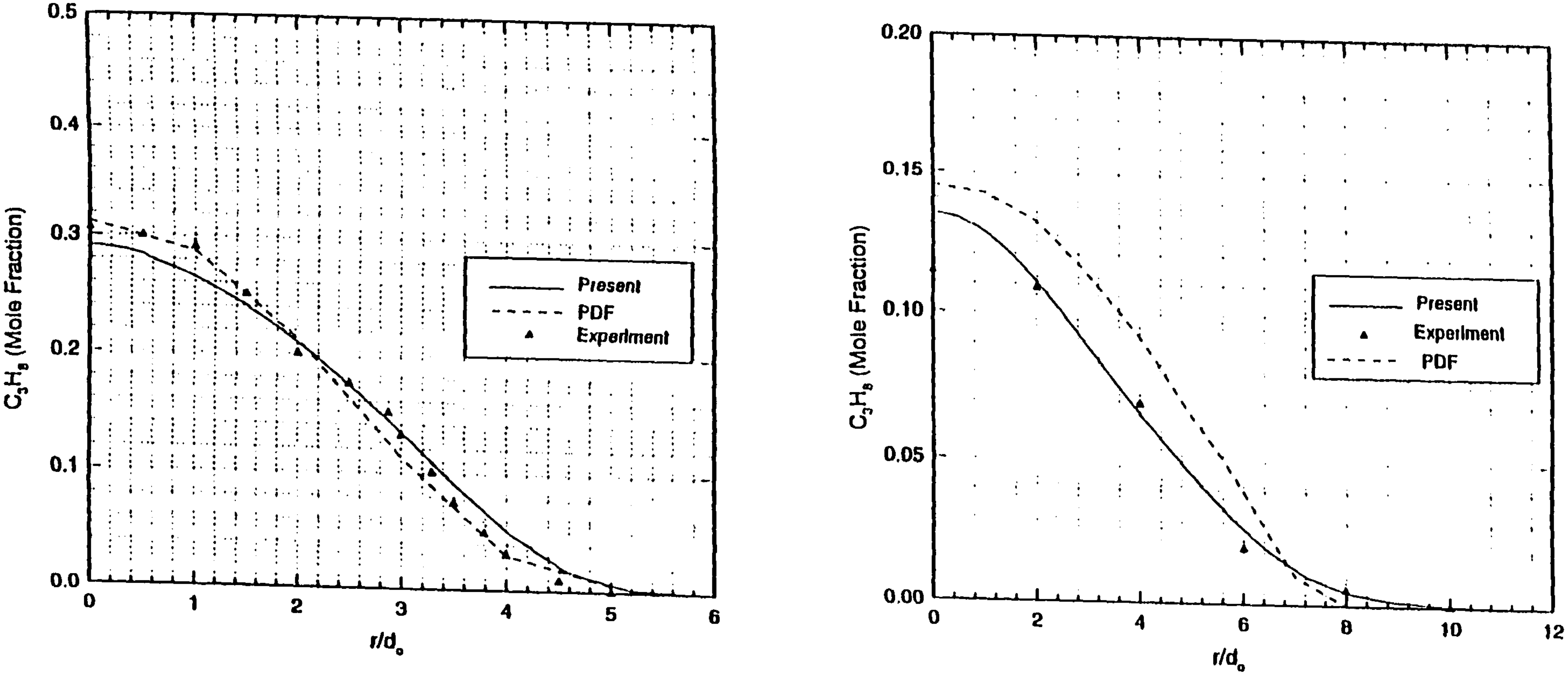

$\frac{x}{d} = 40$

$\frac{x}{d} = 80$

Fig. 5.6 Radial profiles of C_3H_8 mole fraction at two axial locations and comparison with experimental and PDF results from Chen and Kollmann.

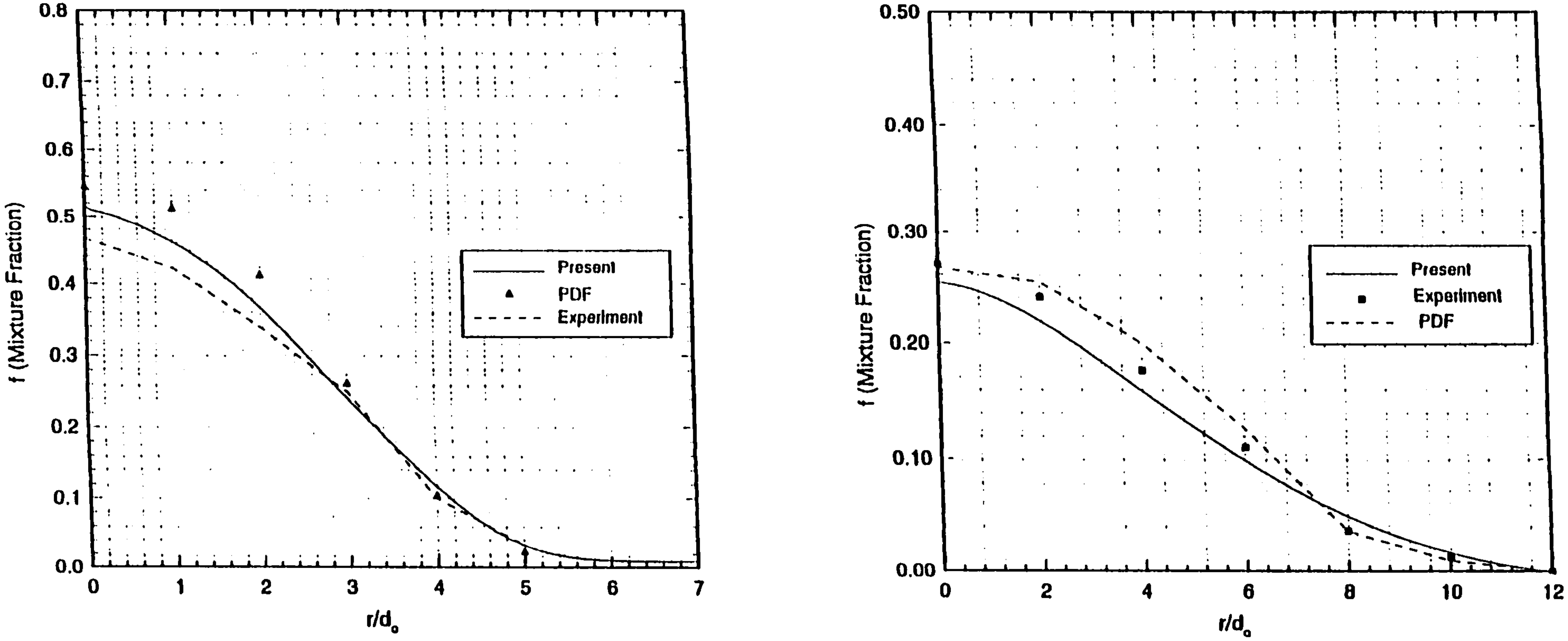

$\frac{x}{d} = 40$

$\frac{x}{d} = 80$

Fig. 5.7 Radial profiles of mixture fraction at two axial locations and comparison with experimental and PDF results from Chen and Kollmann.

It should also be emphasized that the present CO_2 results at a location 80 diameter downstream showed better comparison with the experimental results than those predicted by the PDF model.

Flame Lift-off Results

The criteria used in determination of the flame base have been described in Sec. 4.4. In this section we use the same procedure to locate the axial and radial positions of the flame base. Figures 5.9-5.11 present the radial profiles of calculated turbulent flame velocity and the axial component of flow velocity for jet velocity of 34.7, 47.5 and 60 m/s, respectively. As noted in the previous chapter the flame is stabilized at a location where the turbulent flame velocity is equal to the flow velocity. This is indicated by the tangency condition in Figs 5.9-5.11. From these figures the axial locations of the flame base are determined. The radial location of the flame base is determined from Figs. 5.12-5.14 for corresponding jet velocities. In these figures the temperature field for the four velocities are overlapped with the mixture fraction contours. From the fact that the flame base is located along the stoichiometry contour, the radial location of flame base is determined from the axial coordinate already determined from Figs. 5.12-5.14. Figure 5.15 shows the variation of the flame base width and the maximum flame width with the jet exit velocity.

Figure 5.16 shows the variation of flame base height to the tube diameter ratio with the jet exit velocity to diameter ratio. As can be seen from the figure, the present calculation overpredicts the results of Annushkin and Sverdlov by about 6 - 9 percent. On the other hand, these results are about 12 percent lower compared to the results of

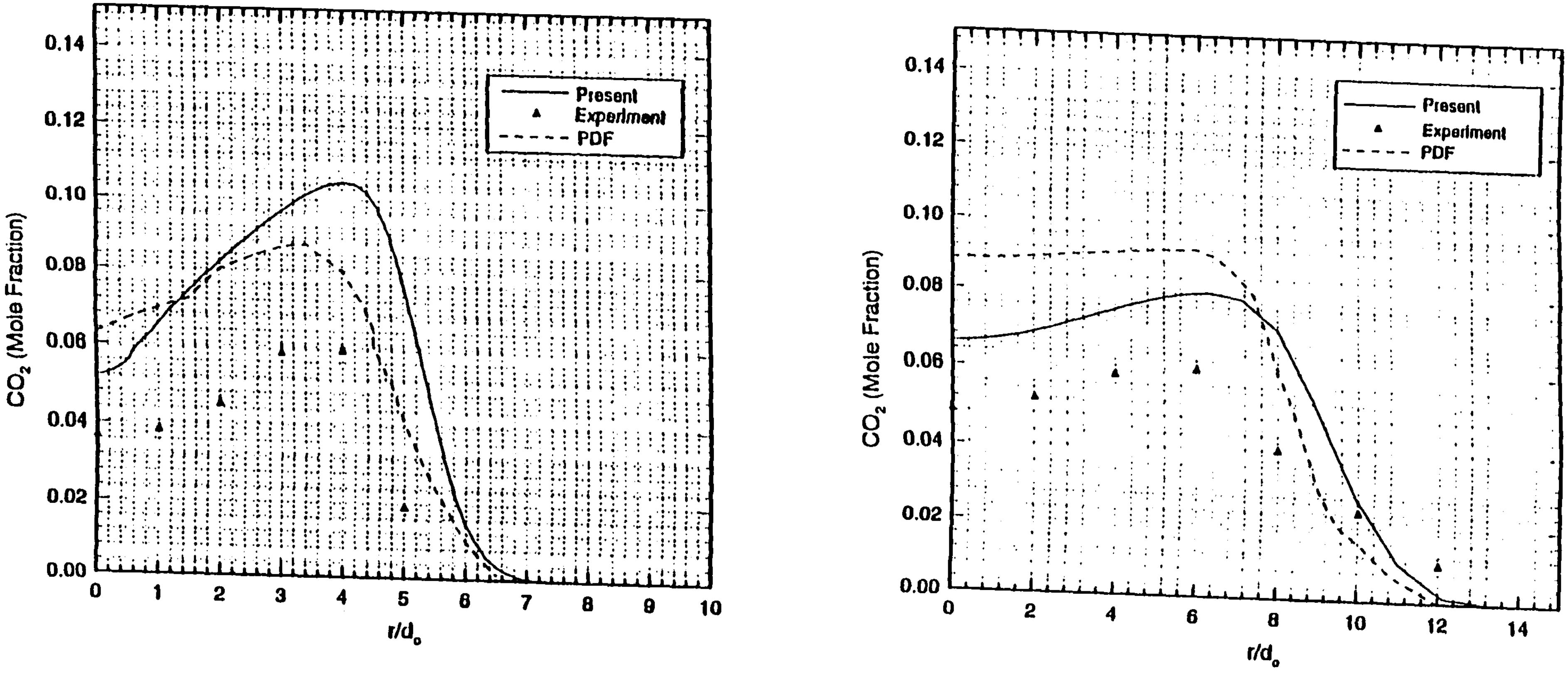

$\frac{x}{d} = 40$

$\frac{x}{d} = 80$

Fig. 5.8 Radial profiles of CO$_2$ mole fraction at two axial locations and comparison with experimental and PDF results from Chen and Kollmann.

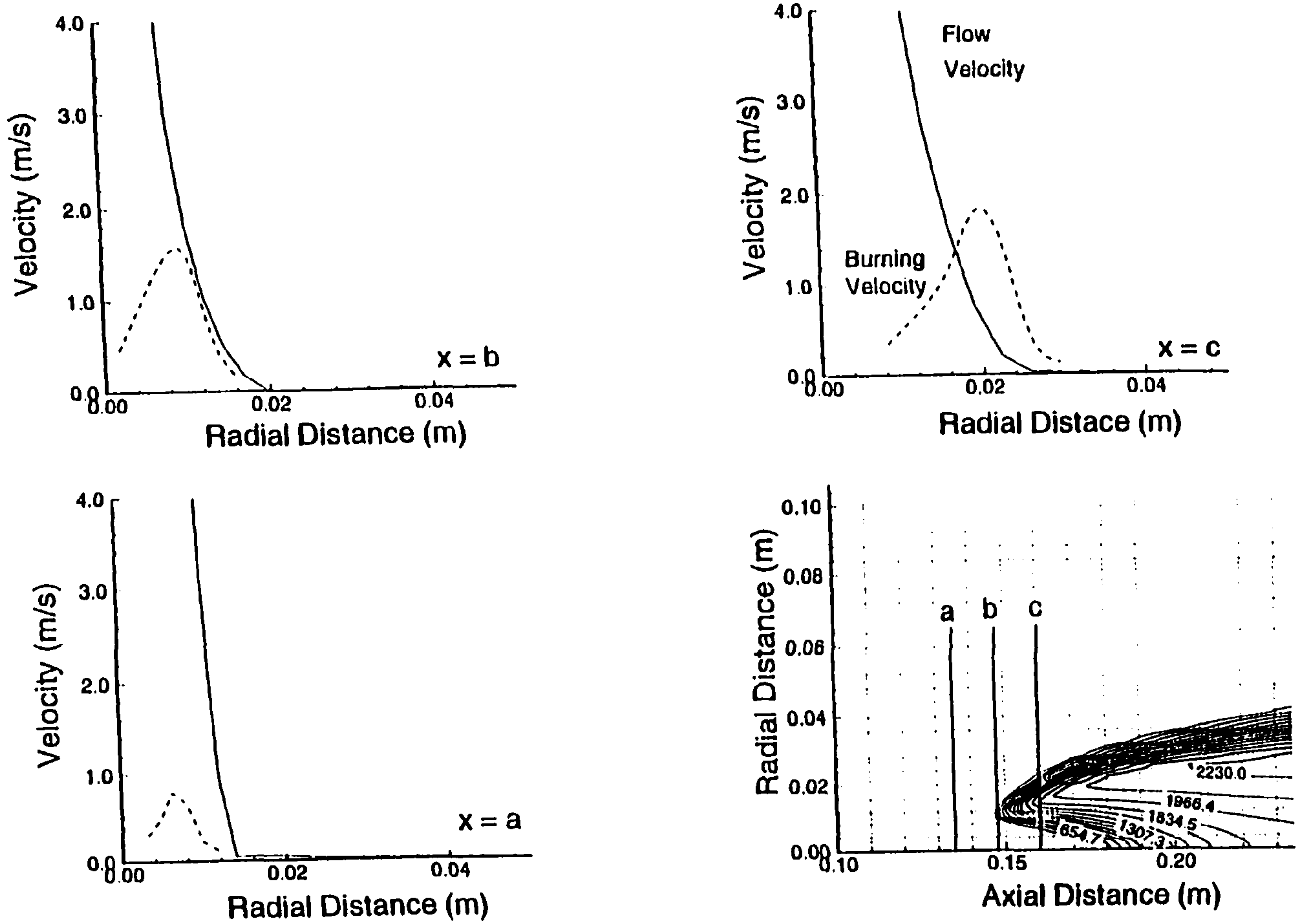

Fig. 5.9 Velocity and turbulent flame speed profiles at different axial locations (a=.035 m, b=.047 m & c=.06 m) for the fuel jet velocity of 34.7 m/s (fuel C_3H_8).

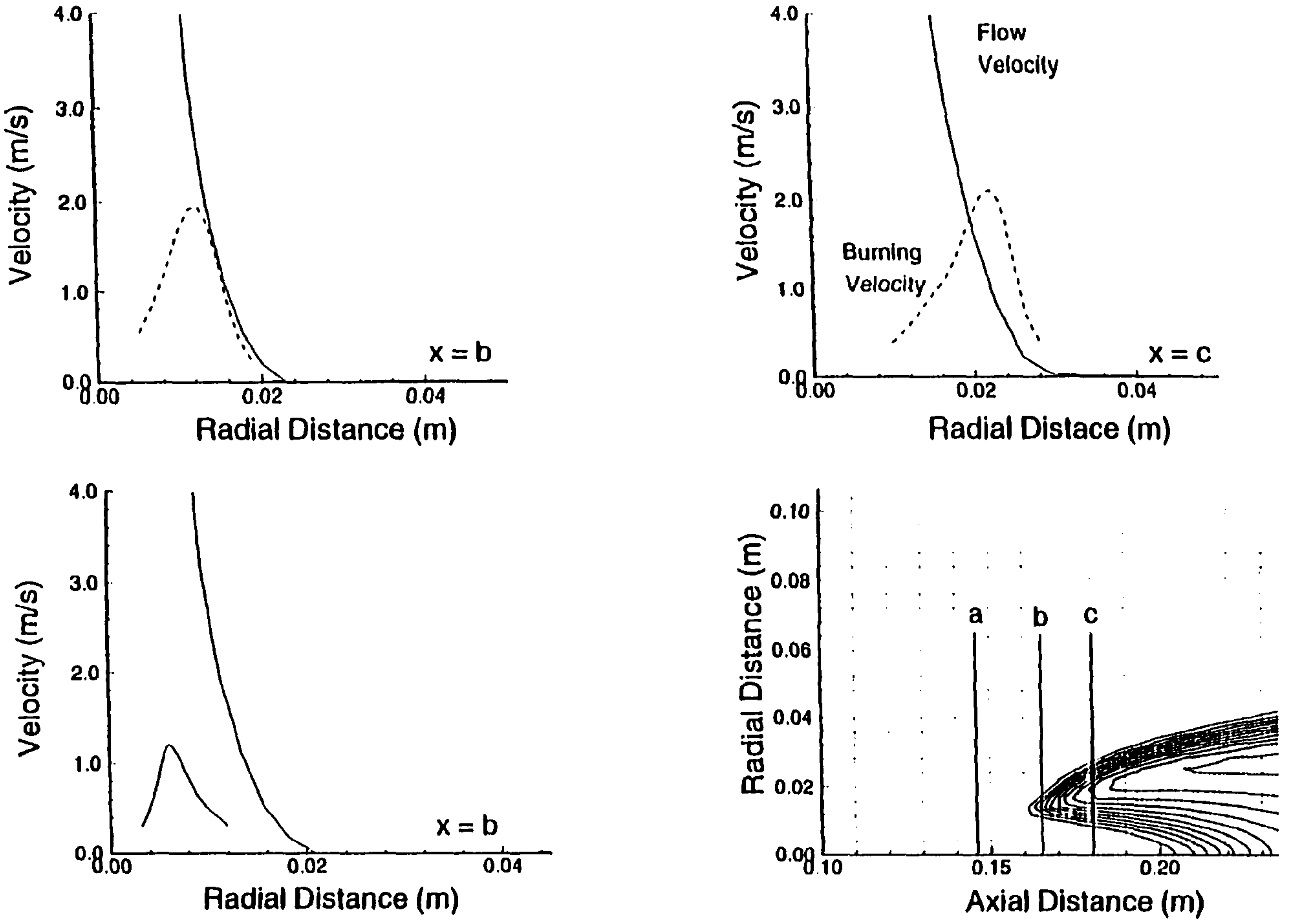

Fig. 5.10 Velocity and turbulent flame speed profiles at different axial locations (a=.047 m, b=.066 m & c=.08 m) for the fuel jet velocity of 47.5 m/s (fuel C_3H_8).

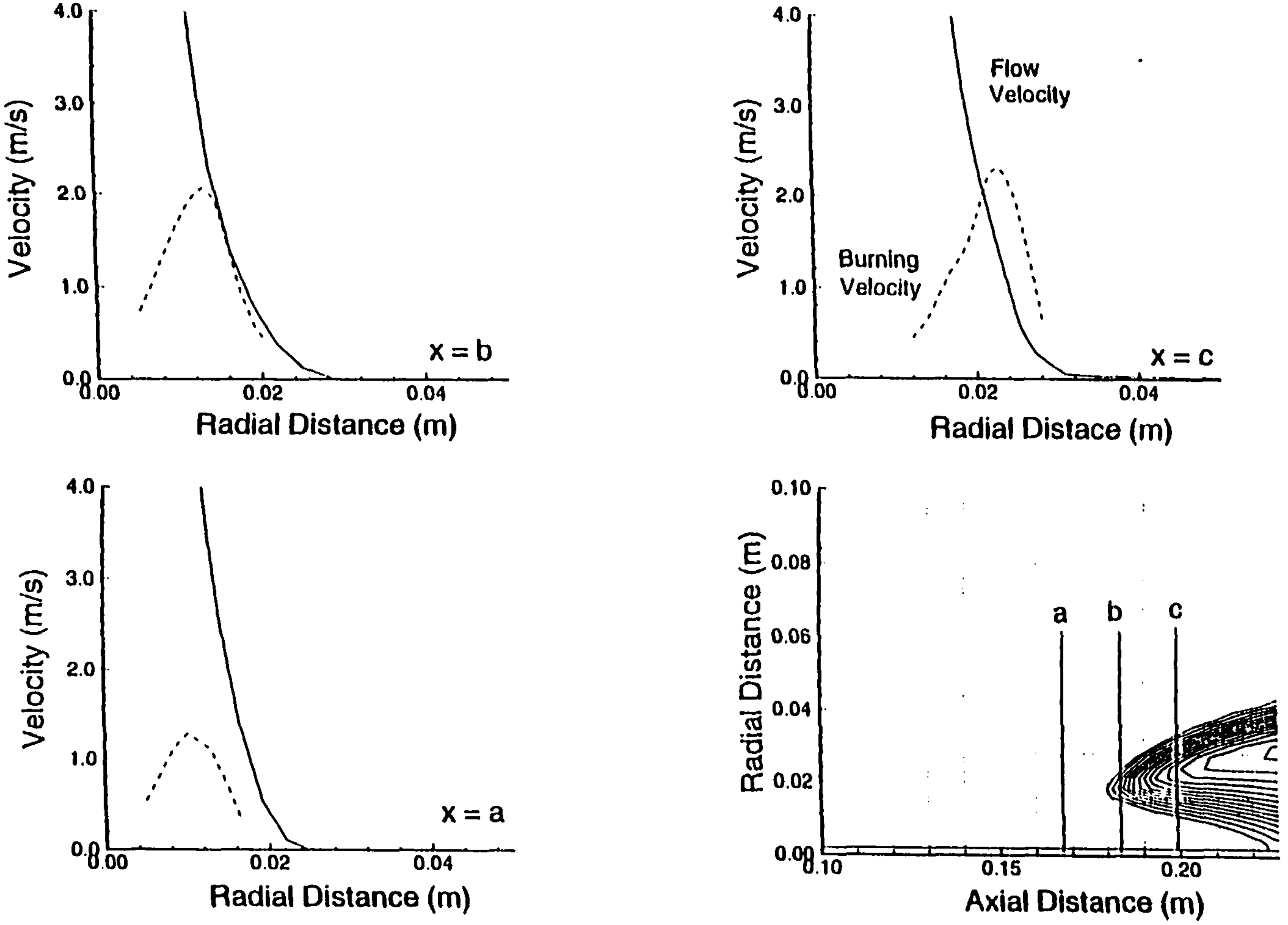

Fig. 5.11 Velocity and turbulent flame speed profiles at different axial locations (a=.078 m, b=.084 m & c=0.1 m) for the fuel jet velocity of 60.0 m/s (fuel C_3H_8).

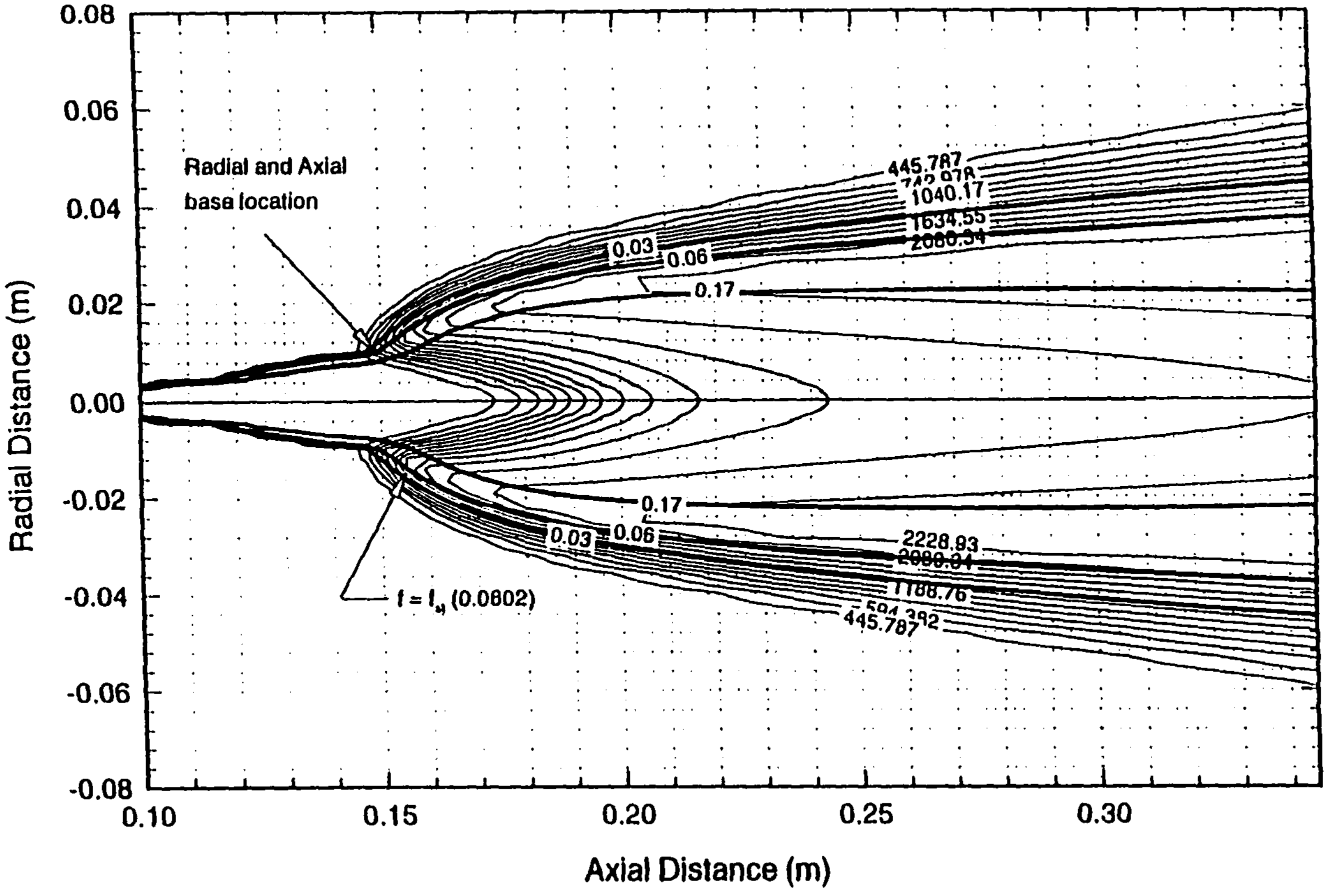

Fig. 5.12 Expanded view of temperature and mixture fraction (f) contours for the fuel jet exit velocity of 34.7 m/s.

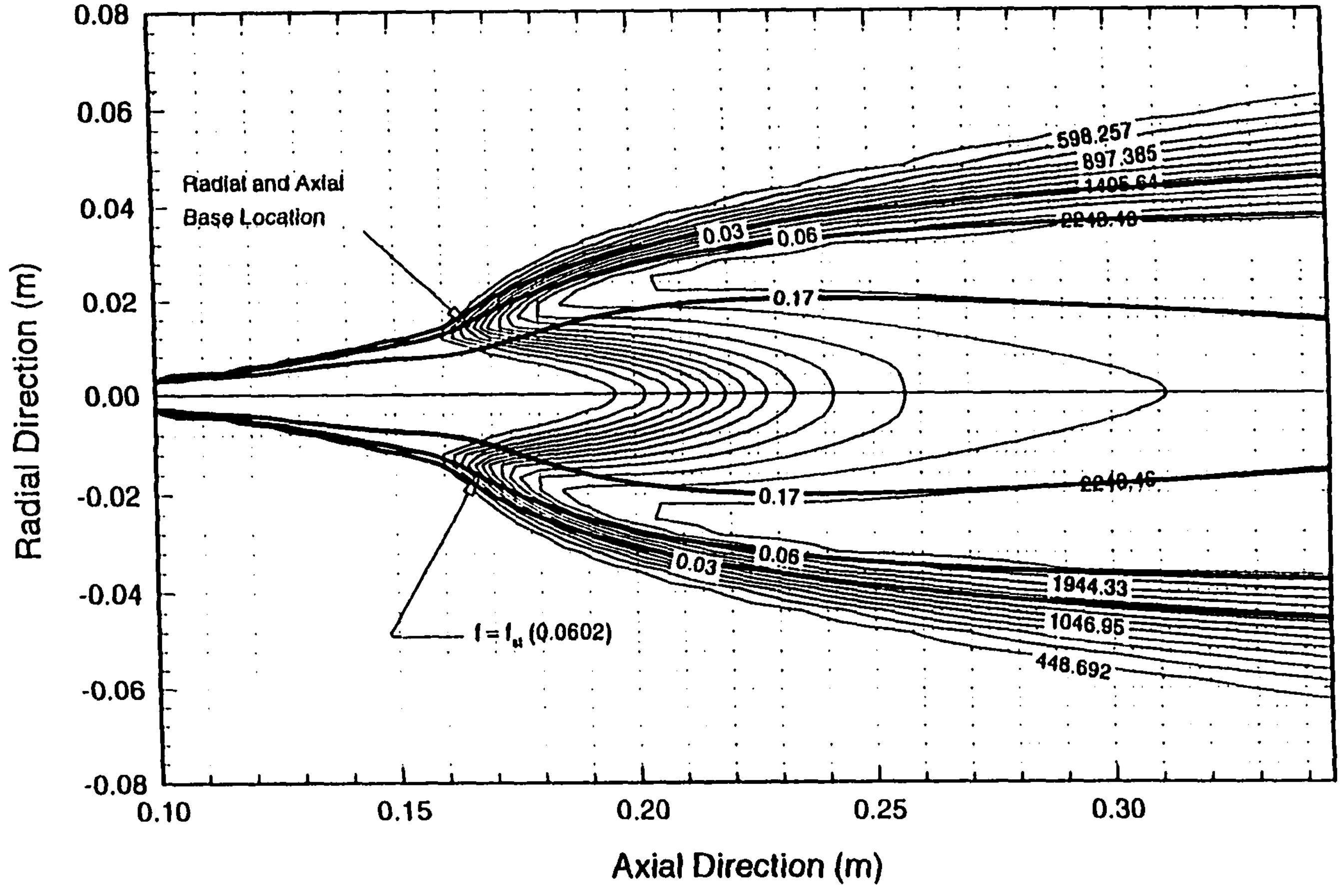

Fig. 5.13 Expanded view of temperature and mixture fraction (f) contours for the fuel jet exit velocity of 47.5 m/s.

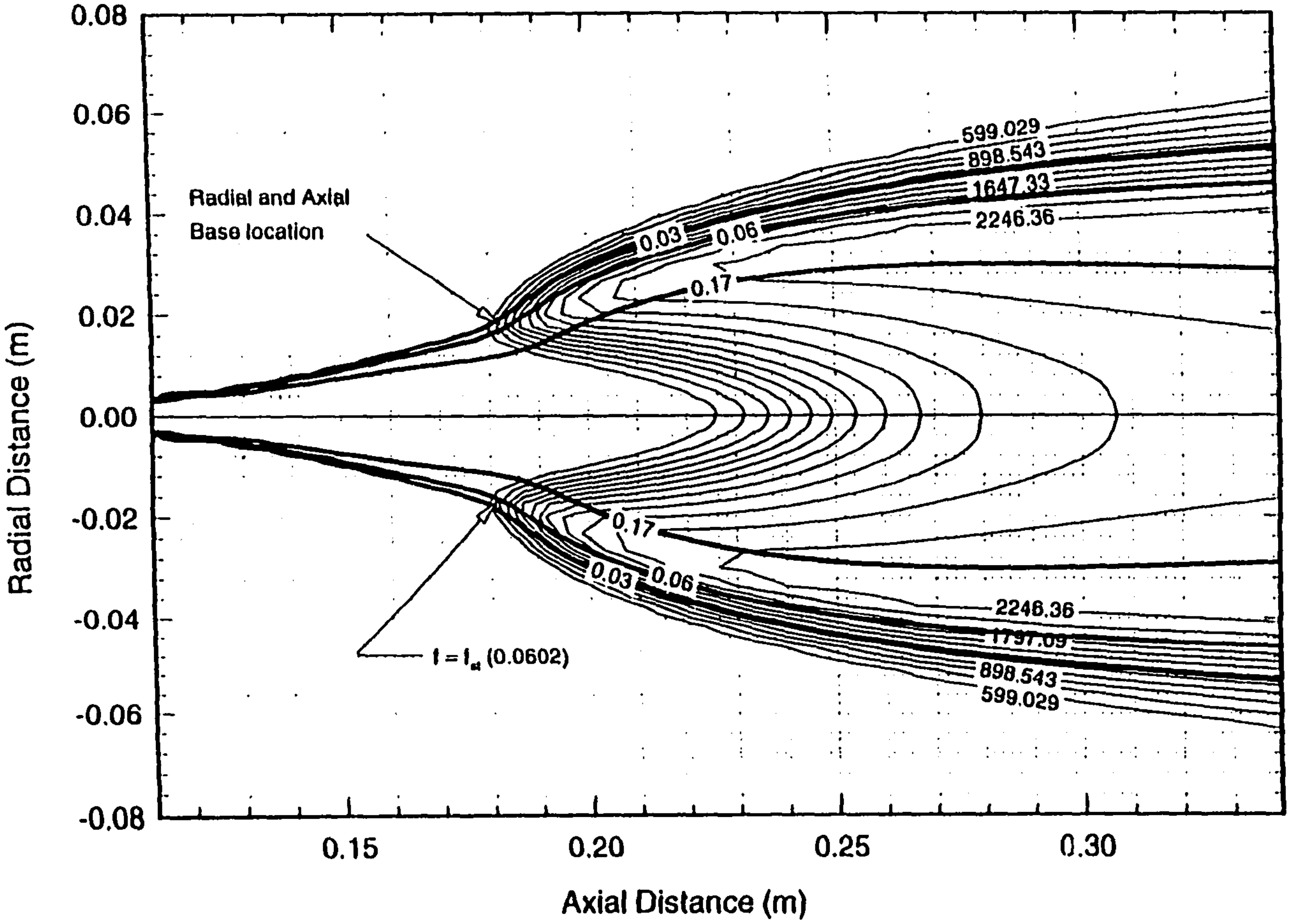

Fig. 5.14 Expanded view of temperature and mixture fraction (f) contoures for the fuel jet velocity of 60.0 m/s.

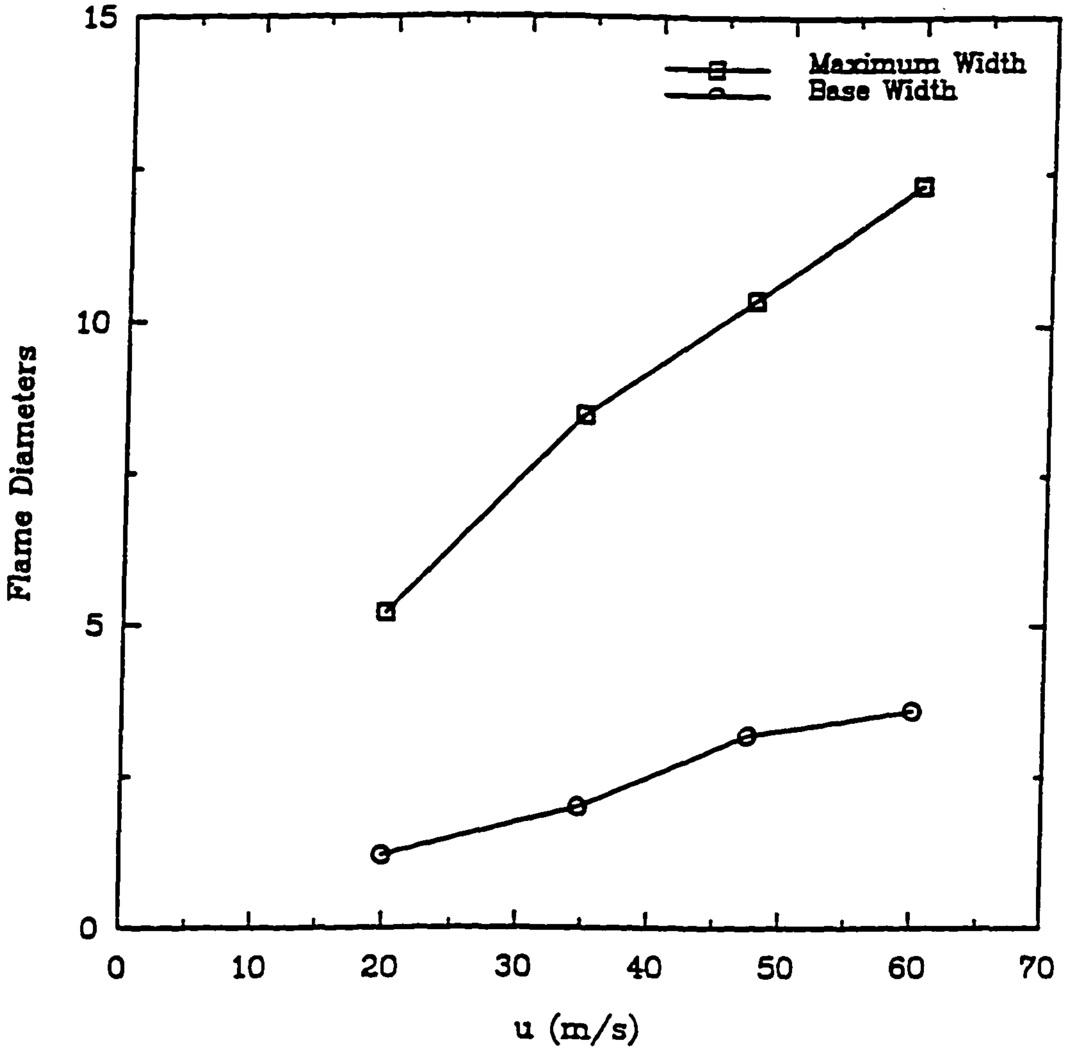

Fig. 5.15 Variation of flame base width and maximum flame width with the jet exit velocity.

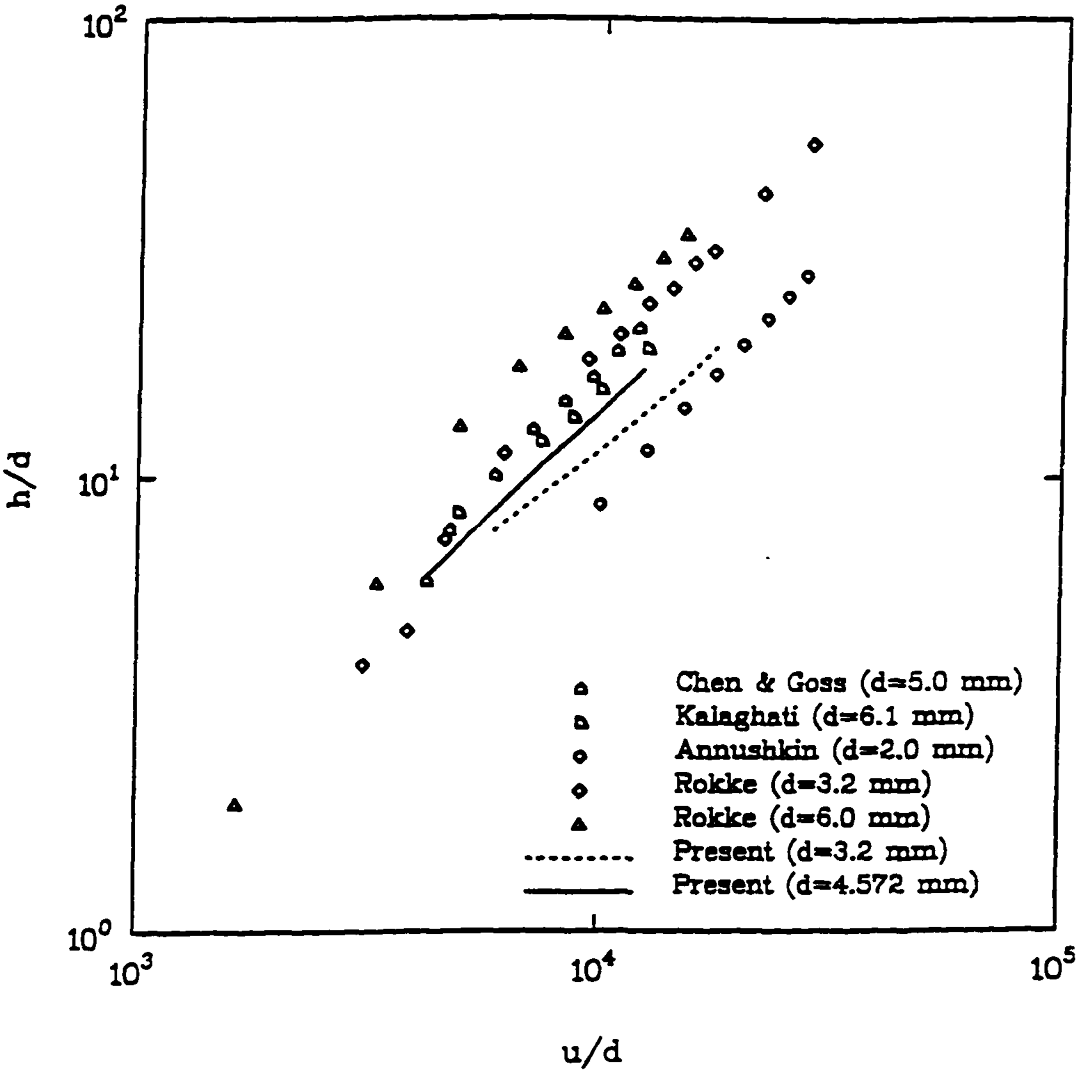

Fig. 5.16 Flame lift-off height of propane fuel at injector diameter.

Kalaghatgi, Chen and Goss and Rokke et al. It is important to note that the lift-off height results are obtained without fine tuning the empirical constants that are associated with the eddy-dissipation combustion model [33]. The figure also shows the effect of tube injector diameter. Computed results for a smaller tube diameter ($d=3.2$ *mm*) produced *h/d* ratios that are somewhat smaller than those determined with $d=4.57$ mm. This behavior has also been observed by Rokke et al.

Figure 5.17 presents the fuel burnout rate at different axial locations for jet exit velocities of 34.7, 47.5 and 60 m/s. The sudden rise of the burnout rate indicates the beginning of the chemical reaction and the base region of the flame. The flame base height is clearly identified at the axial location where a sharp change in the slope occurs. As seen from Fig. 5.17, the variation of the height with the jet velocity computed from this procedure compared favorably with the results obtained from the tangency criterion involving turbulent flame speed.

Prediction of Lift-off Height From The Non-reacting Cases

Discussions in the previous chapter indicated that the potential location of the flame base can also be approximately determined from cold flow calculations. This is once again demonstrated for propane by plotting the radial profiles of the u-component of the velocity and the calculated turbulent speed at different axial locations. Prior to determination of the potential flame base location, a comparison of the flow field predicted for the inert jet with the results predicted for the reacting jet is made. Figures 5.18 and 5.19 show the variation of velocity and the turbulent stress component u'u' along the axis of symmetry. It is observed that the results obtained from both reacting and non

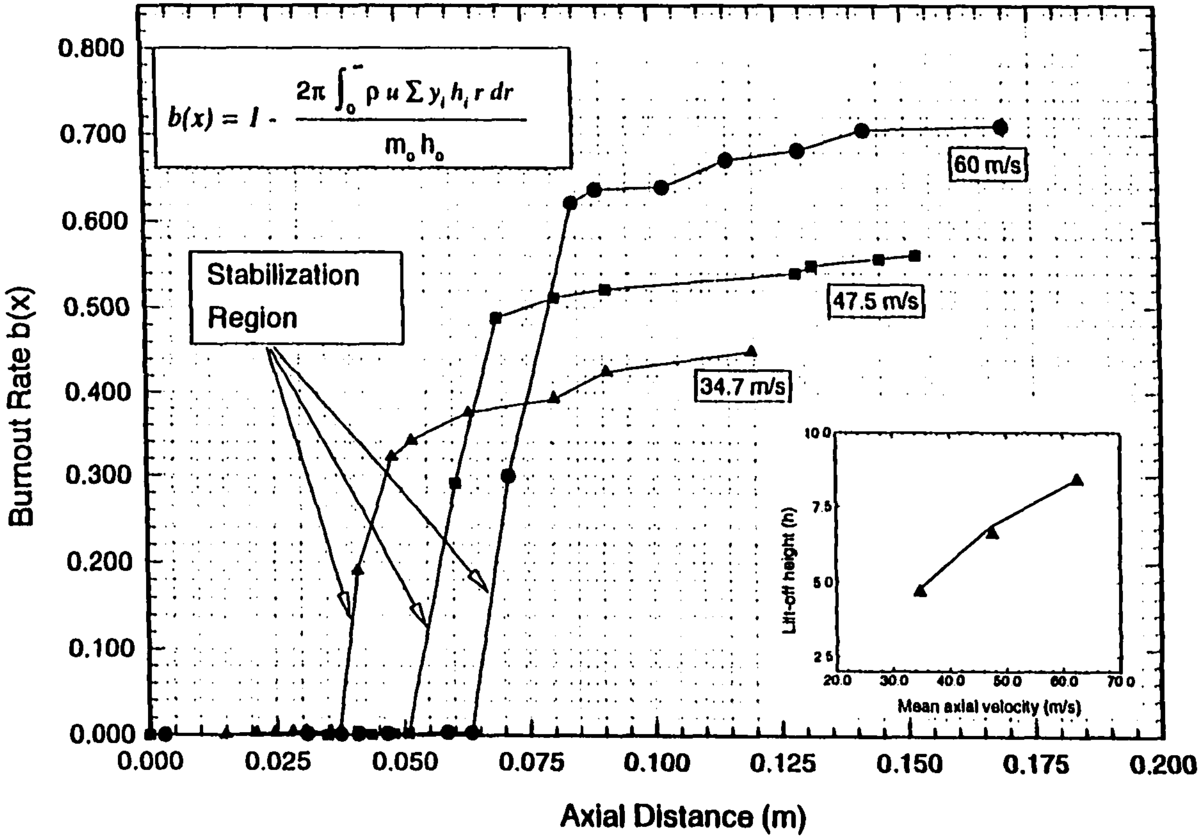

Fig. 5.17 Prediction of burnout rate along axial direction for jet exit velocity of 34.7 m/s, 47.5 and 60.0 m/s. Small graph represents lift-off height predicted using turbulent flame speed criteria (symbols) as compared to the above criteria (lines).

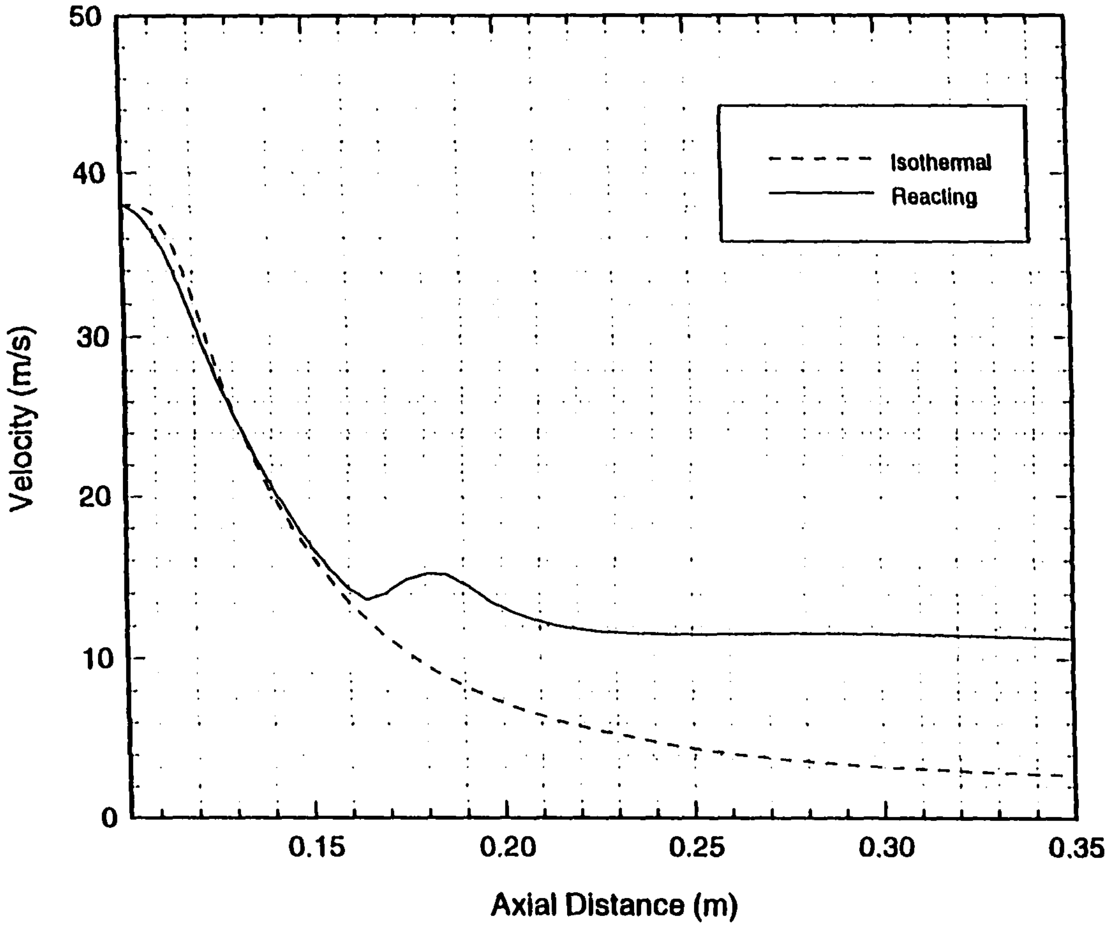

Fig. 5.18 Computed axial velocity for reacting and non-reacting flows.

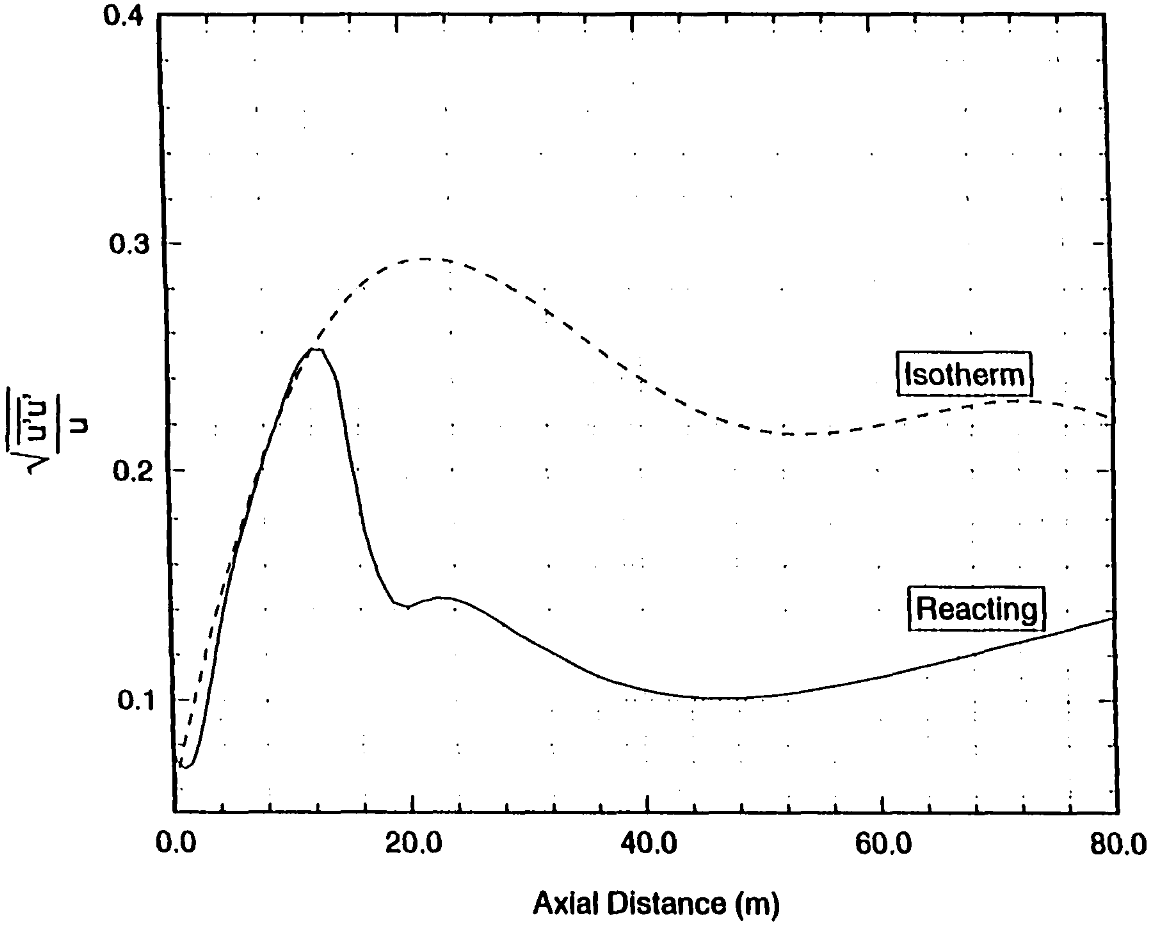

Fig. 5.19 Computed turbulent intensity for reacting and non-reacting flows.

reacting cases are nearly identical in the region prior to the flame base. After combustion initiates, the axial velocity shows a bump, due to thermal expansion in the flame base region. Figure 5.20 shows the radial profile of the u-component of velocity and the turbulent flame velocity for the non-reacting cases at three axial locations namely, $x=0.39$ m (upstream), $x=0.043$ m (potential flame base location) and $x=0.069$ m (downstream). The tangency condition in Fig. 5.20 predicts the potential location of the flame base at $x=0.043$ m for the 34.7 m/s axial velocity case. This compares with a value of $x=0.047$ m for the reacting case, representing a 8% deviation from the reacting case.

5.2 Results for Methane/Hydrogen Mixtures

Most of the past studies that involve the prediction of turbulent diffusion flame structure and stabilization region have generally been restricted to single component fuels. Fuels consisting of two different combustible gases have been discussed in the literature as means of increasing the combustion performance. Several cases, involving increasing proportion of hydrogen in a methane-hydrogen mixture are calculated and analyzed. Figure 5.21 shows comparison of the flame structure of a pure methane flame and a flame formed by a 95% CH_4 and 5% H_2 fuel mixture. It is evident that the flame base in the mixture moved upstream compared to the pure methane flame. Also, the flame base has smaller width compared to the pure methane flame. Figure 5.22 shows the flames for the 90% CH_4 - 10% H_2 and 85% CH_4 - 15 $\%$ H_2 fuel mixtures. The flame as expected continues to move upstream and its base keeps getting narrower as the hydrogen concentration increases in the fuel mixture. This is expected since hydrogen has a maximum burning velocity about six times greater than that of methane. Figure 5.23

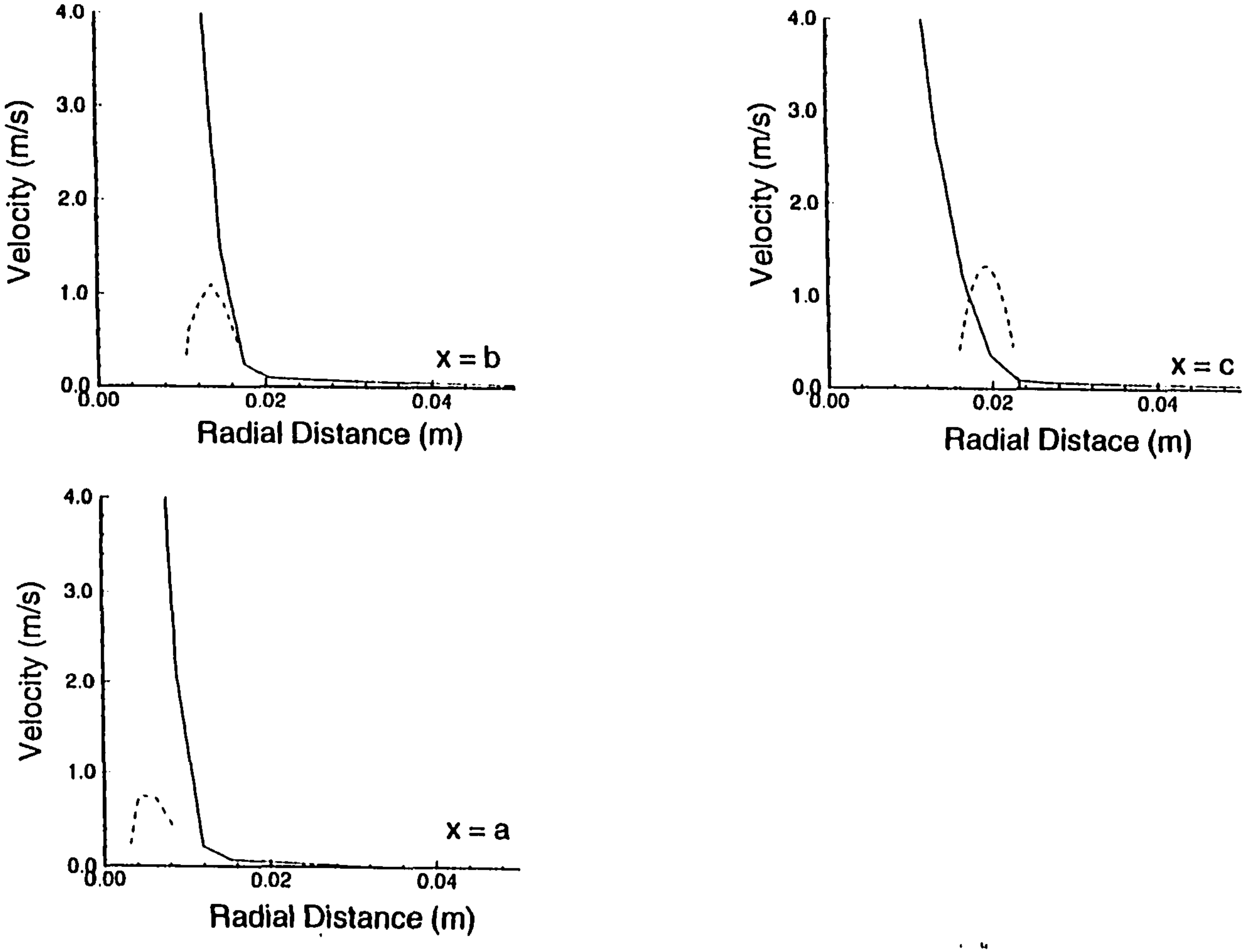

Fig. 5.20 Velocity and turbulent flame speed profiles at different axial locations (a=.039 m, b=.043 m & c=.069 m) for the fuel jet velocity of 34.7 m/s (fuel C_3H_8).

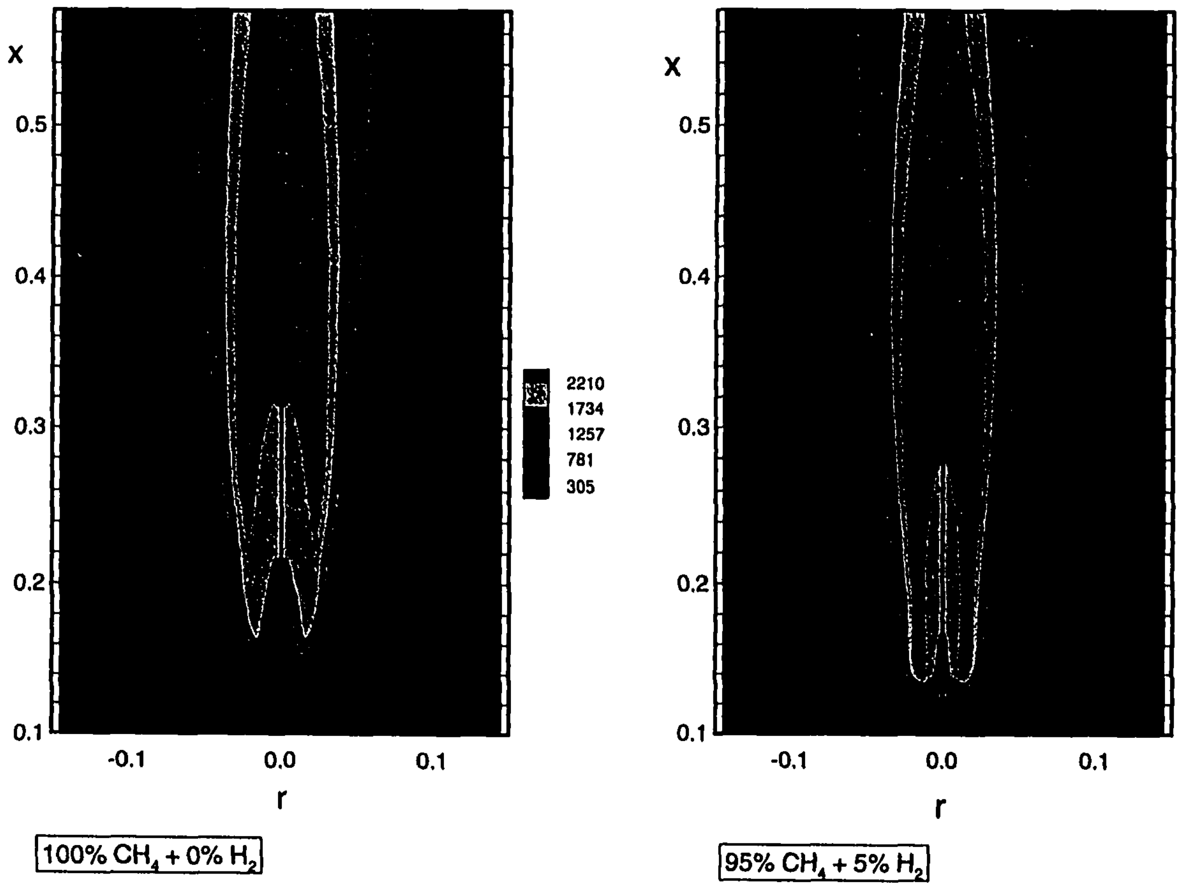

Fig. 5.21 Prediction of temperature field for the two different mixture ratios of CH_4/H_2 fuels. Jet exit velocity of 34.7 m/s.

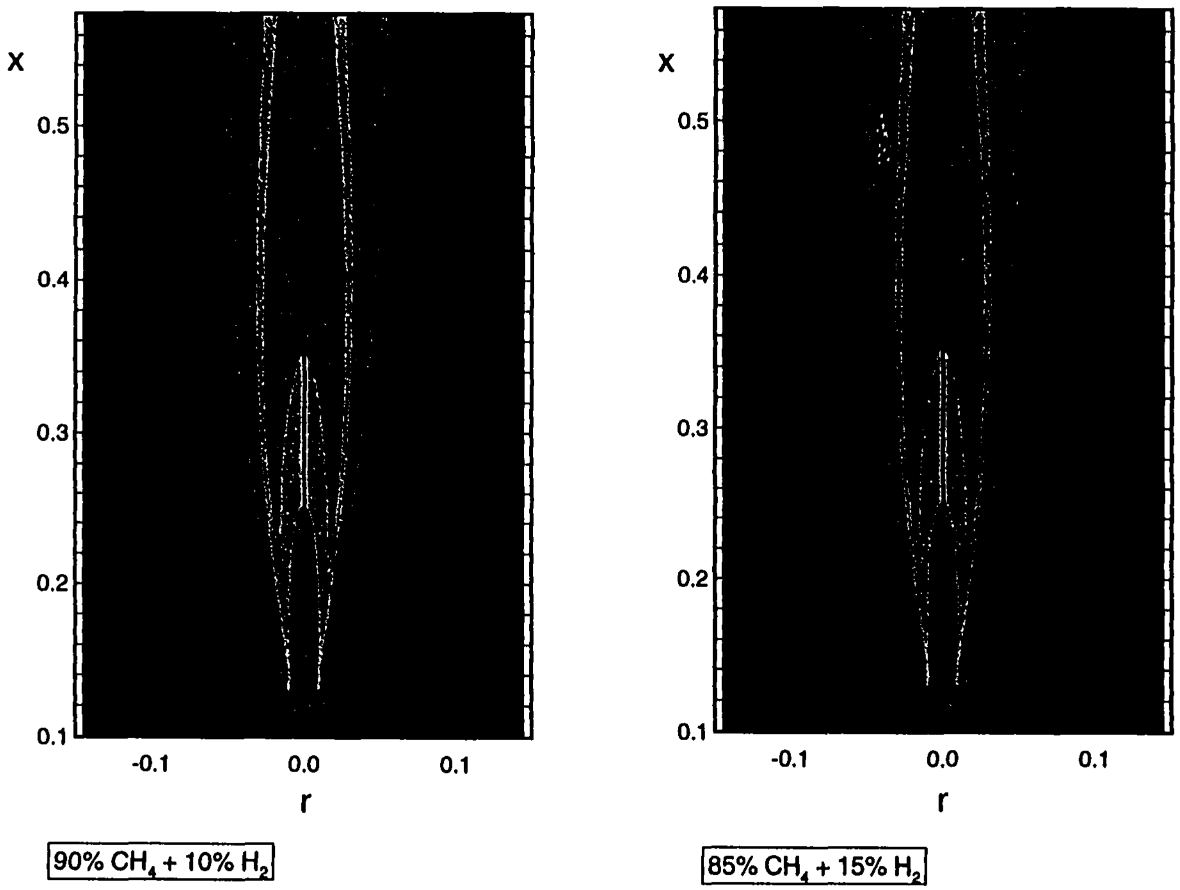

$90\%\ CH_4 + 10\%\ H_2$

$85\%\ CH_4 + 15\%\ H_2$

Fig. 5.22 Prediction of temperature field for the two different mixture ratios of CH_4/H_2 fuels. Jet exit velocity of 34.7 m/s.

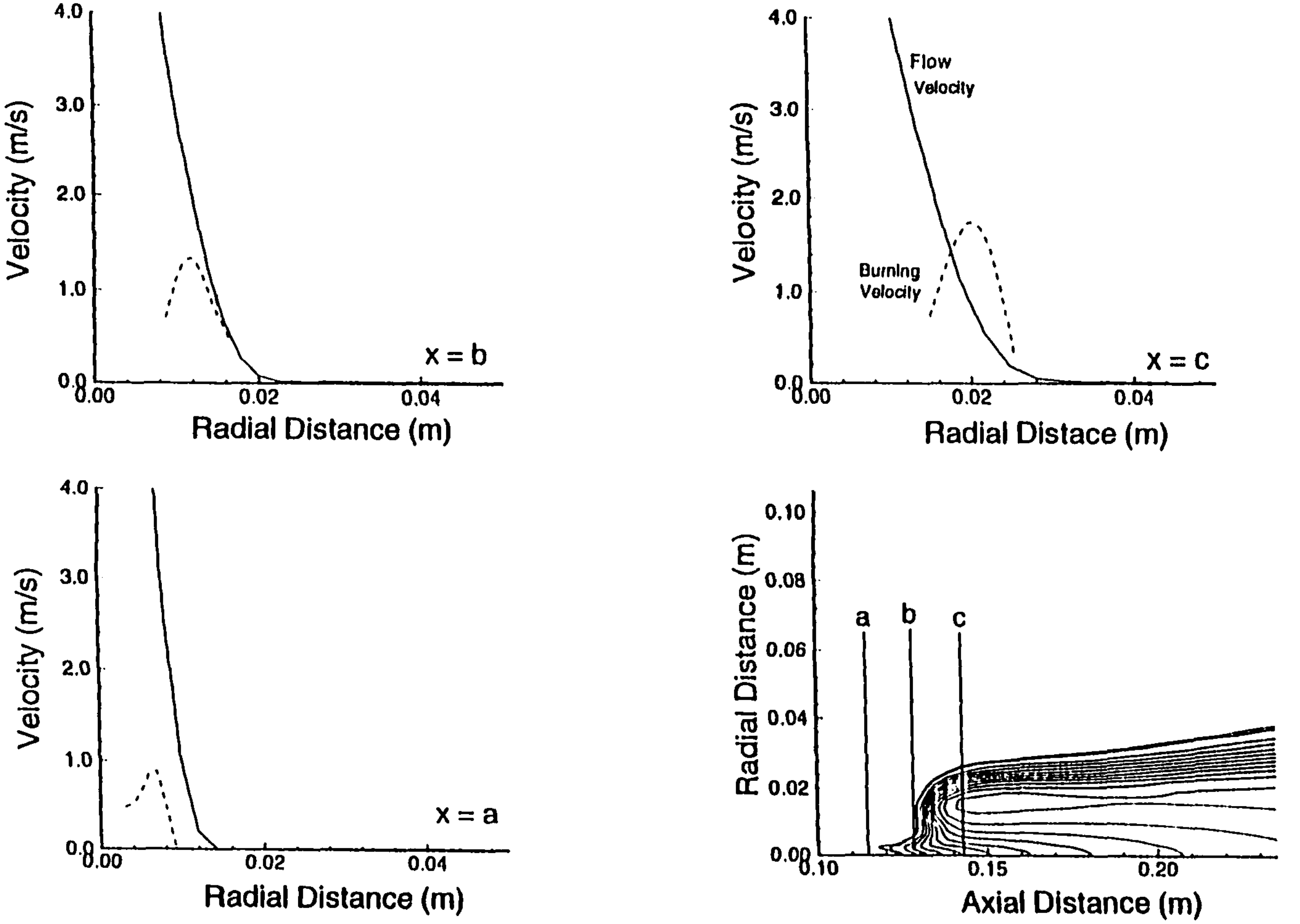

Fig. 5.23 Velocity and turbulent flame speed profiles at different axial locations (a=.013 m, b=.027 m & c=.069 m) for the fuel jet velocity of 34.7 m/s (fuel mixture 95%CH_4 + 5%H_2).

shows the mechanism discussed in Chap. 4 for locating the flame base for the mixture, using the tangency condition between the turbulent flame velocity and the u-component of flow velocity. The flame base height for the *5%* H_2 case is found to be *2.7 cm*, using the tangency condition in Fig. 5.23. The turbulent flame velocity is computed from the Eq. (3.17) in terms of the laminar burning velocity and the turbulent Reynolds number. The laminar speed for the mixture is calculated using a mixing rule proposed by Spalding [90, 91].

Figures 5.24 and 5.25 show the expanded view of the flame temperature field superimposed on the mixture fraction field. These figures once again demonstrate the hypothesis of Vanquickenborne and van Tiggelen that the flame base is anchored between the lower and upper flammability limits. The conical region, centered around the axis where the unreacted fuel penetrates into the interior region of the flame, clearly exists for the pure methane flame case. However, as seen in Figs 5.21 and 5.22 this region fades as the hydrogen concentration is increased in fuel mixture.

The fuel burnout rate profiles for the fuel mixtures are plotted in Fig. 5.26. The steep rise of the burnout rate is indicative, as in the case of pure fuels, of the flame stabilization region. It is also noted that the location of the steep change in the burning rate moves toward the injection point as the ratio of hydrogen is increased in the mixture. The lift-off height, predicted as the location where the change in slope of burning rate starts ($h=2.56$ *cm*), compares favorably with the result obtained from the Fig. 5.23 ($h=2.7$ *cm*) for the *95%* CH_4 - *5%* H_2 fuel. The lift-off height for different mixture ratios is also shown in the same figure. It is also evident from the Fig. 5.26 that the rate of burnout increases with higher hydrogen ratio. This is an indication that the combustion initiates earlier and is completed earlier. Thus, a smaller portion of the unreacted fuel would exist at the end of the domain as a result of increasing hydrogen concentration in the mixture. This is shown to be the case in Fig. 5.27 where the radial profiles of unburnt methane for different hydrogen ratios are plotted at an axial location of 0.45 m from the injection point. This figure shows that the depletion of methane is increased as the H_2 concentration increases in the fuel mixture. One of the contribution of this section is the demonstration of the fact that the stabilization region of the flame resulting from the combustion of a fuel mixture can be computed using the same mechanism that has been developed for the flames from pure fuels. Although there are no data available for the mixtures to compare with the predicted results, one can test the behavior of predicted lift-off height for all mixture fuels cases using the scaling procedure, based on the experimental observation by Kalaghatgi [7]. Figure 5.28 shows the variation of the ratio of lift-off height (h) and the tube diameter (d) with the jet exit velocity divided by the square of the maximum laminar flame speed. The cases presented here include pure CH_4, pure C_3H_8 and mixtures fuels. Numerical results agree with the following experimental findings [7]:

1. h/d varies linearly with jet velocity, except at small values of h,
2. h/d is inversely proportional to $(S_u^2)_{max}$,
3. h/d is nearly independent of d.

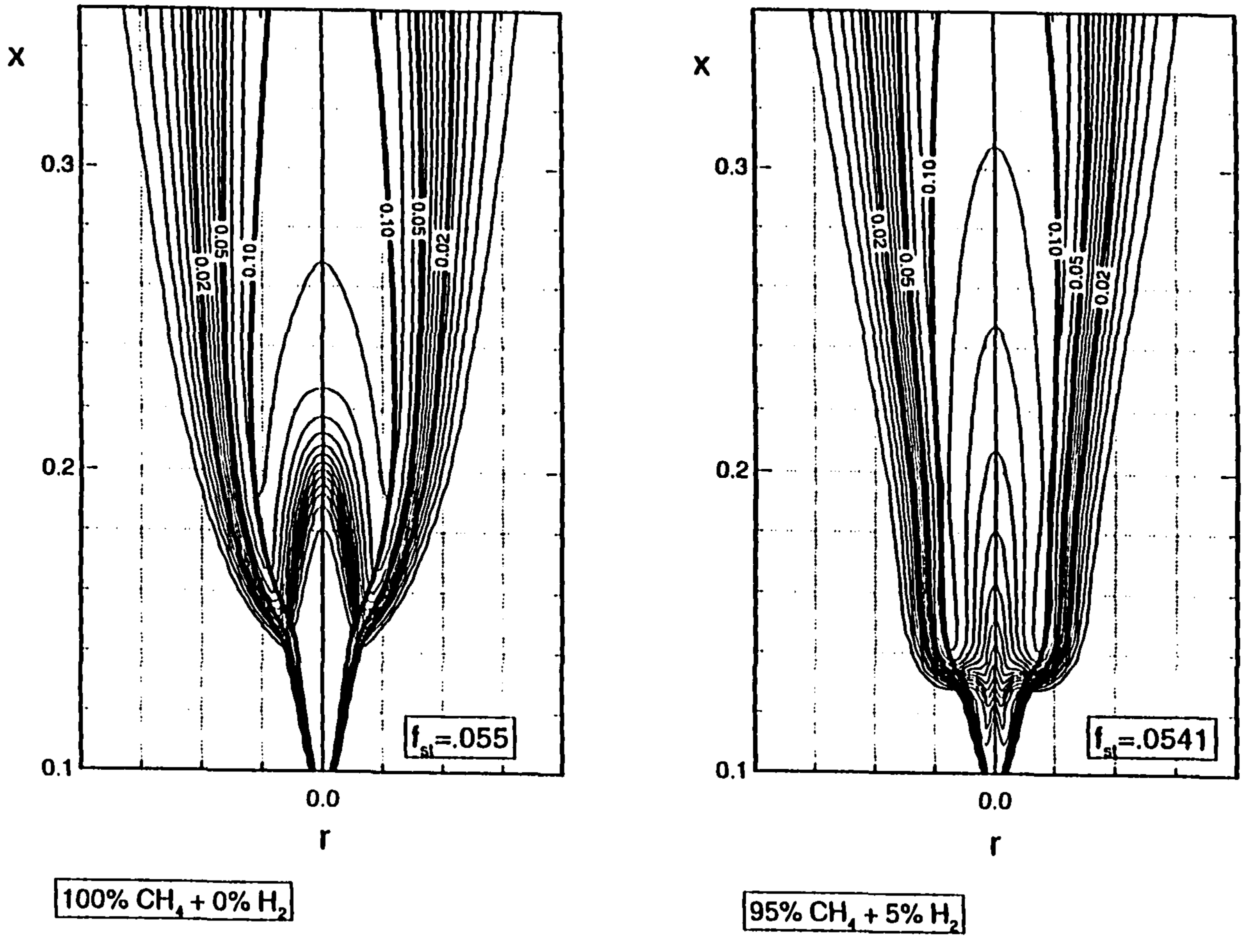

Fig. 5.24 Expanded view of temperature and mixture fraction contours for the two types of mixtures CH_4/H_2 fuels. Jet exit velocity of 34.7 m/s.

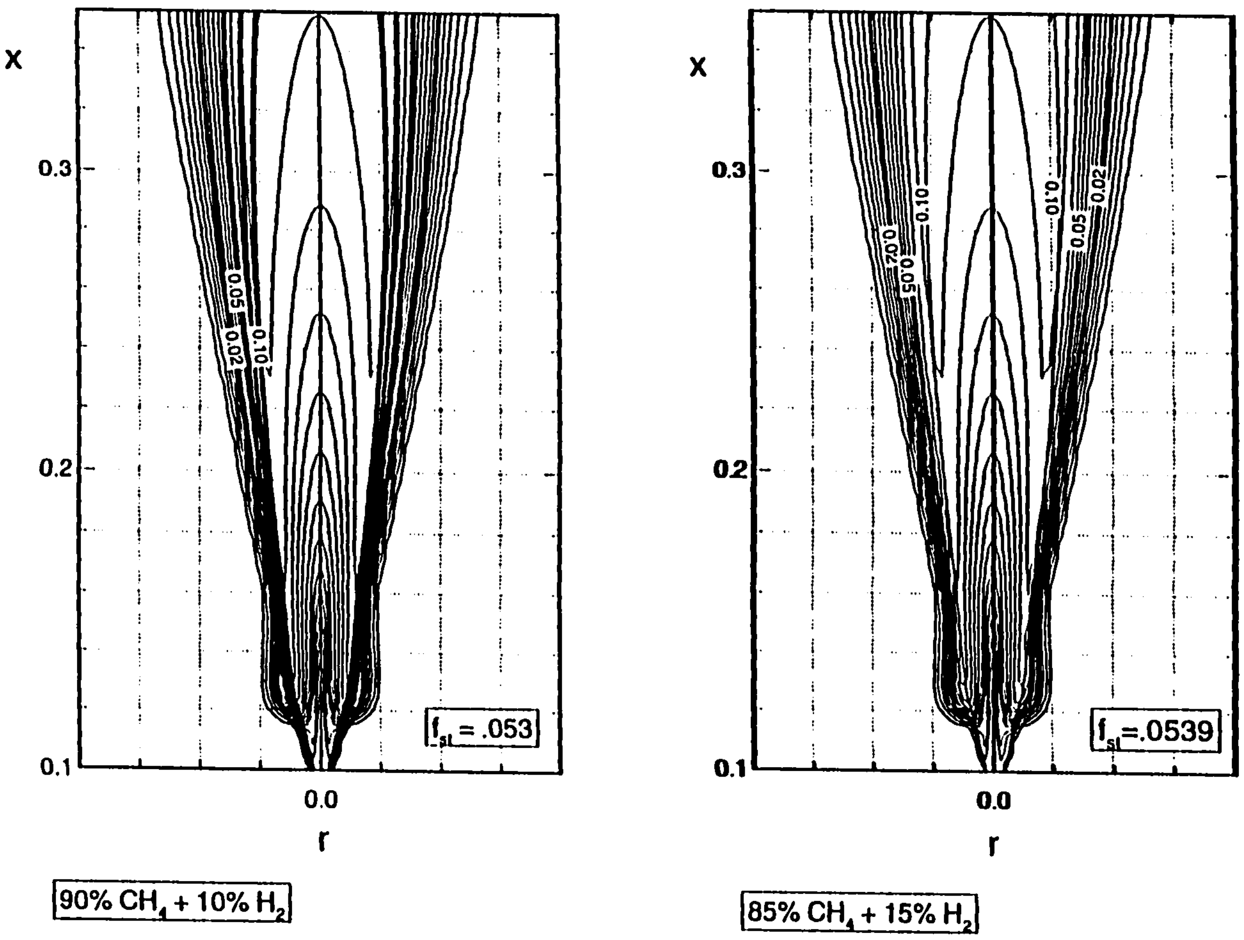

Fig. 5.25 Expanded view of temperature and mixture fraction contours for the two types of mixtures CH_4/H_2 fuels. Jet exit velocity of 34.7 m/s.

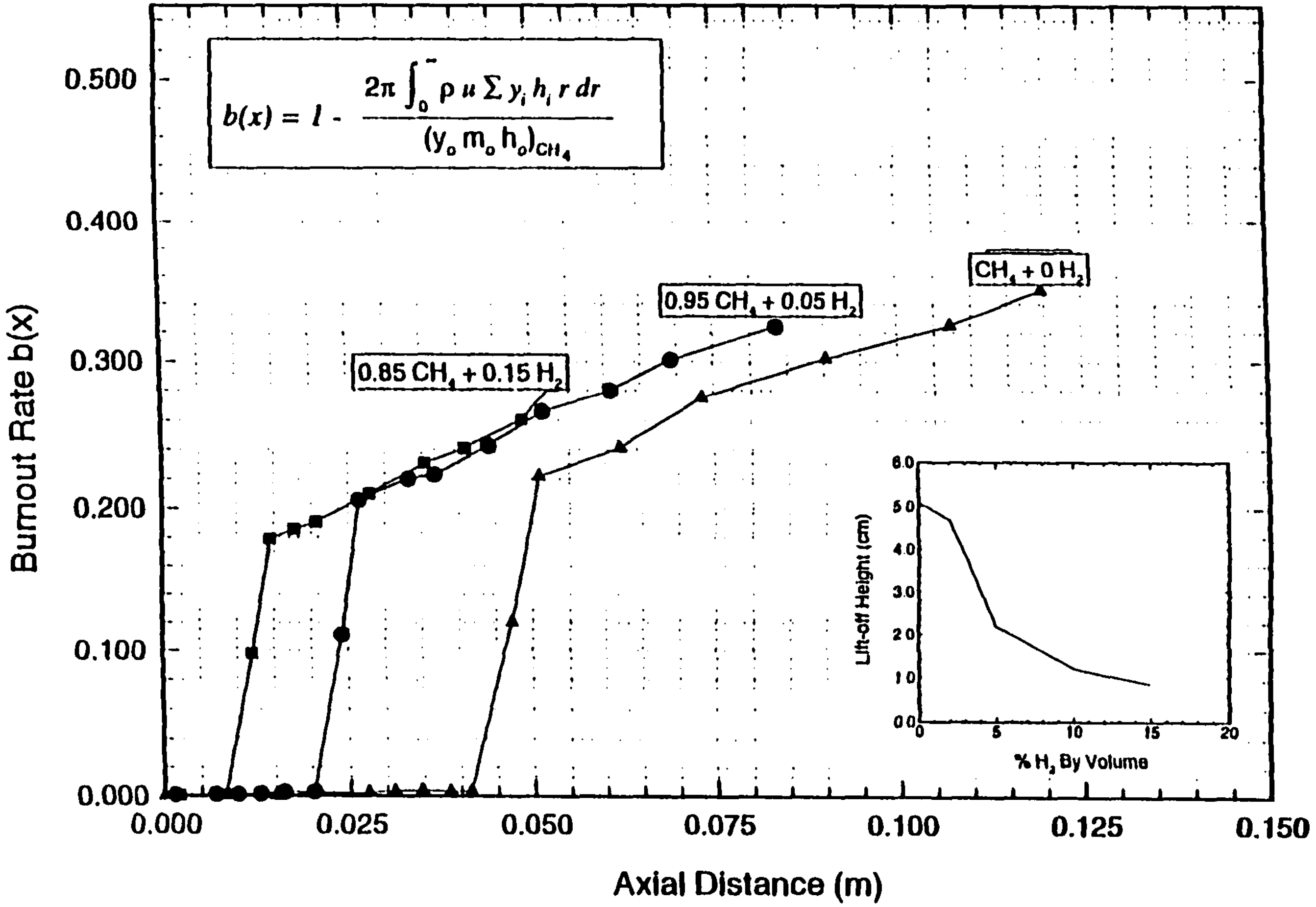

Fig. 5.26 **Prediction of burnout rate along axial direction for jet exit velocity of 34.7 and various mixures. Small graph shows the effect of the above compositions on flame lift-off height.**

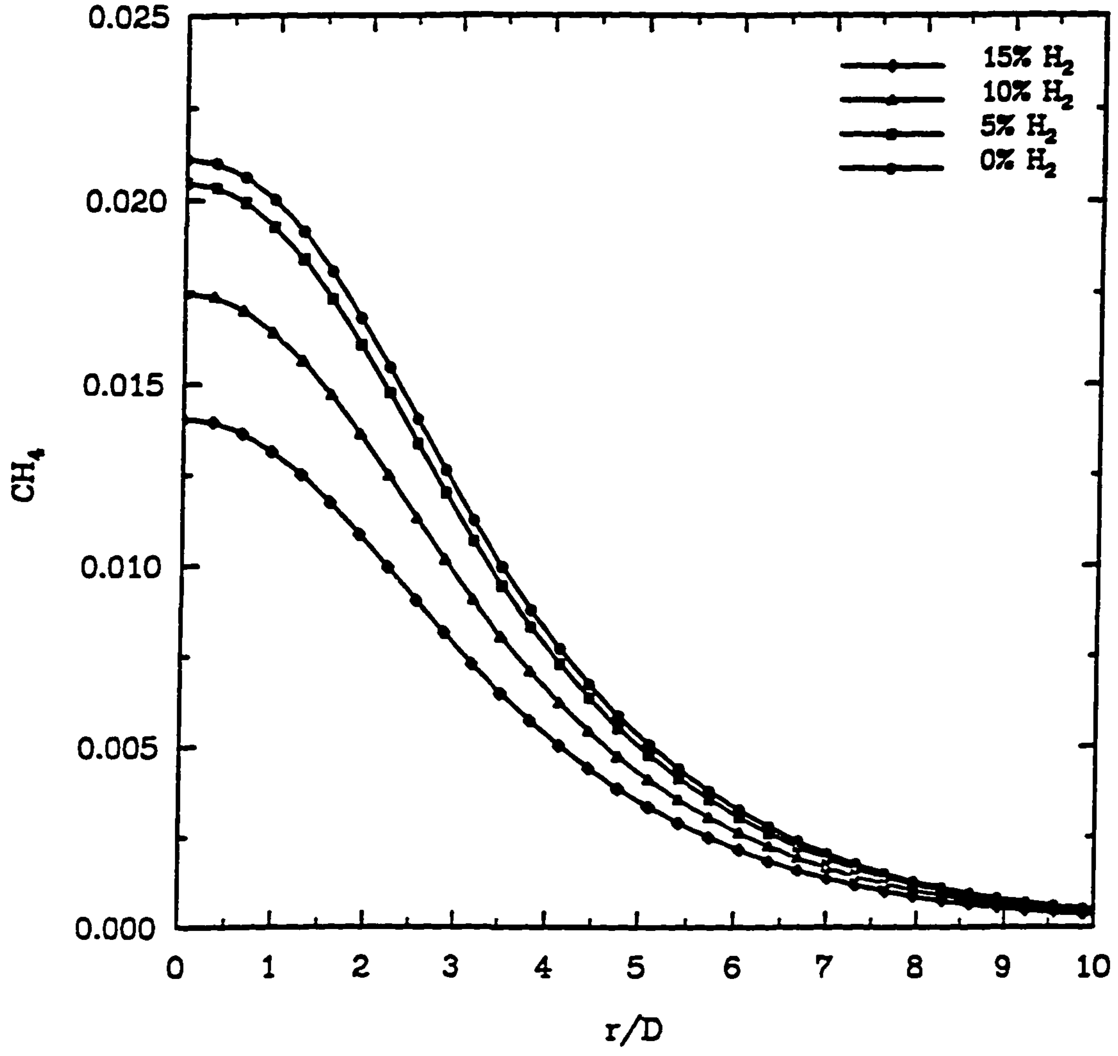

Fig. 5.27 Prediction of CH_4 mass fraction at axial location of 45 cm from the injection point.

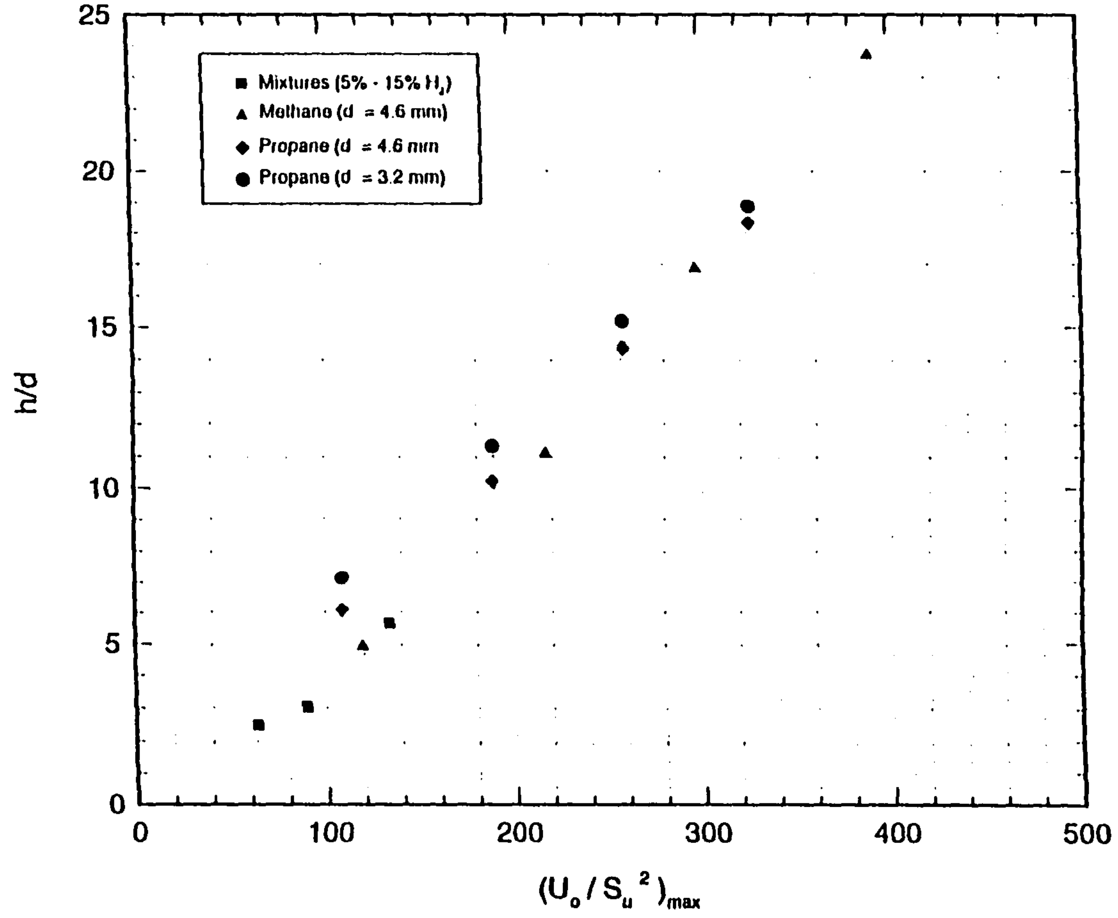

Fig. 5.28 Variation of lift-off to diameter ratio with the jet velocity divided by the square of the maximum laminar flame speed.

For propane, experimental study by Rokke et al. [31] has shown that the lift-off height may also be weakly dependent on the injector diameter *d*. In this study, the lift-off height for propane is also shown to be weakly dependent on the diameter (Fig. 5.16).

5.3 Results From The PDF/Flame Sheet Model

All the results that have been discussed thus far in Chap. 4 and the preceding sections of Chap. 5 are obtained based on the eddy dissipation model employed in conjunction with the RSM model. The predicted flame properties such as species concentration, flame lift-off height and width are in reasonable accord with the experimental data. However, this model has been challenged in many studies in the literature due to its simplicity, lack of solid theoretical foundation, and the need to change constants in the model to fit the data. As a result, we have also attempted to predict the flame structure using the PDF/flamelet model as an alternative to the eddy dissipation model. Previous Studies [2, 34, 90, 91] have compared both models, and have suggested that the results from the PDF model compare better with experiments as compared to the eddy dissipation model predictions. However, all previous studies using the eddy dissipation model have employed the k-ϵ model for prediction of turbulence properties. As noted in this study, the accuracy of the turbulence model is extremely important in prediction of reliable results when using it with the eddy dissipation model. Clearly, the RSM, as the present study shows, should be used with the eddy dissipation model.

In this section, results for pure methane determined from the PDF/Flame sheet model are discussed, and compared with the results obtained from the eddy dissipation model in Chap. 4. Combustion is modeled by introducing a transport equation for a conserved scalar *f* (mixture fraction) as discussed in Chap. 2. Figure 5.29 shows comparison of flames predicted by the PDF/Flame sheet model and eddy dissipation model/RSM. This figure shows that both models produced different flame shapes near the flame base but have nearly identical prediction in the far field region. For example, the flame base is much narrower in the PDF/Flame sheet model. We also observe small isolated regions of combustion between the flame base and the fuel injection point. Figures. 5.30 and 5.31 show the predicted radial mass fraction profiles of different species from both models at *x=5.34 cm* (near flame base) and *x=34.91 cm*, a downstream location. It is evident that the predicted profiles from both models are significantly different at the near field location but are in good accord at the downstream location. Near the flame base, the radial profiles of CH_4, O2, CO and CO_2 show similar trends but numerical values show significant deviation.

Flame Base Location

The results from the PDF model were obtained by adjusting the value of scalar dissipation coefficient C_{g2} in Eq. (2.21). A value of $C_{g2} = 8.2$ has been used in the present study. The value of C_{g2} has also been also adjusted in many prominent studies such as by Peters and Williams [11], Sanders and Lamers [12], Bradley et al. [13], and Bray and Peters [82] in order to predict results for flame base height that are in accord with experiments. The concept of lift-off described by Peters and Williams [11] relates the local dissipation rate at stoichiometry (χ_{st}) with its quenching value (χ_q). The flame exists depending on the criterion that compares χ_{st} with χ_q. For values $\chi_{st} > \chi_q$ the flame is extinguished. Also, the studies by Peters and Williams have suggested that for value of

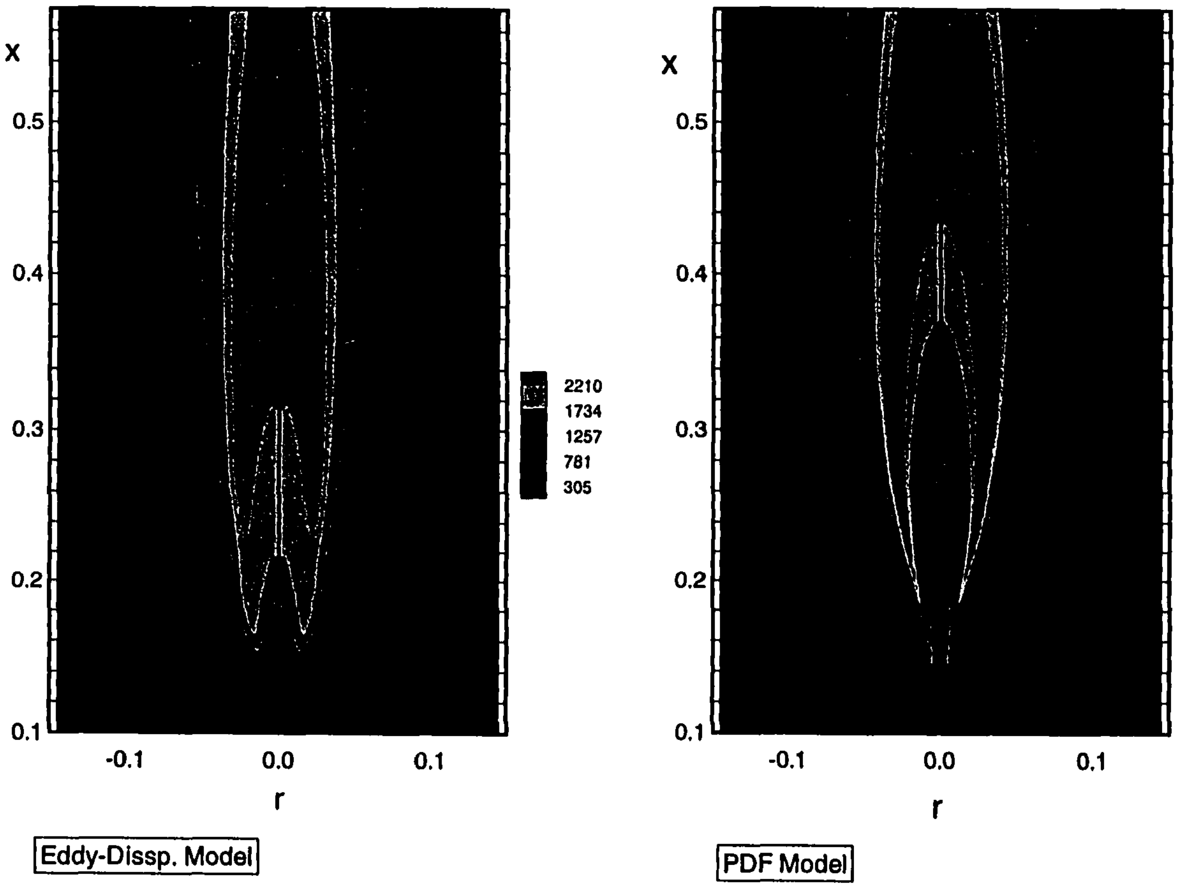

Fig. 5.29 Prediction of temperature field for the two different combustion models for methane fuel jet exit velocity of 34.7 m/s.

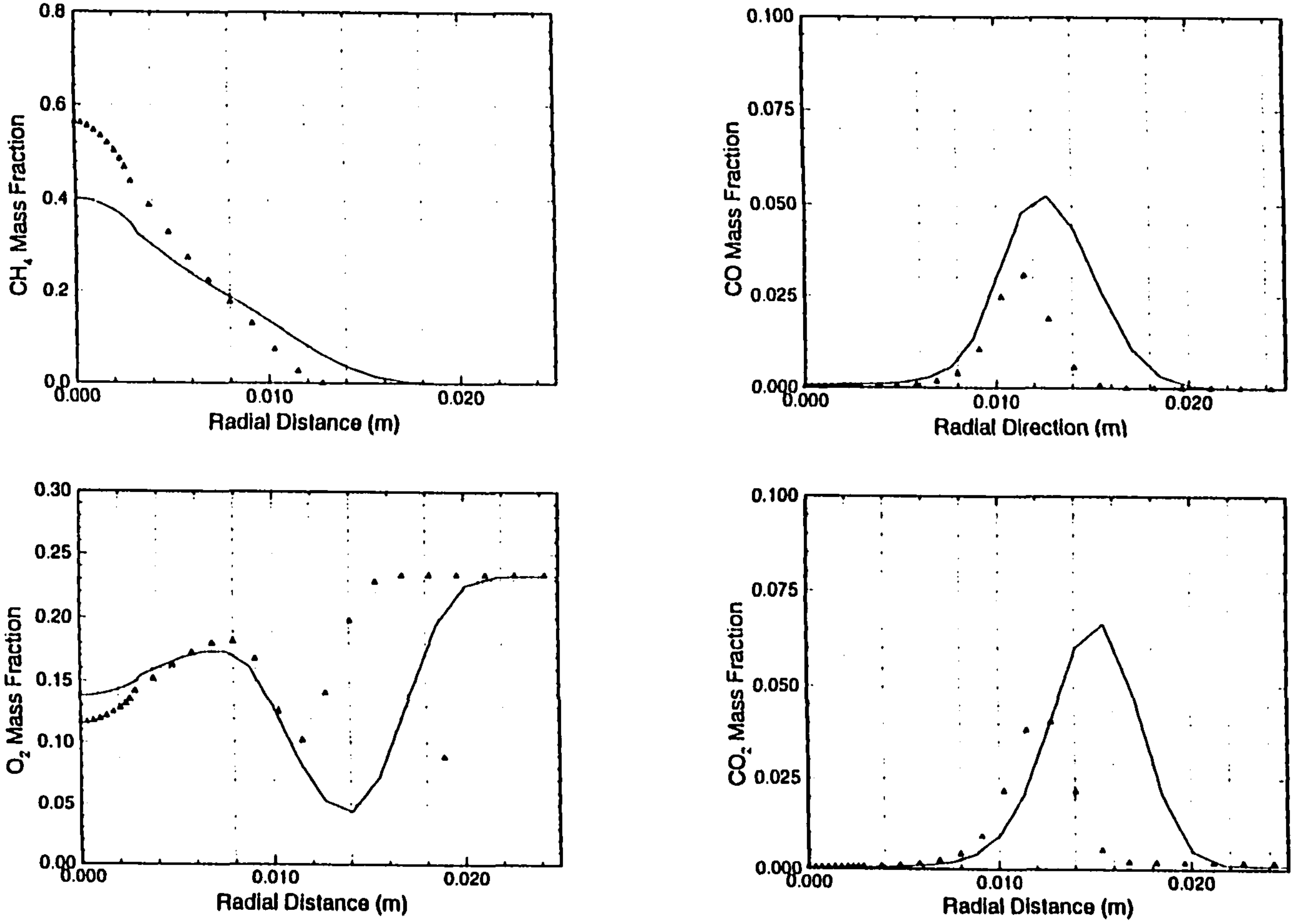

Fig 5.30 Comparison of predicted mass fractions between the two combustion models, with symbols representing the (PDF Model), and solid lines representing the (Eddy Dissipation Model) at an axial location of 5.3 cm.

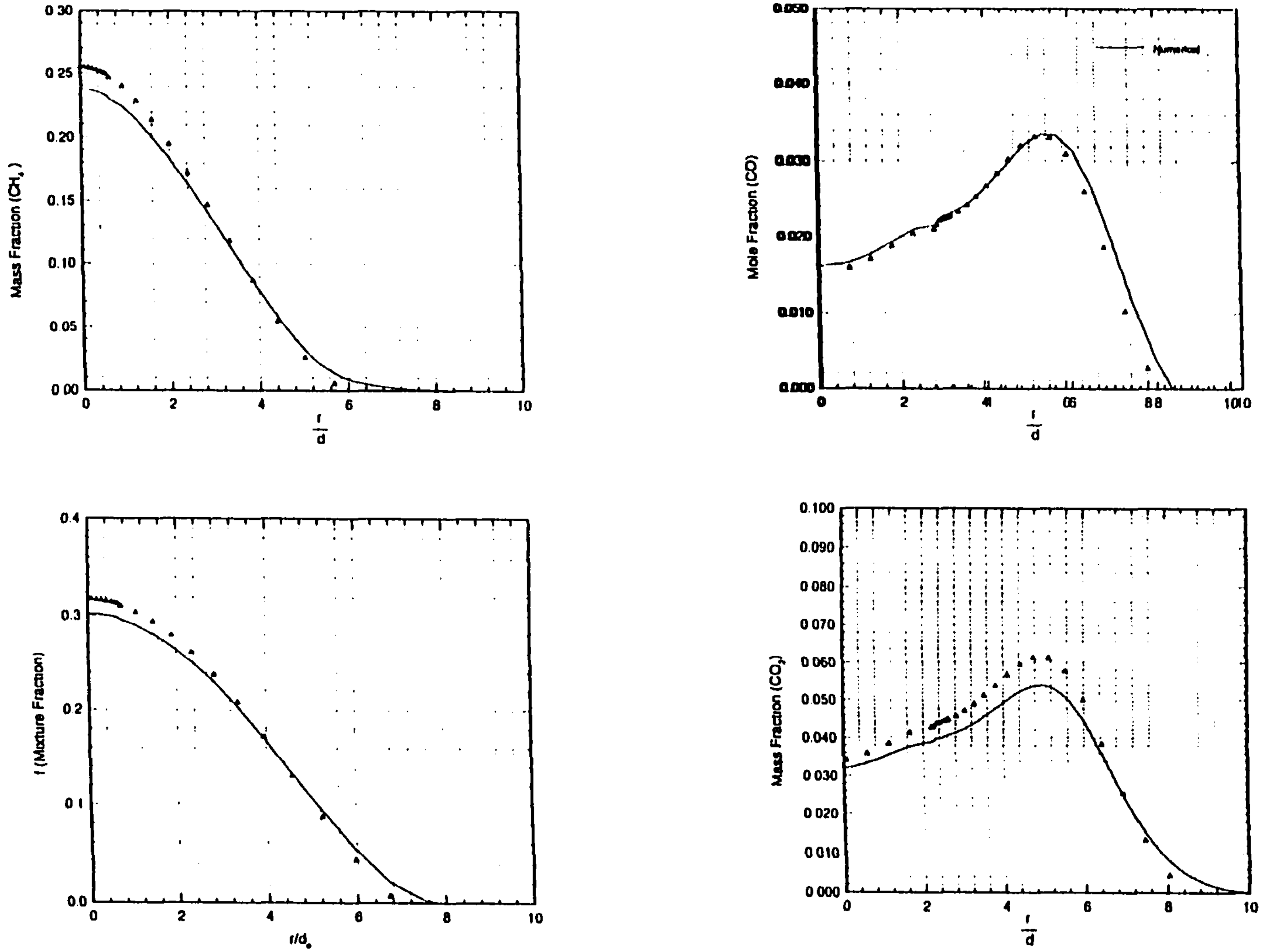

Fig 5.31 Comparison of predicted mass fractions between the two combustion models, with symbols representing the (PDF Model), and solid lines representing the (Eddy Dissipation Model) at an axial location of 34 cm.

χ_{st} higher than the quenching value, holes may exist instead of flame. This, as stated earlier, has been observed in Fig. 5.30 where combustion zones separated by holes exist. The procedure for locating the flame base for the PDF/Flame sheet theory is shown in Fig. 5.32 for the jet velocity case of 34.7 m/s. In Figure 5.32a, the radial χ profile for the stoichiometric value is shown. The flame base is obtained using the criterion $\chi_{st} = \chi_{q}$, where χ_q calculated from Eq. (3.2) turns out to be 6.2. Figure 5.32b shows the corresponding axial location of r_{st}, and from this figure the flame base is found to be located at *x=4.8 cm*. The exact location of the base is denoted in Fig. 5.32c which shows an expanded view of the temperature contours. The flame width is indicated to be *2.2 cm*. The corresponding flame base width predicted from the eddy dissipation model is *3.3 cm* as compared to *3.6 cm* from the experimental results [8].

5.4 Flame Stabilization in Swirling Flows

Swirling flows are widely used with industrial burners in order to improve burnout characteristics and flame stability. With strong swirl, the centrifugal forces and induced pressure gradients generate a toriodal vortex type of recirculation zone in the flame region near the burner injection point. The recirculating fluid generates region of high turbulence in the shear layer between forward and the reverse flow, resulting in faster mixing of combustion air with the injected fuel. Figure 5.33 shows the velocity vectors for two cases, namely one with swirl component and the other without the swirl velocity at the injection point. Both cases were computed using the RSM model and the eddy dissipation model for methane. The jet exit velocity is chosen as *34.7 m/s*, and for the swirl case, the ratio of axial velocity to tangential velocity at inlet is *1.24*. Figure 5.34 shows the

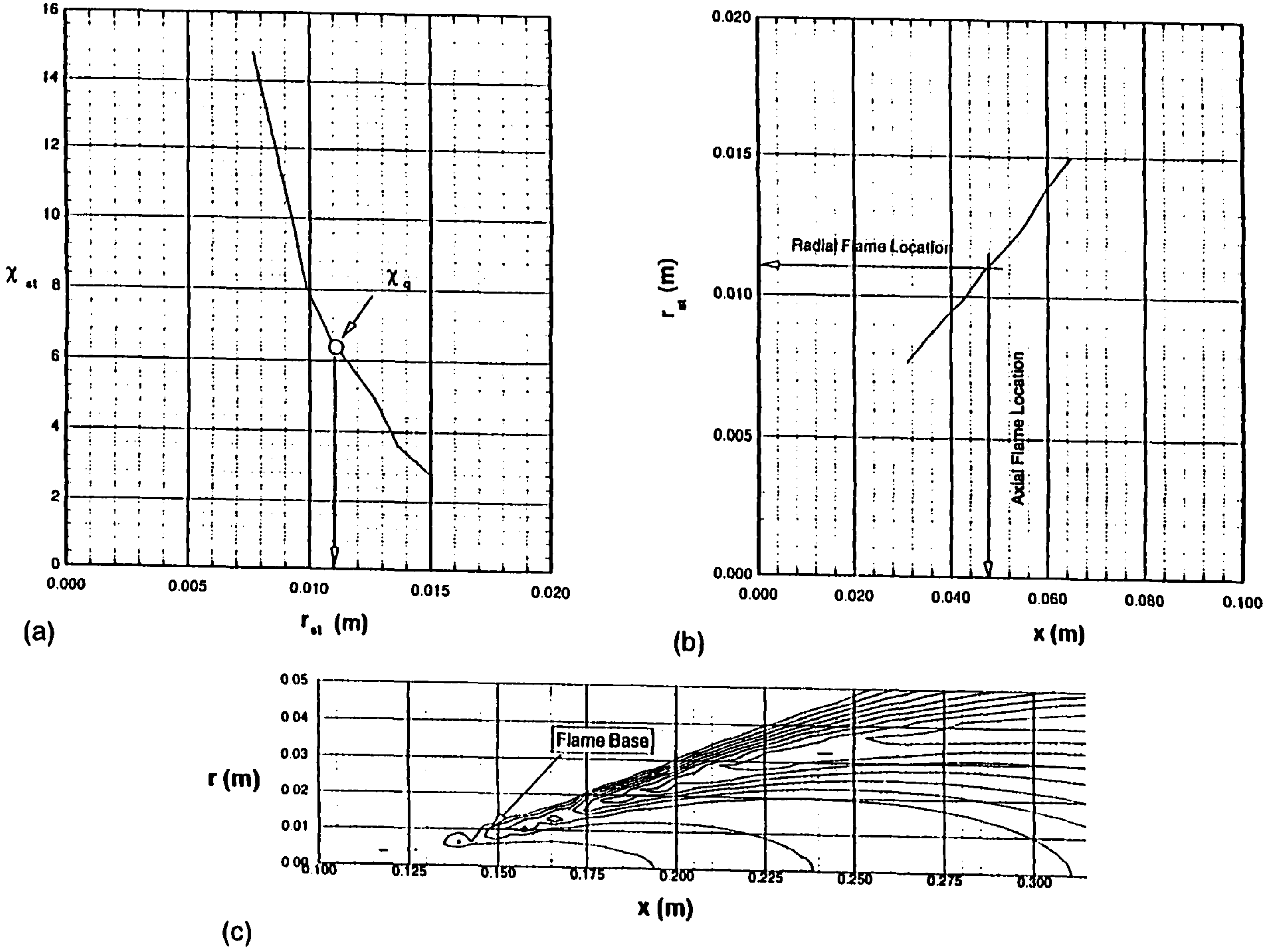

Fig. 5.32 Procedure of locatin axial and radial position of flame base for jet exit velocity of 34.7 m/s, (a) radial profile of χ_{st}, (b) corresponding axial location of r_{st} and (c) expanded view of flame structre near the base.

temperature field for both cases. It is noted that the flame base moves upstream in the swirling flow case and also becomes wider. Increasing the swirl increases the decay in axial velocity and the flame base, in accordance with the tangency condition, moves closer to the burner. The effect of swirl component on combustion is illustrated further by calculating the rate of fuel burnout *b(x)*. Figure 5.35 shows the comparison of b(x) calculated from the swirl flow case with the corresponding case calculated with no swirl. The burnout rate is clearly improved with swirling and the steep rise in burnout rate occurs at a distance closer to the injection point as compared to the one for the non-reacting case.

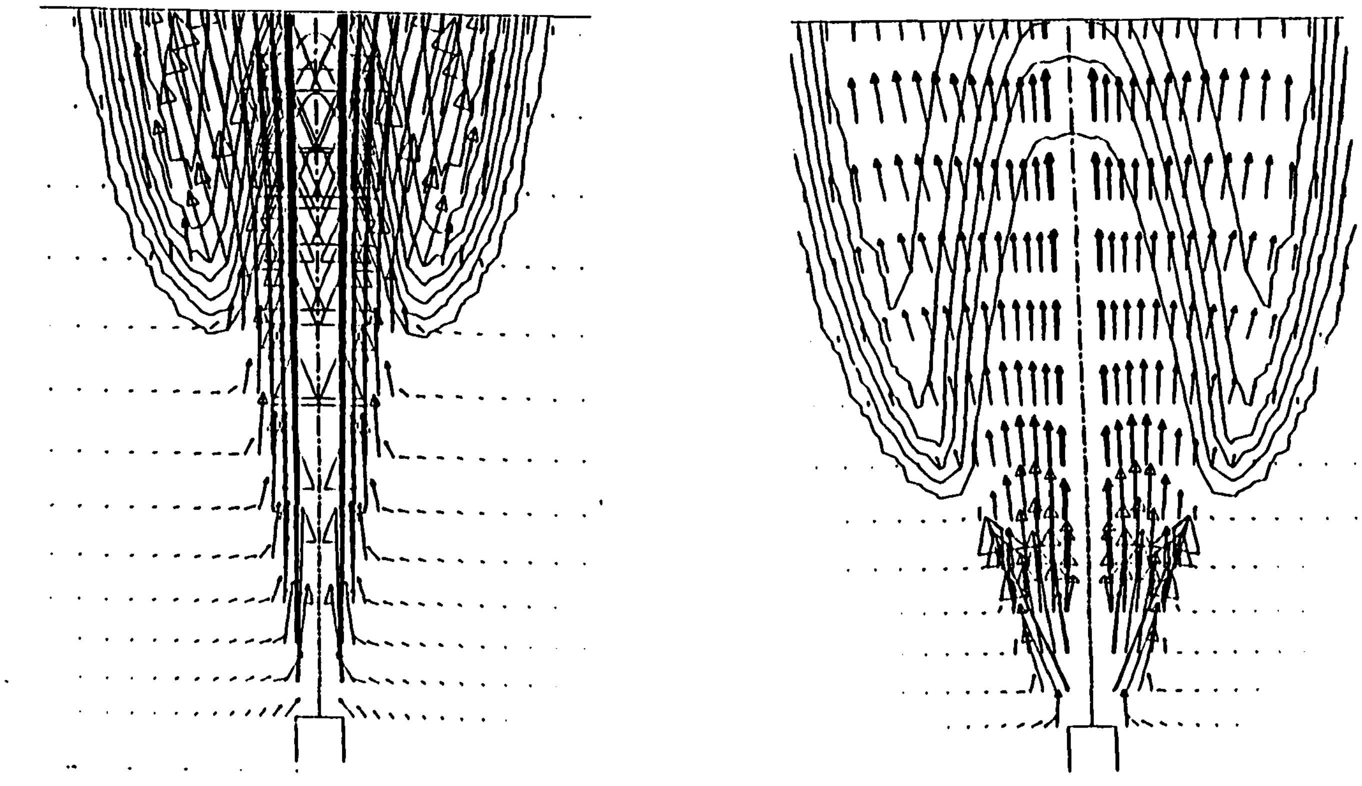

(a)

(b)

Fig. 5.33 Expanded view of velocity vectors and temperatue field at the flame base, (a) no swirl and (b) swirl.

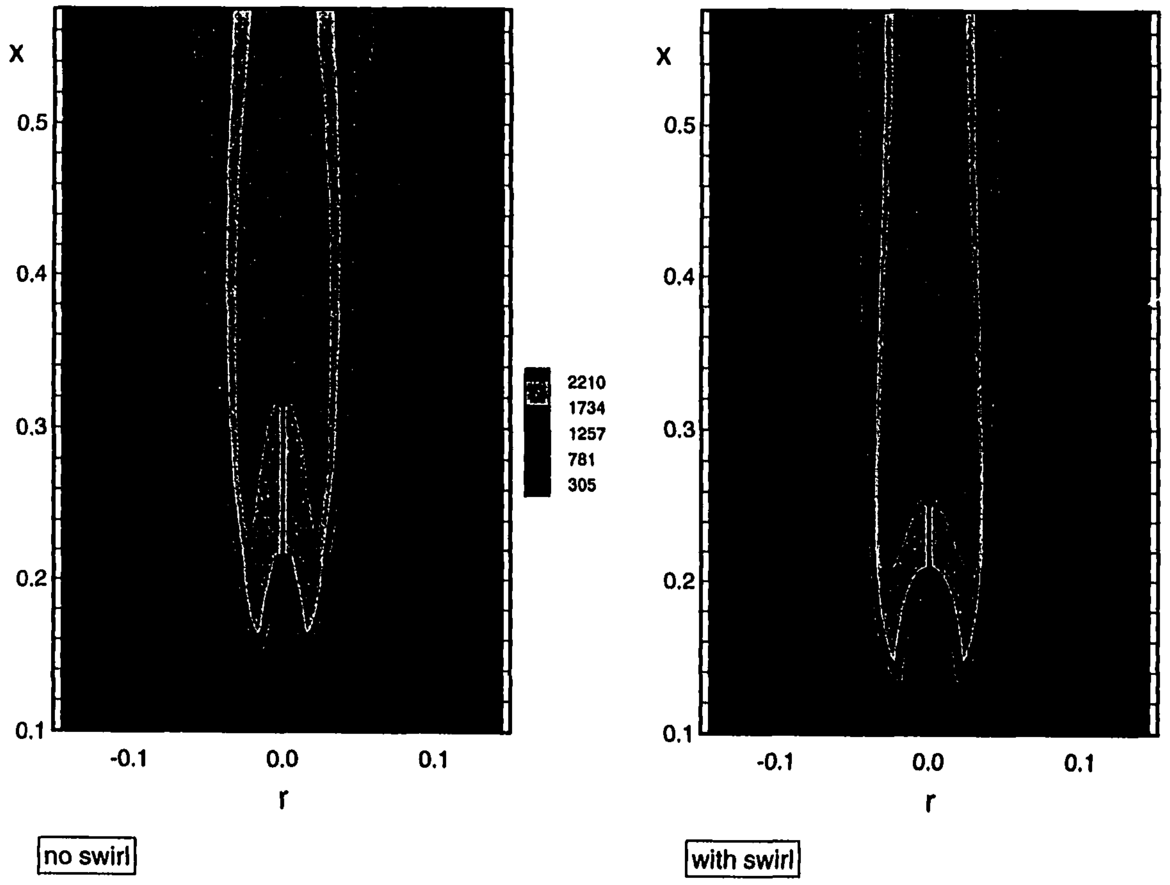

Fig. 5.34 Effect of swirling flows on the prediction of flame structuctre for methane fuel jet exit velocity of 34.7 m/s.

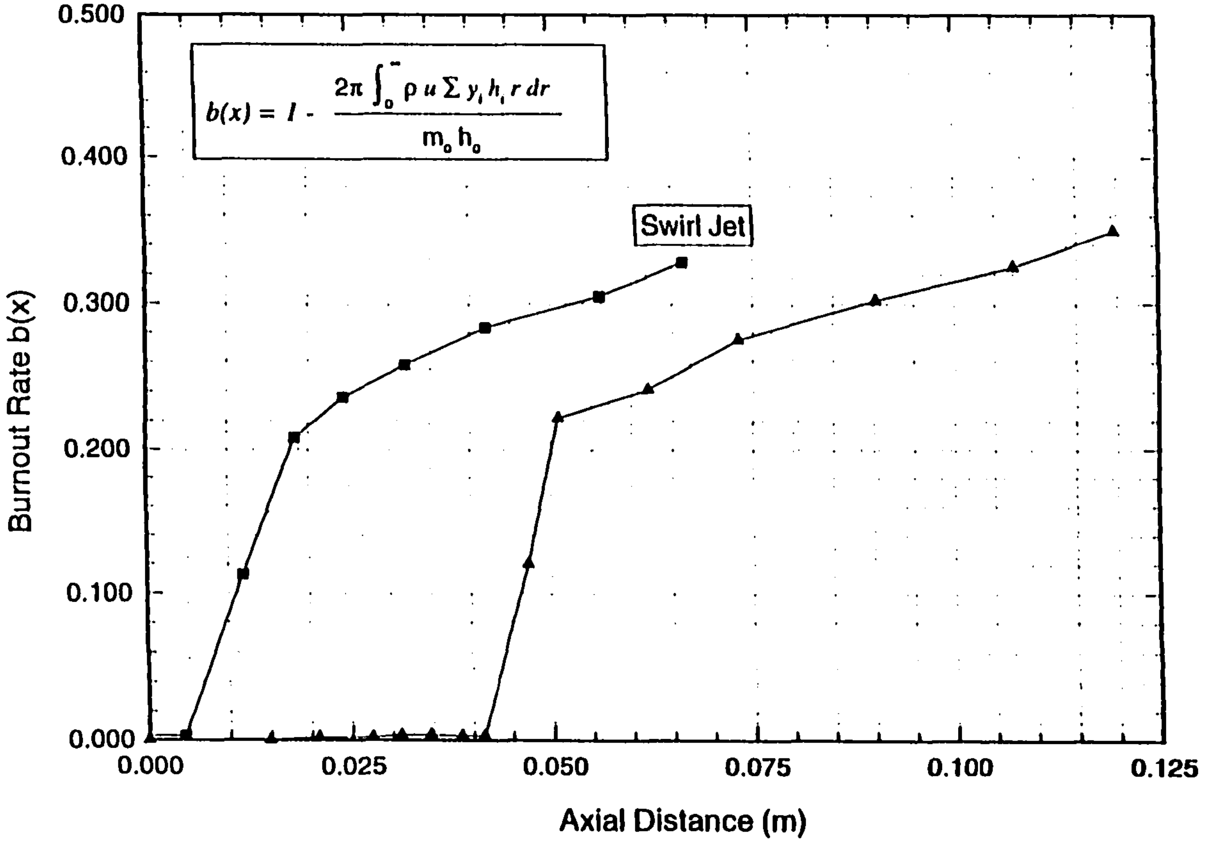

Fig. 5.35 Prediction of burnout rate along axial direction for jet exit velocity of 34.7 m/s, results with swirl jet are compared to results without swirling.

Chapter 6

CONCLUSIONS

The Reynolds stress model was used in conjunction with a two-step chemical kinetics model and the eddy dissipation model to predict the flame base height of a diffusion flame formed by a turbulent methane jet issuing vertical in a quiescent atmosphere. The RSM predicts flame base heights that are in reasonable agreement with the experimentally observed flame base height results. The model also successfully predicts the linear relationship between the flames base height and the fuel jet velocity. The flame base widens and flattens as the fuel jet velocity is increased. At the highest jet velocity, the flame base shows a double dip pattern in which the flame front also advances to an upstream location. It is to be noted that the RSM has yielded reasonable results with universally accepted constants in turbulence and the chemistry models.

Numerical results also reveal that the flame base, as postulated in a model by Vanquickenbourn and van Tigglen, is anchored in the premixed flammable region on the stoichiometric line where u-component of flow velocity is in equilibrium with the local turbulent flame speed. The numerical calculations for all fuels and velocity cases yielded radial distributions of turbulent velocity and the u-velocity that showed the tangency condition at the base of the diffusion flame as postulated by the hypothesis of Vanquickenborne and van Tigglen. Many other features of diffusion flames, as observed by others, have also been successfully calculated by the present model. These include the predicted bump in the axial velocity, the thermal expansion zone near the flame base and other flame characteristics such as the maximum width of the flame, and the flame height. The numerical results also indicate that the position of the flame base is strongly governed by the turbulent mixing in the fuel jet upstream of the flame base. In fact, the analysis of isothermal fuel jet case results in prediction of the flame base height that very closely replicate predictions in the reacting case.

The study also revealed that diffusion flames when analyzed with the eddy dissipation model in conjunction with the k-ϵ model yield results that are not in accord with experimental results. The results further suggest that the RSM yields more accurate results for flow and turbulence properties which in turn determine the location correctly where the local u-velocity is in equilibrium with the local turbulent flame velocity. In contrast, the k-ϵ model yields flow and turbulence properties that shift the point of equilibrium between the flow velocity and the flame velocity much closer to the point of fuel injection than observed in experiments. The large streamline curvature due to strong entrainment of ambient air near the flame base may be one of the reason for this discrepancy. The RSM, despite its modeling complexities, is the model of choice for use with the eddy dissipation model. We also conclude that it is possible to analyze gaseous diffusion flames formed with a variety of fuels by employing universally accepted constants in the RSM/eddy dissipation model.

The calculation of burnout rate also affords some insight into the physical mechanisms governing the diffusion flame phenomenon. It is noted that the numerically calculated burnout rate shows behavior similar to that observed experimentally by

Eickhoff et al. The burnout rate is nearly zero before the flame stabilization region, and then rises sharply to 0.3 to 0.5 values, depending on the fuel and jet velocity. This suggests that a significant amount of premixing has occurred prior to the flame base region. This observation supports studies that are based on the premixing concept.

The application of the RSM/eddy dissipation model to swirling yields results that indicate that the flame stabilization region for methane jet moves upstream as the swirling motion is increased. The location of flame stabilization region is once again governed by the tangency criteria.

For the propane jet, the RSM/eddy dissipation model predicts results that are in good agreement with experimental results. For example, the flame base height, calculated from the tangency criteria, is in good agreement (within ±10%) with experimental results. The numerical results also show that the flame base height versus fuel jet velocity curve, unlike that for methane, has a weak diameter dependence. The results for methane and hydrogen mixtures show very clearly defined flat flame base for most cases. The flame base, as calculated from the tangency criteria, moves upstream as the hydrogen concentration in the mixture increased.

The results from PDF/flame sheet model for methane have been compared with the results from the eddy dissipation model. One of the empirical constants in the PDF model had to be modified in order to achieve flame heights that are in accord with observed results. In order to achieve this, the constant $C_{g,2}$ was changed from 2 to 8.2. The results from this model also showed region of combustion surrounded by regions where flame is quenched. This scenario of flame surrounded by holes has been postulated by Peters and Williams, and Sanders et al.

REFERENCES

1. Patankar, S., V., Numerical Heat Transfer and Fluid Flow, Hemisphere Publishing Corp., Washington, DC, 1980.

2. Pitts, W., "Assessment of Theories for the Behavior and Blowout of Lifted Turbulent Jet Diffusion Flames," Twenty-Second Symposium (International) on Combustion, The Combustion Institute, Aug. 1988, pp. 809-816.

3. Vanquickenborne, L. and van Tiggelen, A., "The Stabilization Mechanism of Lifted Diffusion Flames," Combustion and Flame, Vol. 10, No. 1, 1966, pp. 59-69.

4. Günther, R., Horch, K. and Lenze, B., "The Stabilization Mechanism of Free Jet Diffusion Flame," First Specialist meeting (International) of the Combustion Institute, The Combustion Institute, Pittsburgh, Aug. 1981, pp. 117-122.

5. Annushkin, Y. and Sverdlov, E., "Stability of submerged Diffusion Flames in Subsonic and Underexpanded Supersonic Gas-Fuel Streams," Combustion Explosion and Shock Waves, Vol. 14, 1979, pp. 597-605.

6. Hall, L., Horch, K. and Günther, R., "Die Stabilator Von Fveistahl - Diffusions Flammer," Brenst-Warme-Kraft, Vol. 32, No. 1, 1980, pp. 26-31.

7. Kalaghatgi, G., "Lift-Off Heights and Visible Length of Vertical Turbulent Jet Diffusion Flames in Still Air," Combustion Science and Technology, Vol. 41, No. 1, 1984, pp. 17-29.

8. Comer, K., Mohieldin, T., Tiwari, S., and Puster, R., " Experimental and Numerical Investigation of Lifted Methane Diffusion Flames," AIAA Paper, 95-0728, Jan. 1995.

9. Peters, N., "Laminar Flamelet Concepts in Turbulent Combustion," Twenty-First Symposium (International) on Combustion, The Combustion Institute, Aug. 1986, pp. 1231-1250.

10. Janika, J. and Peters, N., "Prediction of Turbulent Jet Diffusion Flame Lift-Off Using a PDF Transport Equation," Nineteenth Symposium (International) on Combustion, The Combustion Institute, Aug. 1982, pp. 367-374.

11. Peters, N. and Williams, F., "Lift-Off Characteristics of Turbulent Let Diffusion Flame," AIAA Journal, Vol. 24, No. 3, 1983, pp. 423-429.

12. Sanders, J. and Lamers, A., "Modeling and Calculation of Turbulent Lifted Diffusion Flames," Combustion and Flames, Vol. 96, No. 1, 1994, pp. 22-33.

13. Bradley, P., Gaskell, H. and Lau, A., " A Mixedness-Reactedness Flamelet Model for Turbulent Diffusion Flames," Twenty-Third Symposium (International) on Combustion, The Combustion Institute, July 1990, pp. 685-692.

14. Tsuji, H. and Yamaoka, I., "A Gas Dynamic Analysis of the Counterflow Diffusion Flame in the Forward Stagnation Region of a Porous Cylinder," Institution of Space and Aronautics, University of Tokyo Report No. 404, 1966.

15. Tsuji, H., "Counterflow Diffusion Flames," Progress in Energy and Combustion science, Vol. 8, No. 1, 1982, pp. 93-108.

16. Tsuji, H. and Yamaoka, I., "The Counterflow Diffusion Flame in Forward Stagnation Region of a Porous Cylinder," Eleventh Symposium (International) on Combustion, The Combustion Institute, Sept. 1967, pp. 979-991.

17. Puri, I. and Seshadri, K., "Extinction of Diffusion Flame Burning Diluted Methane and Diluted Propane in Diluted Air," Combustion and Flame, Vol. 65, No. 2, 1986, pp. 137-150.

18. Mitchell, R., Sarofim, A. and Clomburg, L., " Experimental and Numerical Investigation of Confined Laminar Diffusion Flames," Combustion and Flame, Vol. 37, No. 2, 1980, pp. 227-239.

19. Dixon-Lewis, G., David, T., Haskell, P., Fukutani, S., Jinno, H., Miller, J., Kee, R., Smooke, M., Peters, N., Effelsberg, E., Warnatz, J., and Behrendt, F., "Calculation of the structure and Extinction Limit of a Methane-Air Counterflow Diffusion Flame in the Forward Stagnation Region of a Porous Cylinder," Twentieth Symposium (International) on Combustion, The Combustion Institute, Aug. 1984, pp. 1893-1904.

20. Keyes, D. and Smooke, M., "Flame Sheet Starting Estimates for Counterflow Diffusion Flame Problems," Journal of Computational Physics, Vol. 73, No. 2, 1987, pp. 267-288.

21. Smooke, M., "Solution of Burner Stabilized Premixed Laminar Flames by Boundary Value Methods," Journal of Computational physics, Vol. 48, No.1, 1982, pp. 72-89.

22. Yuenong, X. and Smooke, M., "Primitive Modelling of Multidimensional Laminar Flames," Combustion Science and Technology, Vol. 90, No. 2, 1993, pp. 289-313.

23. Smooke, M., Mitchell, R., and Keyes, D., "Numerical Solution of Two-Dimensional Axisymmetric Laminar Diffusion Flames," Combustion Science and Technology, Vol. 67, No.1, 1989, pp. 85-122.

24. Smooke, M., "On the Use of Adaptive Grids in Premixed Combustion," American Institute of Chemical Engineering, Vol. 32, 1986, pp. 1233-1241.

25. Kee, R., Miller, J. and Jefferson, T., "CHEMKIN: A General-Purpose, Transportable, Fortran Chemical Kinetics Code Package," Sandia National Labs., Livermore, CA, Report SAND80-8003, March 1980.

26. Kee, R., Warnatz, J. and Miller, J., "A Fortran Computer Code Package for the Evaluation of Gas-Phase Viscosities, Conductivities, and Diffusion Coefficients," Sandia National Labs., Livermore, CA, Report SAND80-8003, March 1983.

27. Kee, R., Rupley, F.. and Miller, J., "The Chemkin Thermodynamics Data Base," Sandia National Labs., Livermore, CA, Report SAND80-8003, March 1983.

28. Miller, J., Mitchell, R., Smooke, M. and Kee, R., "Toward a Comprehensive Chemical Kinetic Mechanism for the Oxidation of Acetylene: Comparison of Model Predictions with Results from Flame and Shock Tube Experiments," Nineteenth Symposium (International) on Combustion, The Combustion Institute, Aug. 1982, pp. 181-197

29. Miller, J., Green, R. and Kee, R., " Kinetics Modeling of the Oxidation of Ammonia in Flames," Combustion Science and Technology, Vol. 34, No.2, 1983, pp. 149-162.

30. Miller, J. and Kee, R., "Chemical None-equilibrium Effects in Hydrogen-Air Laminar Flames," Journal of physical Chemistry, Vol. 81, 1977, pp. 2534-2562.

31. Rokke, N., Hustad, J. and Sonju, O., "A Study of Partially Premixed Unconfined Propane Flames," Combustion and Flames, Vol. 97, No. 1, 1994, pp. 88-106.

32. Sonju, O. and Hustad, J., "An Experimental Study of Turbulent Jet Diffusion Flames," Proceedings from the First International Conference on Combustion Technologies for a Clean Environment, Gilmoura, Portugal, 1991, pp. 320-339.

33. Magnussen, G., and Hjertager, B., "On Mathematical Models of Turbulent Combustion with Special Emphasis on Soot Formation and Combustion," Sixteenth

Symposium (International) on Combustion, The Combustion Institute, July 1976, pp. 15-26.

34. Lau., J., "Comparison of pdf and Eddy-Dissipation Combustion Model Applied to Propane Jet Flame," Combustion and Flame, Vol. 102, No. 1, 1995, pp. 209-215.

35. Mohieldin, T. and Chaturvedi, S., "Flame Lift-off and Thermal Load Characteristics of a Cylindrical Injector," Numerical Methods in Thermal Problems, Vol. 8, No. 1, 1995, pp. 209-215.

36. Broadwell, J., Dahm, W., and Mungal, M., "Blowout of Turbulent Diffusion Flames," Twentieth Symposium (International) on Combustion, The Combustion Institute, Aug. 1984, pp. 303-310.

37. Rodi, W., "Examples of Turbulence-Model Applications," Turbulence Models and their Applications, Vol. 2, 1984.

38. Bradshaw, P. Ferriss, D., and Atwell, N., "Calculation of Boundary-Layer Development using Turbulent Energy Equation," Journal of Mechanics, Vol. 28, No.2, 1967, pp. 593.

39. Jones, W. and Launder, B., "The Prediction of Laminarization with a 2-Equation Model of Turbulence," International Journal of Heat and Mass Transfer, Vol. 15, No. 2, 1972, pp. 301-324.

40. Spalding, D., "The Prediction of Two-Dimensional Steady Turbulent Flows," Imperial College, Heat Transfer Section Report EF/TN/A/16, 1969

41. Mellor, G., Herring, H., "A Survey of the Mean Turbulent Field Closure Models," AIAA Journal, Vol. 11, 1973, pp. 560-612.

42. Schetz, J., Injection and Mixing in Turbulent Flow, Progress in Astronautics and Aeronautics, New York, 1980.

43. Ayoub, G., "Dispersion of Buoyant Jets in a Flowing Ambient Fluid," Ph.D. thesis, University of London, May 1971.

44. Launder, B. and Spalding, D., "The Numerical Computation of Turbulent Flows," Imperial College of Science and Technology, NTIS N74-12966.

45. Jones, W. and McGuirk, J., "Computation of a Round Jet Discharging into Confined Cross Flow," Turbulent Shear Flow 2, Springer Verlag, Heidelberg, 1980.

46. Patankar, S., Pratap, V., and Spalding, D., "Prediction of Turbulent Flow in Curved Pipes," Journal of Fluid Mechanics, Vol. 67, 1975, pp. 583-595.

47. Rodi, W. and Srivatsa, S., "A Locally Elliptic Calculation Procedure for three-Dimensional Flows and its Application to jet in a Cross Flow," Computational Methods in Applied Mechanics and Engineering, Vol. 23, No.1, 1980, pp. 67-83.

48. Ratogi, A. and Rodi, W., "Predictions of Heat and Mass Transfer in Open Channels," Journal of Hydraulics Div., No. 3, 1978, pp.397-420.

49. McGuirk, J. and Rodi, W., "Mathematical Modelling of Three-Dimensional Heated Surface Jets," Journal of Fluid Mechanics, Vol. 95, 1979, pp.609-634.

50. Scharma, D., "Turbulent Convection Phenomena in Straight, Rectangular Sectioned Diffusers," Ph.D. thesis, University of London, 1974.

51. Pope, S., "An Explanation of the Turbulent Round-Jet/Plane-Jet Anomaly," AIAA Journal, Vol. 16, 1978, pp. 279-281.

52. Janicka, J. "A Reynolds-Stress Model for the Prediction of Diffusion Flames," Twenty-First Symposium (International) on Combustion, The Combustion Institute, Aug. 1988, pp. 1409-1417.

53. Weber, R., Boysan, F., Swithenbank, J. and Roberts, P., "Computations of Near Field Aerodynamics of Swirling Expanding Flows," Twenty-First Symposium (International) on Combustion, The Combustion Institute, Aug. 1988, pp. 1436-1443

54. Bittker, D. and Scullin, V., "General Chemical Kinetics Computer Program for Static or Flow Reactors, With Application to Combustion and Shock-Tube Kinetics," NASA TN D-6586, Jan. 1972.

55. Dickinson, R. and Gelinas, R., "SETKIN: A Chemical Kinetics Preprocessor Code," Numerical Methods for Differential Systems, Academic Press, Inc., New York, 1976.

56. Gordon, S. and Mcbride, J., "Computer Program for Calculation of Complex Chemical equilibrium Compositions, Rocket Performance, Incident and Reflected Shocks and Chapman-Jauguet Detonations," NASA SP-273, 1971.

57. Coffee, T. and Heimerl, J., Combustion and Flame, Vol. 43, 1981, pp. 273-289.

58. Westbrook, C. and Dryer, F., "Chemical Kinetic Modeling Hydrocarbon Combustion," Progress in Energy and Combustion Science, Vol. 10, Jan. 1984, pp. 1-57.

59. Coffee, T., Kotlar, A. and Miller, M., "The Overall Reaction Concept in Premixed, Laminar, Steady-State Flame. I. Stoichiometries," Combustion and Flame, Vol. 54, 1983, pp. 155-169.

60. Peters, N. and Williams, F., "The Asymptotic Structure of Stoichiometric Methane-Air Flames," Combustion and Flame, Vol. 68, No. 1, 1987, pp. 185-207.

61. Peters, N. and Kee, R., "The Computation of Stretched Laminar Methane-Air Diffusion Flames Using a Reduced Four Step Mechanism," Combustion and Flame, Vol. 68, No. 1, 1987, pp. 17-29.

62. Dryer, F. and Glassman, I., "High-Temperature Oxidation of CO and CH4," Fourteenth Symposium (International) on Combustion, The Combustion Institute, Sept. 1973, pp. 987-1003.

63. Hautmann, D., Dryer, F., Schug, K. and Glassman, I., "A Multiple -Step Overall Kinetic Mechanism for Oxidation of Hydrocarbons," Combustion Science and Technology, Vol. 25, 1981, pp. 219-235.

64. Nikjooy, M. and So, R., "On the Modeling of Non-Reactive and Reactive Turbulent Combuster Flows," NASA Report 4041, April, 1987.

65. Moss, J., "Turbulent Diffusion Flames," Combustion Fundamentals of Fire, Chap. 4, Academic Press, 1995, pp. 221-272.

66. Mohieldin, T., "Numerical Modeling of Flame Lift-Off Phenomenon and Calculation of Thermal Loads on a methane Fuel Injector with Complex Geometry," Ph.D. thesis, Old Dominion University, 1991.

67. Spalding, D., "Mixing and Chemical Reaction in Steady Confined Turbulent Flame," Thirteenth Symposium (International) on Combustion, The Combustion Institute, Aug. 1972, pp. 649-657.

68. Kanury, A., Introduction to Combustion Phenomena, Gordon and Breach, New York, 1992.

69. Jones, W., "Turbulence Modelling and Numerical Solution Methods for Variable Density and Combustion Flows," Turbulent Reacting Flows, Academic Press, Washington DC, 1994, pp. 309-374.

70. Soong, H., Han, H. and Chang, K., "Comparative numerical Studies on Reynolds and Favre Averagings of Turbulent Diffusion Flame," Journal of Propulsion and Power, Vol. 8, No. 1, 1992, pp. 259-263

71. Launder, B., "Current Capabilities for Modeling Turbulence in Industrial Flows", Journal of Applied Scientific Research, Vol. 48, Jan. 1991, pp. 247-269.

72. Launder, B., Reece, G. and Rodi. W., "Progress in the Development of a Reynolds Stress Turbulence Closure," Journal of Fluid Mechanics, Vol. 68, 1975, pp. 537-566.

73. Varma, A., Chatwani, A., and Bracco, F., "The Overall Reaction Concept in Premixed Laminar Steady State Flame," Combustion and Flame, Vol. 64, No. 1, 1986, pp. 223-226.

74. Hirsch, C., Numerical Computation of internal and External Flows, Vol 2, Wiley, New York, 1990.

75. Anderson, D., Tannehill, J. and Pletcher, R., Computational Fluid Mechanics and Heat Transfer, Hemisphere, New York, 1984.

76. Leonard, B., "A Stable and Accurate Convective Modelling Procedure Based on Quadratic Upstream Interpolation," Computer Method in Applied Mech. Eng., Vol. 19, Jan. 1979, pp. 59-98.

77. Leonard, B., "Third-Order Multidimensional Monotonic Euler/Navier Stokes Solver," Proceedings of the First National Fluid Dynamics Conference, Cincinnati, Ohio, July 1988.

78. Majumdar, S., "Role of Underrelaxation in Momentum Interpolation for Calculation of Flow with Nonstaggered Grids," Numerical Heat Transfer, Vol. 13, 1988, pp. 125-132.

79. Rhie, C. and Chow, W., "Numerical Study of the Turbulent Flow Past an Airfoil with Tailing Edge Separation," AIAA Journal, Vol. 21, No. 11, 1983, pp. 1525-1532.

80. Fluent Code V. 4.2, Fluent Inc., Lebanon, New Hampshire, 1992.

81. Eickhoff, H., Lenze, B., and Leuckel, W., "Experimental Investigation on the stabilization Mechanism of Jet Diffusion Flames," Twentieth Symposium (International) on Combustion, The Combustion Institute, Aug. 1984, pp. 311-318.

82. Bray, K. and Peters, N., "Laminar Flamelet in Turbulent Flames," Turbulent Reacting Flows, Academic Press, Washington DC, 1994, pp. 63-113.

83. Wygnanski, I. and Fiedler, H., "Some Measurements in the self-Preserving Jet," Journal of Fluid Mechanics, Vol. 38, No. 3, 1969, pp. 577-612.

84. Donaldson, C., "A progress Report on an Attempt to construct an Invariant Model of Turbulent Shear Flows," Turbulent Shear Flows, AGARD CP-93, 1971.

85. Horch, K., Ph. D. thesis, Universitat Karlsruhe, Geramy, 1978.

86. Pitts, W., "Importance of Isothermal Mixing Processes to Understanding of Lift-off and Blowout of Turbulent Jet Flames," Combustion and Flame, Vol. 76, No. 1, 1989, pp. 197-212.

87. Chen, J. and Kollmann, W., "PDF Modeling of Chemical Nonequilbrium Effects in Turbulent Nonpremixed Hydrocarbon Flames", Twenty-Second Symposium (International) on Combustion, The Combustion Institute, Aug.1988, pp. 645-653.

88. Spalding, D., "A Mixing Rule for Laminar Flame Speed," Fuel London, Vol. 35, Feb. 1956, pp. 347-351.

89. Martin, D., "Flame Speeds of Mixture Containing Several Combustible Components or a Known Quantity of Diluent," Fuel London, Vol. 35, Feb. 1956, pp. 352-358.

90. Brizuela, E. and Bigler, R., "On the Eddy Break-Up Coefficient," Combustion of Flame, Vol. 104, No. 1, 1996, pp. 208-212.

91. Bai, X. and Fuchs, L., "Sensitivity Study of Turbulent Reacting Flow Modeling in Gas Turbine Combustors," AIAA Journal, Vol. 33, No. 11, 1995, pp. 1857-1870.